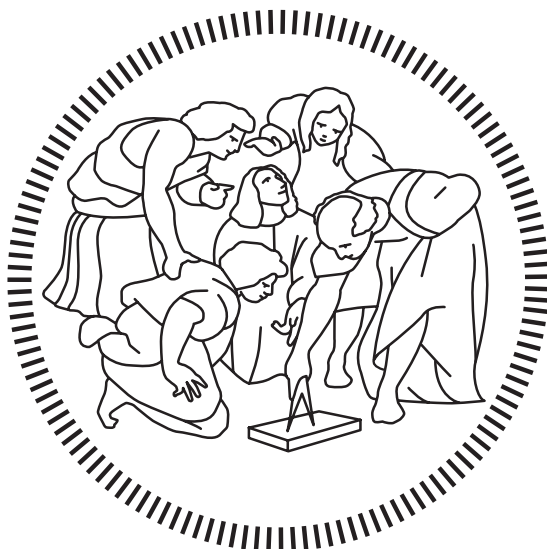


**Politecnico di Milano**

---

SCHOOL OF INDUSTRIAL AND INFORMATION ENGINEERING

Master of Science – Nuclear Engineering



# Femtosecond Laser Micromachining of Integrated Optofluidic Devices for Extreme UV Generation in Gases

Supervisor

**Prof. Roberto OSELLAME**

Co-Supervisor

**Dr. Rebeca MARTINEZ VAZQUEZ**

Candidate

**Pasquale BARBATO**

**913326**

---

Academic Year 2019 – 2020



# Ringraziamenti

Nel caso in cui qualcuno si trovasse a leggere questo testo, è giusto sia informato del fatto che ciò è possibile solo grazie a Roberto Osellame che, accogliendomi nel suo gruppo, mi ha dato la possibilità di lavorare a una tesi tanto affascinante quanto gratificante, e a Rebeca Martinez Vazquez, che mi ha insegnato quasi tutto quello che troverete in questo lavoro. Andando ben oltre il suo ruolo di correlatrice, Rebeca mi ha mostrato come si sta in un laboratorio e cosa vuol dire fare ricerca, facendomi appassionare ancora di più a quello che ho sempre sperato potesse diventare un giorno il mio mestiere. A lei va quindi il mio più sincero ringraziamento.

Ringrazio anche tutto il gruppo di Francesca Calegari al Deutsches Elektronen-Synchrotron, con il quale ho collaborato per lo sviluppo di una parte importante di questo lavoro. Grazie alla professionalità di tutti loro ho potuto portare a termine il mio percorso di studi nonostante la tristemente nota pandemia, che per tanti ha significato incertezza e sofferenza. Non posso quindi non dedicare anche un pensiero a quanti, al Politecnico ma non solo, si sono adoperati affinché la vita risentisse al minimo degli effetti del COVID-19.

Nei ringraziamenti per la tesi si è soliti rivolgersi non solo a chi nel concreto ha contribuito alla sua realizzazione, ma anche a tutti coloro che sono stati in qualche modo importanti nei cinque anni di studi di cui questo lavoro è il culmine. È per questo che dico grazie alla mia famiglia, Sandro, Lorella e Alessandra, che mi ha permesso di intraprendere questo percorso, ma anche a Silvana, Massimiliano, Giuseppe, Cristina, Angela e Michela, il cui supporto è stato prezioso soprattutto nei primi anni a Milano. Tra i tanti professori che ho incontrato in questo percorso, alcuni si sono rivelati fondamentali nel contribuire alla mia formazione non solo accademica, ma anche personale. A loro tutti la mia più profonda stima e gratitudine.

Ringraziare uno ad uno tutte le persone che mi hanno fatto dono della loro amicizia in questi anni richiederebbe un capitolo a parte. Ricorderò sempre con affetto tanti tra quelli che ho incontrato in Camplus e al Politecnico, sia che mi siano stati vicino per pochi giorni o per molti anni. Mi rivolgo in modo particolare ai miei coinquilini Claudio e Emanuele, e Jacopo, compagno di studi da più di dieci anni. Grazie anche agli altri amici di vecchia data, come Edoardo e Matteo, che mi sono sempre rimasti vicini nonostante la lontananza.

Mi rivolgo infine ad Antonella: sai bene quanto sei stata importante nella mia vita, e mi sembra superfluo stare qui a ricordarlo. Voglio però che si sappia che senza di te questa tesi non sarebbe stata la stessa o, più probabilmente, non ci sarebbe affatto stata.



# Sommario

Questo lavoro di tesi è dedicato allo sviluppo di dispositivi optofluidici integrati per la generazione di impulsi ad attosecondi nell'estremo ultravioletto.

Tali dispositivi sono stati realizzati all'interno di un substrato di vetro con una tecnica nota come FLICE (Femtosecond Laser mIcromachining followed by Chemical Etching). Il fascio di un laser a femtosecondi viene focalizzato all'interno del materiale, che viene modificato localmente. La zona danneggiata diventa particolarmente sensibile ad un attacco chimico, e questo permette di fabbricare con precisione micrometrica delle strutture cave, tridimensionali ed articolate quanto si voglia, in un supporto delle dimensioni di qualche millimetro. Dispositivi così realizzati trovano diversi campi di applicazione. In questo caso, sono stati progettati per ospitare l'interazione tra un fascio laser a femtosecondi ad alta energia e le molecole di un gas nobile, fenomeno che risulta nell'emissione di radiazione nell'estremo ultravioletto.

In particolare, è stato realizzato un dispositivo che integra un sistema di pompaggio differenziale, appositamente studiato per garantire il miglior confinamento del gas e sostituire un apparato esterno usato in un precedente lavoro [1]. Nell'ambito dell'attività aggiuntiva per la tesi richiesta dal percorso ASPRI, è stato simulato il flusso del gas al suo interno.

Parallelamente, si sono studiati gli effetti di un trattamento termico subito da una guida cava utilizzata per la generazione di armoniche di ordine elevato (HHG), ed è stato rilevato un aumento della resa di generazione. Si è caratterizzato questo dispositivo prima e dopo il trattamento nel tentativo di comprendere la variazione delle proprietà ottiche a seguito di un cambiamento strutturale.

Questo lavoro rappresenta un piccolo passo in avanti verso l'integrazione di un numero sempre maggiore di funzionalità all'interno di dispositivi fotonici e nella comprensione del loro funzionamento, che in futuro rappresenteranno un prezioso strumento per la generazione di impulsi ultra-brevi nell'estremo ultravioletto, fino ai raggi X.



# Abstract

This thesis work is devoted to the realization of integrated optofluidic devices for the generation of extreme ultraviolet radiation.

These devices are fabricated on a glass substrate with a technique known as FLICE (Femtosecond Laser micromachining followed by Chemical Etching). A femtosecond tightly focused laser beam is able to modify locally the material, which in that zone becomes more sensitive to chemical attack. It is then possible to build with micrometric precision articulated, three-dimensional hollow structures, which can be employed in various applications. Here, they are designed to host the interaction between a strong femtosecond laser beam and noble gas molecules, a process which results in the emission of extreme ultraviolet radiation.

In particular, a device which integrates a differential pumping system was realized, specifically developed to guarantee a good gas confinement aiming to replace the bulky apparatus used in a previous work [1]. In the framework of the additional thesis activity required by ASPRI project, it was simulated the gas flow inside this device. Meanwhile, the effects of a thermal treatment on a hollow waveguide used for High-order Harmonic Generation (HHG) were studied. It was revealed an increase in the generation yield. This chip was characterized before and after the annealing, in the attempt of understanding how structural changes influences optical properties.

This work represent a little step forward in the integration of multiple functionalities inside photonic devices and in the understanding of their working principles, because in future they will represent a precious instrument for the generation of ultrafast extreme ultraviolet and soft X-ray pulses.



# Extended Abstract

Research on integrated microfluidic devices is today drawing the attention of many scientists, appearing as a promising tool for a new generation of extreme ultraviolet (EUV) and soft X-ray (SXR) attosecond pulses sources. In particular, hollow structure realized with FLICE technique already proved successful in hosting third harmonic generation [1] and high-order harmonic generation [2], setting new records in the production of high-quality pulses in the EUV region of the spectrum.

The interest in such sources is motivated by the will of exploring ultrafast phenomena occurring in atoms, molecules and condensed matter, which dynamics could be captured in their fundamental times ( $\sim fs$ ) and lengths ( $\sim nm$ ) by attosecond pulses. To achieve this goal, much work is still needed both on the theoretical comprehension of highly nonlinear optical phenomena which can be triggered in hollow structures and on the integration in these devices of more functionalities so that a few centimeter chip has the same capabilities of much larger equipment.

In this thesis, I present the design and the development of a microfluidic device which integrates a differential pumping system, that is a series of chambers and channels specifically thought to ensure a high gas density in the part of the chip devoted to deep UV generation via third harmonic up-conversion of a near-infrared driving laser. This project was done in collaboration with the Attosecond Science division at Deutsches Elektronen-Synchrotron (DESY), in Hamburg, where is located the experimental setup which contains the external differential pumping system this new chip aims to replace. Unfortunately, it was not possible to test this device yet, due to a series of delays mainly related to COVID-19 pandemic, that forced for long time people at home, especially in Germany, where a severe lockdown has been imposed for the most of the duration of this thesis. At the time of writing, the device is ready and we are waiting for the realization of a home-build mounting to house the chip, which we plan to test in the next months.

In the framework of the additional activity to the master thesis foreseen by the ASPRI program, I performed some preliminary simulations of the behaviour of the gas inside the new differential pumping chip. The study of the gas-flow inside optofluidic micro-devices is something still mostly unexplored, but, in my opinion, will become increasingly more important. In fact, integrating more functionalities will mean fabricating more complicated structures, and to have a clear understanding of the glass flow inside them will be crucial both to study the feasibility of new concepts and to optimize the already existing ones. For this reason, I exploited the Free Molecular Flow module of COMSOL multiphysics, which was deepened to highlight advantages

and limitations in its use.

In the same time, I fabricated, optically characterized and assisted to HHG characterization of a chip which for the first time underwent a thermal treatment to enhance its structural properties, especially the smoothness of the internal surface. It was found that the annealing process effectively improves the performances of the device, encouraging further studies in the theoretical investigation of the interaction between the propagating light and the wall of the device, and in the optimization of thermal treatments.

In this thesis are then reported the main passages of this activity, starting with a theoretical review of the very interesting physics involved. The material is organized as follows:

- In **Chapter 1** is presented the micromachining technique used for the fabrication of all the prototypes of this work, with a focus on the underlying physics but with a description also of the more practical aspects.
- In **Chapter 2** is explained the importance of deep UV radiation for pump-probe spectroscopy; then it is introduced the third harmonic generation and the experimental setup used in [1] for the generation of sub-2-fs pulses, with a special attention to the bulky differential pumping system.
- **Chapter 3** is fully devoted to high-order harmonic generation, to the models used to explain this phenomenon and the expedients used to enhance it, especially the utilisation of hollow waveguide.
- In **Chapter 4** are detailed all the experimental apparatus used in this work.
- **Chapter 5** contains the motivations behind the realization of the differential pumping chip, its design, and the solutions adopted for its fabrication, which was quite difficult due to its dimensions.
- In **Chapter 6** is reported the optical characterization of the annealed HHG chip and the spectra of the generated harmonics.
- In **Appendix A** are shown the gas flow simulations performed on the differential pumping chip, together with a brief excursus on the free molecular flow regime and its numerical implementation.

# Contents

<b>Ringraziamenti</b>	<b>iii</b>
<b>Sommario</b>	<b>v</b>
<b>Abstract</b>	<b>vii</b>
<b>Extended Abstract</b>	<b>ix</b>
<b>Contents</b>	<b>xii</b>
<b>List of Figures</b>	<b>xv</b>
<b>List of Tables</b>	<b>xvii</b>
<b>1 Femtosecond Laser Micromachining</b>	<b>1</b>
1.1 Introduction . . . . .	1
1.2 Femtosecond Laser Micromachining Physics . . . . .	2
1.2.1 Carrier Excitation and Free Electron Plasma Formation . . . . .	3
1.2.2 Bulk Modification . . . . .	5
1.2.3 Transient Nanoplasmonic Model . . . . .	7
1.2.4 Exposure parameters . . . . .	7
1.3 FLICE (Femtosecond Laser mIcromachining followed by Chemical Etching) . . . . .	10
1.3.1 Chemical Etching . . . . .	10
1.3.2 Channel Properties . . . . .	11
1.3.3 Surface Roughness and Glass Annealing . . . . .	12
<b>2 Few-Femtosecond Deep UV Generation</b>	<b>15</b>
2.1 Introduction . . . . .	15
2.2 Third Harmonic Generation in Gases . . . . .	17
2.2.1 Classical Formulation . . . . .	18
2.2.2 Quantum Formulation . . . . .	19
2.3 Experimental Setup for Generation of Deep Ultraviolet Sub-2-fs Pulses	20
2.3.1 Bulky Differential Pumping and Recirculation System . . . . .	22
<b>3 High-Order Harmonic Generation</b>	<b>25</b>
3.1 Introduction . . . . .	25
3.2 Three-Step Model . . . . .	26
3.2.1 Ionization . . . . .	27

3.2.2	Motion in the Electric Field . . . . .	29
3.2.3	Recombination . . . . .	30
3.3	Quantum Models . . . . .	32
3.3.1	Quantum Treatment of Electrons' Dynamics . . . . .	32
3.3.2	Quantum-Optical Formulation . . . . .	33
3.4	HHG Improvement Strategies . . . . .	34
3.4.1	Phase Matching . . . . .	34
3.4.2	Gas-Filled Hollow Waveguide . . . . .	36
<b>4</b>	<b>Materials and Methods</b>	<b>39</b>
4.1	FLICE Fabrication Setup . . . . .	39
4.2	Hollow Waveguide Characterization . . . . .	42
4.3	HHG Setup . . . . .	43
<b>5</b>	<b>Differential Pumping Chip</b>	<b>47</b>
5.1	Introduction . . . . .	47
5.2	Design Criteria . . . . .	48
5.2.1	Gas Flow Simulations . . . . .	51
5.3	Fabrication . . . . .	54
5.3.1	Etching Dynamic Analysis . . . . .	54
5.3.2	Cell Fabrication: Solutions and Parameters . . . . .	56
5.3.3	DPC micromachining . . . . .	58
<b>6</b>	<b>High-Order Harmonic Generation in a Thermally Treated Glass Chip</b>	<b>61</b>
6.1	Introduction . . . . .	61
6.2	Device Characterization . . . . .	63
6.3	HHG in an Annealed Gas-Filled Hollow Waveguide . . . . .	65
	<b>Conclusions</b>	<b>67</b>
<b>A</b>	<b>Free Molecular Flow Simulations with COMSOL Multiphysics</b>	<b>69</b>
A.1	Molecular Gas Flow in Micro-Devices . . . . .	69
A.1.1	Angular Coefficient Method . . . . .	71
A.2	Differential Pumping Chip Simulations . . . . .	73
A.2.1	Conclusions . . . . .	78
	<b>Acronyms</b>	<b>79</b>
	<b>Bibliography</b>	<b>81</b>

# List of Figures

Figure 1.1	Timescale of the most important phenomena occurring in the interaction of a femtosecond laser with a transparent material . . . . .	2
Figure 1.2	Schematics of nonlinear photoionization processes: multiphoton ionization, tunneling ionization and avalanche ionization . . . . .	3
Figure 1.3	Illustration of the femtosecond laser micromachining main steps	5
Figure 1.4	Visual representation of the nanograting formation aligned perpendicularly to the writing laser polarization . . . . .	6
Figure 1.5	Longitudinal and transverse writing geometries . . . . .	9
Figure 1.6	Scanning electron images of nanogratings formed with different writing directions . . . . .	10
Figure 1.7	Etching effectiveness for different writing geometries . . . . .	11
Figure 1.8	Schematic writing pattern for a cylindrical fabrication . . . . .	12
Figure 1.9	Optical images of inner surfaces before and after thermal annealing	12
Figure 1.10	Schematic representation of the most relevant temperature-dependent processes in fused silica . . . . .	13
Figure 2.1	Pump-probe spectroscopy schematic setup . . . . .	16
Figure 2.2	Schematic representation of THG via Second Harmonic Generation followed by Sum Frequency Generation . . . . .	17
Figure 2.3	Schematic representation of Third Harmonic Generation via $\chi^{(3)}$ materials . . . . .	18
Figure 2.4	Energy levels involved in Third Harmonic Generation . . . . .	19
Figure 2.5	Experimental setup for generation and characterization of deep ultraviolet pulses . . . . .	21
Figure 2.6	Differential pumping setup and recirculation system . . . . .	22
Figure 3.1	Schematic representation of a HHG spectrum . . . . .	26
Figure 3.2	Schematic drawings of the three-step semiclassical model . . . . .	27
Figure 3.3	Distorted coulombian potential . . . . .	28
Figure 3.4	Trajectories for different initial phases, as a function of time and in the state space . . . . .	30
Figure 3.5	Kinetic energy as a non monotonic function of the initial phase	31
Figure 3.6	Cutoff energies as a function of the laser wavelength for different noble gases . . . . .	31
Figure 3.7	Quantum levels involved in the harmonic generation under the strong field approximation . . . . .	33
Figure 3.8	Representation of an extreme nonlinear upconversion of a femtosecond laser in a gas-filled hollow channel: phase matching . . . . .	34
Figure 3.9	On axis photon flux as a function of the medium length . . . . .	35

Figure 3.10	Transmission of the fundamental mode $\text{EH}_{11}$ at 780 nm as a function of hollow fiber length for various radius of the guide and against the next high-order mode $\text{EH}_{12}$ . . . . .	36
Figure 3.11	Examples of a transverse circular electric, a transverse circular magnetic and an hybrid modes . . . . .	37
Figure 4.1	Schematic experimental apparatus for femtosecond laser writing	40
Figure 4.2	Schematic experimental apparatus for hollow waveguide characterization . . . . .	43
Figure 4.3	Schematic representation of the interaction chamber for high-order harmonic generation . . . . .	44
Figure 4.4	Three-dimensional drawings of the home-made support for the HHG chip . . . . .	45
Figure 4.5	High-order harmonic generation and acquisition schematic setup	46
Figure 5.1	CAD drawing of the differential pumping chip . . . . .	48
Figure 5.2	Beam cross sections for a focal length of 50 cm and of 80 cm .	49
Figure 5.3	Beam spot at different position over the length of the DPC . .	50
Figure 5.4	Top and front view of the glass cell for third harmonic generation	51
Figure 5.5	Gas flow through the DPC . . . . .	52
Figure 5.6	Top view and total number density along the axis of the DPC for different inlet pressures . . . . .	53
Figure 5.7	Optical images of the lines array for the etching dynamic analysis	54
Figure 5.8	Schematic draw of the upside-down glass cell with all the solution adopted for the fabrication . . . . .	56
Figure 5.9	Top view of the irradiated path for the reservoir with the cutting planes and the cell-reservoir connection . . . . .	56
Figure 5.10	Picture of the THG cell fabricated in a fused silica slab . . . .	57
Figure 5.11	Optical microscope images of the inner cell and the side of the device . . . . .	58
Figure 5.12	Picture of a fused silica slab irradiated with the geometry of the differential pumping chip . . . . .	59
Figure 6.1	(a) Scheme of the irradiation pattern for the HHG chip and (b) a picture of the device fabricated with FLICE technique. . . . .	61
Figure 6.2	Thermal treatment for the annealing of the HHG chip . . . . .	62
Figure 6.3	SEM images of the HHG chip . . . . .	62
Figure 6.4	Zero order Bessel modes of the waveguide before and after thermal annealing . . . . .	63
Figure 6.5	Zero order Bessel fitting and Gaussian fitting of the mode transverse profile before the annealing of the waveguide . . . . .	64
Figure 6.6	Gaussian fitting of the mode transverse profile after the annealing of the waveguide . . . . .	64
Figure 6.7	HHG spectra generated at different pressures . . . . .	66
Figure A.1	Fluid flow regimes . . . . .	70
Figure A.2	Scheme for the derivation of the angular coefficient method . .	71
Figure A.3	Probability density functions of the velocity modulus . . . . .	72

---

Figure A.4	Volume of gas and boundary conditions applied . . . . .	74
Figure A.5	A detail of the triangle mesh used for the simulations . . . . .	74
Figure A.6	Pressure at the walls of the device for an inlet pressure of 2 <i>atm</i>	75
Figure A.7	Total number density along the axis of the DPC for different inlet pressure . . . . .	76
Figure A.8	Total number density along the axis of the DPC for different channel diameters . . . . .	77



# List of Tables

Table 3.1	Noble gases ionization potentials . . . . .	27
Table 5.1	Measured parameters of the laser beam for two different focusing lenses . . . . .	49
Table 5.2	Lengths (in $\mu m$ ) of the etching paths over lines irradiated at different laser powers and writing speeds along the <b>x</b> direction (perpendicular to the laser polarization) after <b>1 h</b> in 20% HF solution . . . . .	54
Table 5.3	Lengths (in $\mu m$ ) of the etching paths over lines irradiated at different laser powers and writing speeds along the <b>x</b> direction (perpendicular to the laser polarization) after <b>2 hrs</b> in 20% HF solution . . . . .	55
Table 5.4	Lengths (in $\mu m$ ) of the etching paths over lines irradiated at different laser powers and writing speeds along the <b>y</b> direction (parallel to the laser polarization) after <b>1 h</b> in 20% HF solution . . . . .	55
Table 5.5	Final procedure for the fabrication of the differential pumping chip	58



# Chapter 1

## Femtosecond Laser Micromachining

### 1.1 Introduction

Femtosecond Laser Micromachining (FLM) is a technique for complex microfabrications which has been extensively used since 1996, when Hirao and co-workers [3] demonstrated that a tight focused femtosecond laser beam, with a frequency in the visible range, was able to induce permanent modification in several kind of glasses. They suggested that these damages, giving rise to an increase of index of refraction, could be used to write built-in optical circuits in bulk glasses.

In the following years, many researchers developed this idea fabricating integrated optical devices as beam splitters, directional couplers, fiber and waveguide Bragg gratings, waveguide amplifiers [4] etc..

In 2001, a breakthrough paper by Marcinkevicious et al. [5] broadened this already growing field demonstrating that a 5% of aqueous solution of HF acid was able to etch a 3D pattern written by a focused femtosecond laser, resulting in the fabrication of micrometric channels with a circular cross section inside a fused silica substrate. This made possible to fabricate articulated buried structures paving the way for Optofluidic [6, 7], a novel research field which combine optics and fluidics to build microsystems with new functionalities, which could be of interest for a wide range of disciplines.

Compared to other microfabrication techniques such as silica-on-silicon, ion exchange or lithographic methods, which are generally limited to planar structures [8], FLM is truly three-dimensional technique and allow the fabrication of articulated structures that would be otherwise impossible to obtain. By moving the sample with respect to the laser focus it is possible to quickly fabricate prototypes avoiding clean room facilities or dedicated masks and with a suitable choice of parameters it is possible to successfully irradiate different types of glasses [3, 9], crystals [10] and polymers [11]. However, most studies have focused on the irradiation of fused silica [8, 12], being a widely used optical material with a well-known structure, exceptional chemical and mechanical stability, a large transparency window (from UV to IR, covering the range of frequencies FLM typically operates with) and, last but not the least, high commercial availability.

Since all the devices realized in this work were manufactured by Femtosecond Laser

Micromachining followed by Chemical Etching (FLICE) on fused silica, it was deemed appropriate to devote the first chapter to give a deep insight into this technique, summing up the broad literature on the topic. The chapter is organized as follows: in Sect. 1.2 the physical mechanisms underlying FLM are presented while Sect. 1.3 is devoted to the chemical process and the resulting microchannels' properties.

## 1.2 Femtosecond Laser Micromachining Physics

When a material interacts with a focused femtosecond laser pulse with a high peak intensity (of the order of  $10^{13} \text{ W cm}^{-2}$  [4]) some colourless damage can be observed. The only possible explanation is that some sort of energy transfer took place during the process, i.e., the light absorption by matter.

However, the energy of the incident photon is not sufficient to excite electronic transition: if we consider a green photon, its energy is more or less  $\hbar\nu = 2 \text{ eV}$ , whereas the energy bandgap  $E_g$  (the energy difference between the valence and the conduction band) for fused silica is around  $7.5 \text{ eV}$  [13]. Moreover, the damage appears to be localized in a finite region of space, corresponding to the focal volume of the laser beam. Hence, this absorption must be the outcome of a nonlinear process, which consist in the promotion of electrons from the valence to conduction band, the following formation of an electron plasma which eventually will find a way to give up its energy to surrounding material [12].

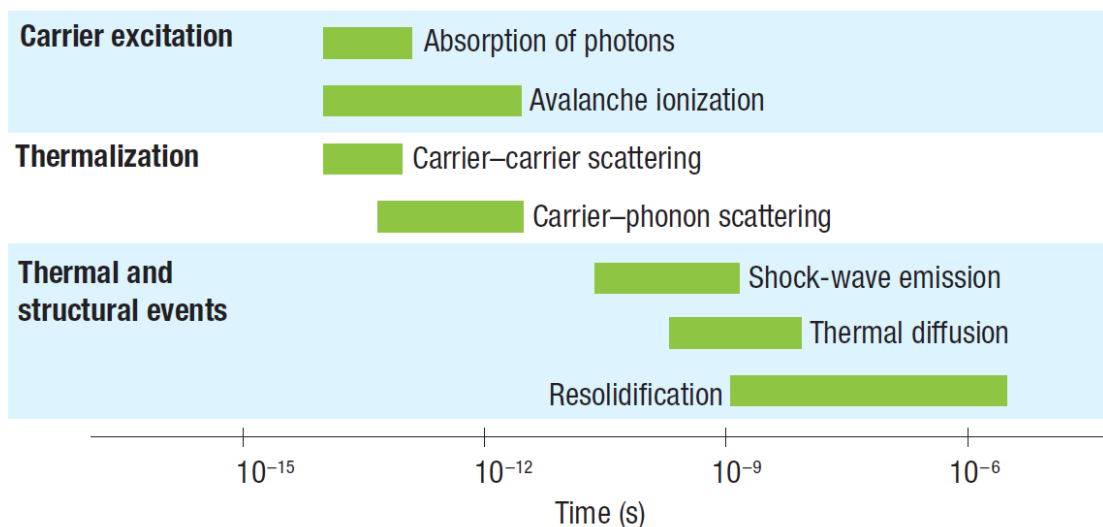


Figure 1.1. Timescale of the most important phenomena occurring in the interaction of a femtosecond laser with a transparent material. Thermal and structural events take place long after carrier excitation [14].

Physics underlying FLM is today not fully understood [4]. The modification of the transparent material depends upon many parameters, from both laser source and sample. In addition, the fast time scale at which involved phenomena occurs (cfr. fig. 1.1), makes this interaction regime difficult to be experimentally investigated and theoretically characterized.

Several models have been proposed and widely accepted for the first stage of the interaction, namely the formation of the electron plasma, whereas a more empirical approach, based on the dependence of the final modification upon the different working conditions, can be exploited to understand energy deposition and structural changes.

### 1.2.1 Carrier Excitation and Free Electron Plasma Formation

Two main nonlinear mechanisms have been appointed as the responsible of the formation of the electronic plasma [13]: *photoionization and avalanche ionization*.

The term photoionization means the direct ionization of matter by the incoming radiation. As stated before, a photon in the spectral range of interest does not have enough energy to excite a photon to the conduction band. Nevertheless, it is possible to imagine that  $n$  photons, for which holds

$$n\hbar\nu > E_g \quad (1.1)$$

where  $\nu$  is the frequency of light, could be absorbed all at once causing the excitation of one electron. This process goes under the name of *multiphoton ionization*.

A second regime is called *tunnel ionization*. In this case the electric field of the laser pulse bends the coulombian hole of atom. If the field is sufficiently high, an electron can overcome the potential thanks to the quantum tunnel effect. Both multiphoton and tunnel ionization are schematically represented in figure 1.2.

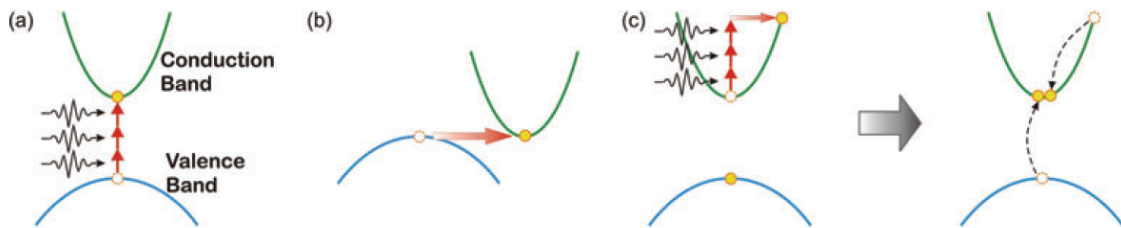


Figure 1.2. Schematics of nonlinear photoionization processes: (a) multiphoton ionization, (b) tunneling ionization and (c) avalanche ionization, consisting in free carrier absorption followed by impact ionization [15].

Interestingly, these two physical phenomena are only apparently different. As firstly demonstrated by Keldysh [16], they are just two different regimes of the same theoretical apparatus. Without entering in any detail, one can introduce the Keldysh parameter  $\gamma$ :

$$\gamma = \frac{\omega}{e} \sqrt{\frac{m_e c n \varepsilon_0 E_g}{I}} \quad (1.2)$$

being  $\omega$  the laser frequency,  $I$  the laser intensity at the focus,  $m_e$  the effective electron mass,  $e$  the electron charge,  $c$  the speed of light,  $n$  the linear refractive index and  $\varepsilon_0$  the permittivity of the free space. This parameter allows to distinguish three qualitatively different situation:

- If  $\gamma \ll 1$  tunnel ionization dominates, meaning high laser intensities and low frequencies.

- If  $\gamma \gg 1$ , multiphoton ionization dominates meaning low laser intensities and high frequencies (but still below that needed for linear photon absorption).
- If  $\gamma \approx 1$ , nonlinear photoionization can be understood as a combination of the two.

Avalanche ionization is governed by the possibility for an electron already excited at the bottom of the conduction band to linearly absorb several photons from the laser field gaining kinetic energy and becoming a so-called hot electron [4]. When its total energy exceeds the conduction band minimum by more than the bandgap energy, it can hit another electron from the valence band, resulting in two electrons near the conduction band minimum. These two electrons can in turn acquire energy from the laser pulse, become hot and excite other electrons, triggering an avalanche in which free electron population grow exponentially [15].

The electron that first generate the ionization and acts as a seed for the avalanche may come from one of the previous described nonlinear mechanism, but also from thermally excited impurities or defect states [4]. In the first case, the laser pulse must be very short (sub-picosecond duration) in order to have peak energy enough to allow multiphoton or tunnelling ionization, in the second could be involved also relatively long pulses (some tens of picoseconds or even nanoseconds). It is crucial for the technique to be successful that the case is the former: in fact, the number of impurities and dislocation within the focal volume is subject to large fluctuation, so the process of free carrier formation would be stochastic. Furthermore, when we consider a sub-picosecond pulse, absorption occurs at a time scale which is faster than the lattice heating process, that is, the electrons become hot much faster than they cool down [13], minimizing heat diffusion coming out from the focal volume. This two points, replicability and confinement, are exactly the key to transform a kind of radiation damage in a very powerful micromachining technique.

Whilst the electric field is present, a simple model for the growth of free electron population  $n_e$  could be described by an equation as [13]:

$$\frac{dn_e}{dt} = \sigma_k I^k + \eta n_e \quad (1.3)$$

where the first part of the second term represents the multiphoton ionization regime, with  $\sigma_k$  the multiphoton absorption coefficient for absorption of  $k$  photons [17], while the second term describe avalanche ionization, being  $\eta$  the avalanche ionization rate. Some authors [18] identify  $\eta$  as directly proportional to the intensity  $I$ , others [19] to  $\sqrt{I}$ .

As a result of the described processes, we have the formation of an electron plasma. To ionized matter is typically associated a characteristic frequency, called plasma frequency [20]:

$$\omega_p^2 = \frac{4\pi e^2 n_e}{m_e^*} \quad (1.4)$$

where  $m_e^*$  is the effective mass of the electron.

Plasma frequency is directly correlated with the population density. Remarkably, the population density takes the name of critical density  $n_c$  when the plasma frequency equals the one of electromagnetic field. In this case, using the laser frequency of interest and some approximation for the effective mass, it results  $n_c = 10^{21} \text{ cm}^{-3}$ . Until  $n_e < n_c$ , the plasma is *underdense* and the laser pulse cannot propagate through it, being partially reflected and partially absorbed at the surface (it is possible to show that the skin depth is of the order of tens of nanometers) but as soon as  $n_e \approx n_c$  it becomes *near critical* and some interesting phenomena lead at the laser energy to be absorbed volumetrically in all the plasma [20]. It is usually assumed that when the carrier reaches this critical value the optical breakdown occurs. In glass, the corresponding laser intensity is of the order of  $10^{13} \text{ Wcm}^{-2}$ .

### 1.2.2 Bulk Modification

In figure 1.3 are summarized the interaction physics discussed up to now.

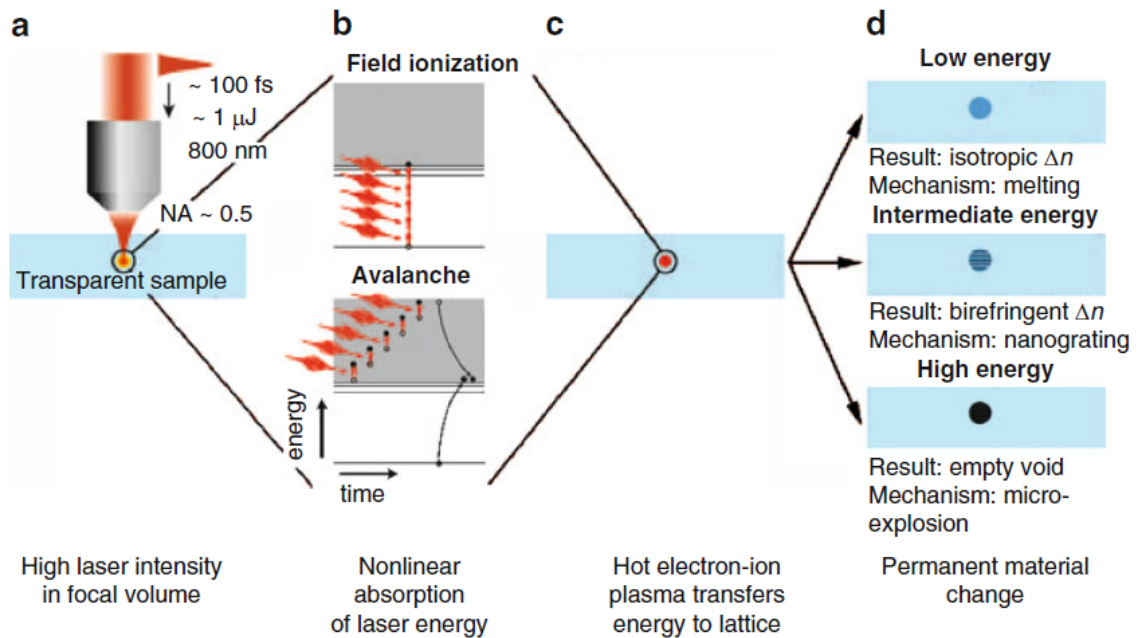


Figure 1.3. Illustration of the FLM main steps: (a) the laser is focused insight the material, (b) energy is absorbed via a nonlinear mechanism, (c) laser transfers its energy to the surrounding material resulting in a permanent modification (d) [4].

Therein, the last step, namely the permanent change of the material, is classified depending on energy of the pulse. The reason is that, despite of the great number of works published in the last two decades on this topic, the mechanisms for the material modification are not fully understood. Anyhow, it was shown that each final result falls in one of the following three groups of structural change:

1. A smooth change of the refractive index. The same research group which in 1996 firstly discovered the phenomena shown the year after that it was possible to take advantage of it to build single mode waveguides [21].

2. A birefringent refractive index change that, as will be shown, is due to the formation of sub-wavelength nanogratings which play a fundamental role for FLICE technique [22–24]
3. Empty voids due to cracks and microexplosions [25].

Which one of those regime happens to realize depends on many parameters.

First of all, it depends on the irradiated material peculiarities, such as composition, bandgap energy, thermal conductivity etc. [8].

For now on, the interest would be on fused silica ( $\text{SiO}_2$ ) which, together with Foturan (Schott) [26], is the main material used for microchannel fabrications. For  $\text{SiO}_2$ , once fixed the pulse duration and numerical aperture (NA) of the focusing objective, it is the laser intensity which dictates the regime. Starting with intensity around  $10^{11} \text{ Wcm}^{-2}$  and corresponding energies just enough to promote non-linear absorption, the material enters the smooth modification condition, which is commonly exploited to fabricate optical waveguides.

For much higher intensity, equal or bigger than  $10^{14} \text{ Wcm}^{-2}$ , pressures greater than the Young's modulus are generated in the focal volume, creating a shockwave which leaves behind a less dense core (which can be called void) surrounded by a shell of higher refractive index. Such structures can be exploited for 3D memory storage [27] and photonic bandgap materials [28], but they are not suitable for micromachining techniques, so their formation must be avoided.

When the energy is high enough to promote plasma formation but not to trigger microexplosion, interaction between the pulse and the electron leads to the formation of periodic nanostructures, which generally goes under the name of nanogratings. A qualitative and semi-quantitative explanation of this process was proposed by Taylor et al. [29] and is here summarized because nanogratings' properties will be essential to a proper understanding of the chemical etching.

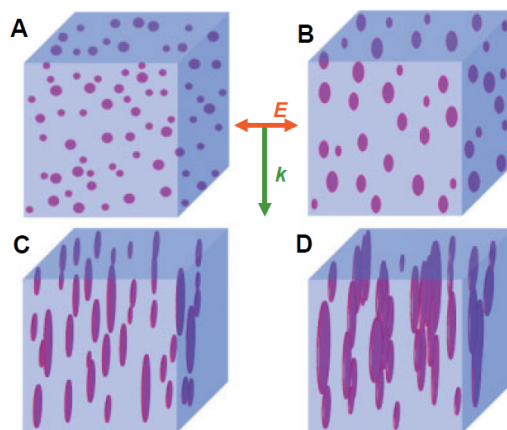


Figure 1.4. Visual representation of the nanograting formation aligned perpendicularly to the writing laser polarization, according to transient nanoplasmonic model [29].

### 1.2.3 Transient Nanoplasmonic Model

The first observation of form birefringence in fused silica dates back to 2001 [22]. Until then, only the other two regimes were known. Later it was suggested that this birefringence could be due to embedded periodic structures orientated perpendicular to the laser polarization [30]. These nanogratings were indeed found in 2003 [23].

The physical mechanism underlying the formation of nanogratings has been studied in detail [30] and a transient nanoplasmonic model has been proposed to explain their formation and subsequential self-ordering. This model involves the following steps:

1. Creation of ionization hot-spots due to nonlinear absorption, localized at defects and colour centres.
2. Evolution of the hot spots into spherically shaped nanoplasmas over several successive pulses thanks to a memory effect [31], for which in the same point where the first ionization occurred there is a reduction of the energy bandgap, and then a trending to have other ionisation in the same volume. Hence the process relies on the cumulative effect of more pulses on the same spot, therefore both intensity and translational speed will affect the process.
3. Asymmetric growth of the plasma. A laser pulse interacting with an underdense plasma induces a longitudinal mode at plasma frequency [32]. This could explain the enhancement of the field at the boundaries of the nanoplasmas which result in an asymmetric growth of the plasmas, which from spheres become ellipsoids and finally plasma disks, all oriented in a direction perpendicular to the direction of the electric field. Their elongation becomes more and more intensified as the density approaches the critical value. Eventually they are so elongated that they link together becoming nanoplanes.
4. Organization of the nanoplanes in an evenly spaced ensemble. During their growth, the nanoplasmas are randomly distributed in the focal volume. When they exceed the critical density, they start influencing the light propagation in such a way that they assemble in parallel nanoplanes spaced by  $\lambda/2n$  [33, 34] where  $\lambda$  is the wavelength.

All the steps of the nanoplasmonic model are represented in figure 1.4.

### 1.2.4 Exposure parameters

Besides pulse intensity, other variables greatly affect the result of FLM: laser source parameters, focusing condition and writing geometry.

Femtosecond laser *wavelength* is usually chosen inside the transparency window of the material to avoid undesired linear absorption. One typical choice of the early works was 800 *nm*. Shah et al. [35] demonstrated that using a 1045 *nm* fundamental frequency and doubling it with a BBO crystal, it was possible to produce lower loss waveguides.

When describing in Sect. 1.1 radiation-matter interaction, it was implicitly assumed that it was an interaction between the matter and a single pulse from the femtosecond laser. Then it was underlined how the formation of nanogratings depends on multiple pulses interaction. In any case, it must appear clear that the *repetition rate*  $f_{rep}$  of the pulses plays a fundamental role.

Having  $t_{th}$  the characteristic thermal diffusion time, it is possible to distinguish between two qualitatively different regimes: low repetition rate, for which  $f_{rep} \gg 1/t_{th}$ , and high repetition rate, for which  $f_{rep} \ll 1/t_{th}$ . The value of  $1/t_{th}$  depends on the material, for fused silica is set to  $1\text{ MHz}$ . In the first case, the time interval between two pulses is sufficient to allow the cooling of the irradiated region before the next pulse arrives. With a higher repetition rate the heat is not completely released before the next pulse arrival, leading to a progressively heating of the zone and localized melting. Operating in this regime, it was reported an increase in the size of the modified structure [13], which besides appears to be smoother thanks to the annealing effect of the heat accumulation [36]. Furthermore, when fabricating a waveguide its cross section will be more symmetric than in the low repetition rate routine, in which the laser affected zone extend also beyond the focal volume in an anisotropic way. To operate with low frequency also very low translation velocity are required ( $\sim 10\ \mu\text{m/s}$ ) whereas high frequency allow faster movement ( $\sim \text{mm/s}$ ) and thus a much faster prototyping.

Femtosecond laser pulses must be *focused* on a micrometric focal spot to overcome the threshold intensity and trigger nonlinear absorption. This can be done by means of an appropriate optical element which unavoidably brings chromatic and spherical aberration. Moreover, when the laser beam crosses the air-glass interface, index mismatch introduces other spherical aberration.

All these occurrences can wreak deviations from the usual linear propagation of a Gaussian beam [4], which is well described (at low intensity) by the paraxial wave equation [37], and consequently a lower control of shape and dimensions of the modified zone. A possible solution requires the utilization of aberration corrected microscope objectives for the wavelength spectrum of interest [4] or oil-immersion lenses. For buried structures, there is also a strong depth dependence and in general an influence from the NA of the objective, which is usually keep high to have a better precision, as it is known from Gaussian optics that both the waist radius and the Rayleigh range (which define the dimension of the focal volume) decrease as NA grows.

Furthermore, a focused beam like the ones used in FLM reaches intensities high enough to cause a nonlinear response from the matter. In particular there will be a polarization field which will depend on  $E^3$  and in turn an index of refraction

$$n(I) = n_0 + n_2 I. \quad (1.5)$$

A pulse propagating in a medium with an intensity dependent refractive index will undergo through Kerr lens self-focusing effect: the beam will see a higher refractive index at the centre and a lower one at the wings and the propagation will be similar to the crossing of a positive lens which tend to focus the propagating light. Anyway, this circumstance is dynamically countered when the electron plasma is produced and acts as a diverging lens.

Another important point is the *writing geometry*. In a typical FLM set up the sample is handled with an appropriate device, driven via software, and translated with respect to the laser focus. This movement can be along (*longitudinal geometry*) or perpendicularly (*transverse geometry*) to the laser beam.

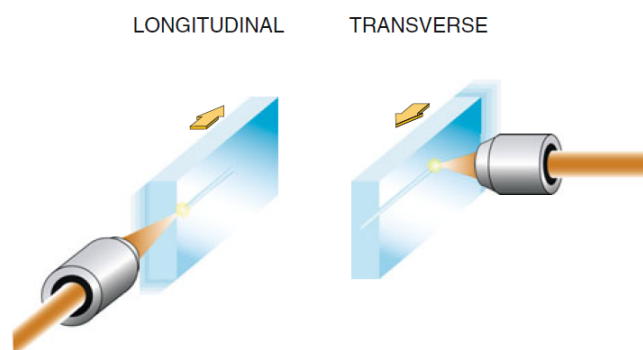


Figure 1.5. Longitudinal and transverse writing geometries [4].

In longitudinal writing, the resulting channels have a cylindrical cross section, thanks to the symmetry of the Gaussian beam, but the length is limited by the working distance of the focusing objective.

In contrast, moving the sample perpendicularly to the laser beam offers much more flexibility scanning even some centimetres of material, and changing the focus depth gives the opportunity of fabricating complex 3D structures, which in the end is the main goal of FLM.

Transverse writing has the great disadvantage of creating channel with high asymmetric cross section, due to the ratio between depth of focus and spot size. This is absolutely relevant, especially when interested in the straight fabrication of waveguides, since the number and the properties of modes supported depends also on the cross section. Various solutions have been proposed to overcome this limitation, such as the use of a slit before the focusing lens [38], the stacking side by side of different laser affected zones [39], the shaping of the focal volume by means of an appropriate focusing geometry [40] and a technique based on the use of a deformable mirror [41]. Furthermore, when the laser operates with high frequencies, the cross section appears naturally symmetric thanks to isotropic heat diffusion [42]. Transverse writing is the most adopted writing geometry for both standard FLM and the fabrication of hollow microchannels.

Also the formation of nanogratings is sensitive to writing direction: the coherent linkage between nanoplanes occurs only if they are all aligned, as in the case of transverse writing (fig. 1.6). This plays a fundamental role in determining the etching velocity.

As a final observation, it is worth noticing that in any case must be avoided the overwriting of the same area: when moving through an already altered zone, the focus will undergo a distortion which in turn will spoil the desired modification.

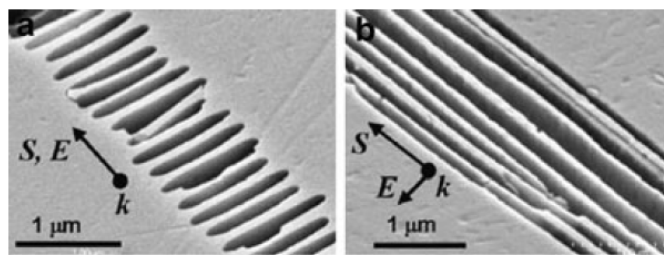


Figure 1.6. Scanning electron images of nanogratings formed with writing direction (a) parallel and (b) perpendicular to the electromagnetic field [4].

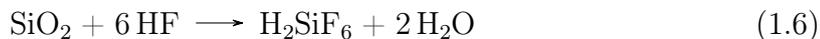
### 1.3 FLICE (Femtosecond Laser micromachining followed by Chemical Etching)

Femtosecond Laser micromachining followed by Chemical Etching (FLICE) technique consists in the etching of the femtosecond pulses irradiated zone with an opportune solvent, commonly an aqueous solution of Hydrofluoric acid (HF).

With FLICE it is possible to directly fabricate buried microfluidic channel in fused silica. The first step of this technique is exactly FLM described with some detail in the previous section. The key idea behind FLICE is that in fused silica the zone modified by the laser is etched with a velocity up to two order of magnitude compared to the unaffected zone [4], enabling the manufacturing of microchannels.

#### 1.3.1 Chemical Etching

Fused silica has an amorphous molecular structure, meaning there is no long-range order, which is instead typical of the crystalline form of  $\text{SiO}_2$ . However, it is possible to identify a basic unit, formed by a Si atom surrounded by four O atoms, connected by covalent  $-\text{Si}-\text{O}-\text{Si}-$  bonds. HF, being a weak acid, partially dissolves in water, producing  $\text{F}^-$ , which cause the nucleophilic attack on the silicon atoms, and a proton, which electrophilic attack on oxygen [43]. The dissolution of fused silica is described by the reaction [44]:



In order to understand how the photomodification enhance the reaction it's useful to refer to the first two regimes introduced in Sect. 1.2.2.

In the first regime it is observed a slight modification of the affected area and also a slight increase in the etching velocity. This is probably due to a straining of the  $-\text{Si}-\text{O}-\text{Si}-$  bond, which makes the oxygen atom more exposed to protonation. However, more studies on the molecular dynamics are needed to validate this conclusion [43]. At higher pulse intensities nanoplanes start to grow and with them the etching rate. This can be justified thinking at the nanoplanes acting as channels for diffusion of the acid deeper in the fused silica. The acid moves faster where the nanoplanes are present and etches the irradiated path before the unaltered area [4]. This interpretation is confirmed by changing the writing geometry: selecting a longitudinal irradiation, nanocracks does not link together and the diffusion cannot take place. This is indeed validated by experimental results, as shown in fig. 1.7.

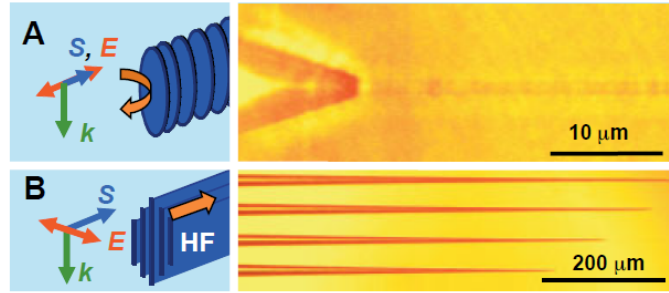
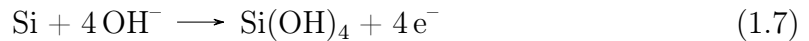


Figure 1.7. Etching effectiveness for different writing geometries. For FLICE to be successful, laser motion must be perpendicular to the field polarization [29].

An unwanted characteristic of the etching with HF is the process self-termination due to the piling up of reaction product and the difficulty to refresh the acid in the microchannel depth. To promote the refreshing and to increase the homogeneity of the result, the etching process is usually performed in an ultrasonic bath. Other parameters which can affect the process are temperature and acid concentration.

To current understanding, there are no differences in the reaction with HF of fused silica before and after the irradiation, and the differences in etching rates are basically due to structural changes. Some studies [45, 46] propose that the laser pulse actually changes the composition of the material with the formation of  $\text{SiO}_x$ , with  $x < 2$ . Then it would be useful to choose a solvent more effective to Si-rich compounds. This is the case of KOH, which acts on Si-Si bonds through the reaction:



Notwithstanding a marked increase in reactivity is observed, KOH is still not so used because of its very low action on unaltered  $\text{SiO}_2$ , which makes it very difficult to start the etching. To overcome this limitation, it is possible to consider a first step of HF etching followed by a second one with KOH, but this means an extension of the overall times. Another possibility involves some preliminary lapping process.

Furthermore, reaction with KOH is not self-limiting and does not produce substances potentially dangerous to humans, conversely to HF which must be always handled with caution and under fume hood.

### 1.3.2 Channel Properties

One known characteristic of HF etching of fused silica is the self-limitation of the reaction due to saturation of the solution. To delay this circumstance and obtain longer channels, one can increase the concentration of HF in solution, but still the buried channel will be limited to a maximum length of around 2 mm. In general, etching rate drops as the diffusion path increases. This has a consequence on the shape of the microchannel: if a cylinder is irradiated, a truncated-conical channel will be obtained after the etching, because the outer section will be exposed for more time to a more effective carving action. To take into account this effect, it is necessary to irradiate a conical shape instead of a cylinder.

Depending on the desired geometry, it is possible to consider additional inlets for the HF (*etching channels*) in other points of the waveguide. In this case it is necessary to modulate the diameter of the cone in such a way to have minima corresponding to etching channels to achieve the most symmetric result. In figure 1.8 is irradiated also a line in the axis of the cylinder whose purpose is make easier the removal of the internal volume. For greater guides could be relevant the fabrication of cutting planes perpendicular to the axis to split the residual glass in more parts easier to pull out.

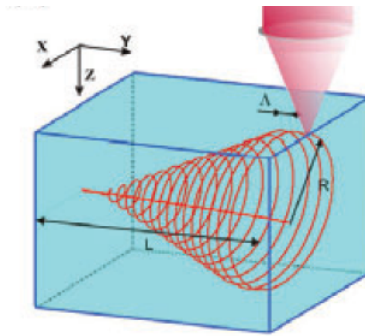


Figure 1.8. Schematic writing pattern for a cylindrical fabrication [15]. Parameters like the helix pitch must be chosen to allow a full removal minimizing the irradiation time.

### 1.3.3 Surface Roughness and Glass Annealing

After the etching process, internal structures usually shows a certain surface rugosity (see fig.1.9) which can be detrimental in most optical applications [47], like light scattering, total internal reflection or light confinement [48].

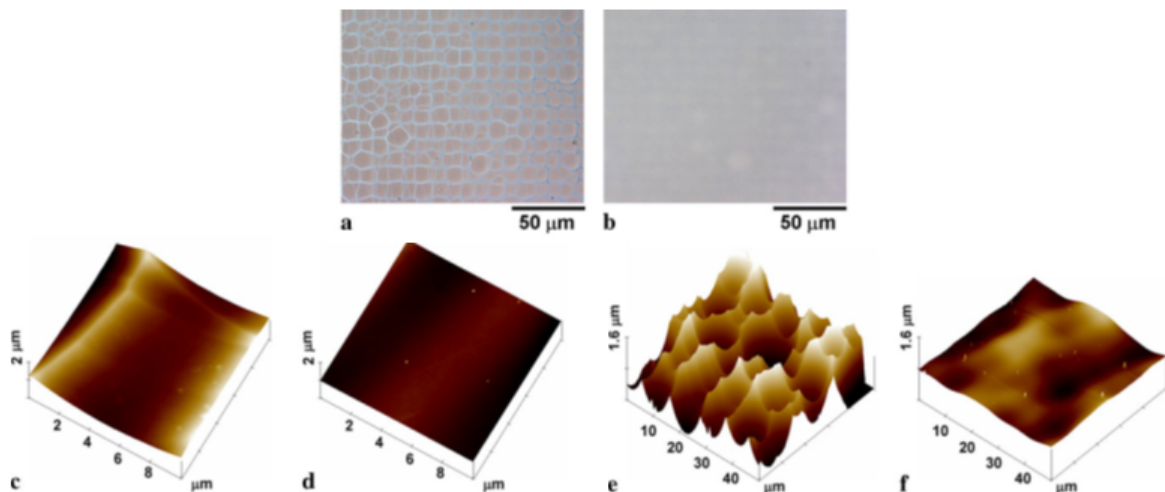


Figure 1.9. Optical images of inner surfaces (a) before and (b) after thermal annealing. Scanning-probe microscope images of a  $10 \times 10 \mu\text{m}^2$  (c) before and (d) after the annealing; (e) and (f) represent the same surface on a larger area of  $50 \times 50 \mu\text{m}^2$ . Here, rugosity was reduced from some hundreds of  $\text{nm}$  to few  $\text{nm}$  [47].

### 1.3. FLICE (Femtosecond Laser micromachining followed by Chemical Etching)

This rugosity can be in principle minimized optimizing the pulse energy, the polarization of the electric field, the focal spot shape or the scanning parameters. Also increasing etching time and more in general the surface of the carved area can improve the smoothness, whereas there is no direct correlation between rugosity and HF concentration [44].

However, in practice is not always possible to optimize all these parameters according to the fabrication requirements and some roughness (tens or hundred of nanometers) is usually still present. To obtain the desired evenness, some annealing techniques could be required.

The aim of a thermal treatment is to relax surface and internal stresses. When a silicate glass is heated, a number of physical and mechanical processes occur depending on temperature and anneal time, as summarized in fig. 1.10. For relatively low temperature (400 °C) isolated point defects are annealed. At higher temperatures and longer times it is possible to reconstruct higher densities of defects. At around 1000 °C external tensions start to relax and reaching 1200 °C also the mechanical stresses in the bulk of the material are relieved. If the temperature is raised further (1600 °C) the material start to soften and eventually to melt [49].

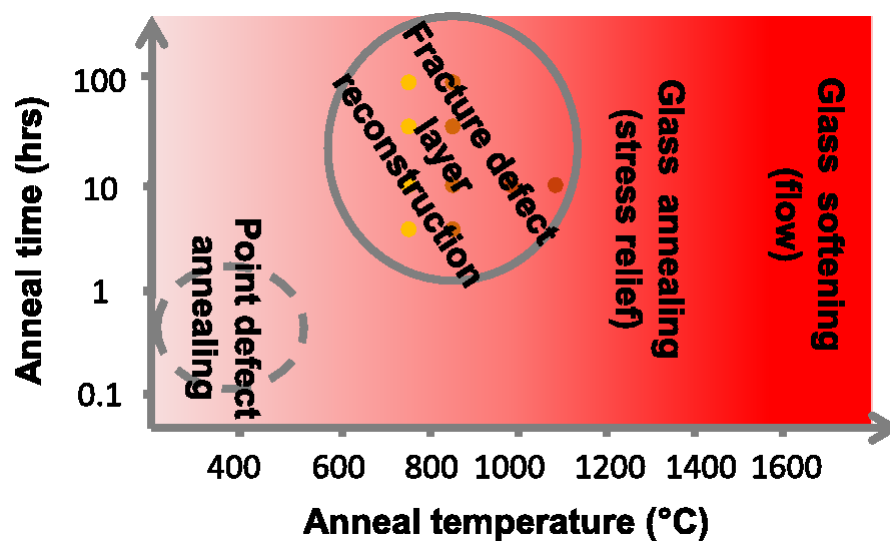


Figure 1.10. Schematic representation of the most relevant temperature-dependent processes in fused silica [49].

During a thermal treatment, the sample is brought over annealing temperature without reaching the softening point. The process is controlled designing an appropriate succession of plateaus and ramps, which raise and decrease smoothly to avoid any kind of shock that can cause cracks. Cracks can be also induced by some dirt, then the glass must be carefully cleaned before the operation and so must the furnace. The whole procedure can last even some days. An example of a specific thermal treatment is given in Chapter 6.



# Chapter 2

## Few-Femtosecond Deep UV Generation

### 2.1 Introduction

The generation of very short pulses has been extensively exploited in the last decades to investigate a wide range of ultrafast processes occurring in nature [50]. A renowned scheme for such an ultrafast measurement is the so-called pump-probe spectroscopy (fig. 2.1): a strong laser pulse, the pump, excite the sample, generating a non-equilibrium state; a second delayed beam, the probe, is used to monitor the pump induced changes in the optical properties. Measuring this changes as a function of the delay time between the arrival of the two pulses, it is possible to study the subsequent evolution of the system. The resolution of this technique naturally depends on the duration of the involved pulses.

It is possible to estimate the time  $T$  needed to resolve an energy difference  $\Delta E$  between two discrete states as  $T = h/\Delta E$ , where  $h = 4,13 \text{ eV s}$  is the Planck constant. Then a molecular transition, with a  $\Delta E$  of some  $meV$ , will be investigated by a picosecond pulse; an electron of an atom or an ion in a valence level with energy around  $0.1 \text{ eV}$  will need a pulse of some tens of  $fs$ ; an internal electron with energy of  $10 \text{ eV}$  a sub-femtosecond pulse, and so on. Since the pump could trigger a transition at a different frequency of the optical one which involve the probe, the pulses should be tunable over a wide range of frequencies.

Nowadays, attosecond science can provide sub-femtosecond and tunable pulses in very different regions of the electromagnetic spectrum. The production of Extreme UV (EUV,  $30\text{-}150 \text{ eV}$ ) is routinely done [51, 52] since the first years of this millennium via High-order Harmonic Generation (HHG), which will be treated in detail in the next chapter. EUV attosecond pulses typically are combined with the Near Infrared (NIR,  $0.9 - 1.6 \text{ eV}$ ), which acts as the driving radiation in HHG process, in a pump-probe scheme. EUV-EUV pump-probing would guarantee a higher temporal resolution but is still challenging due to the low photon fluxes produced with HHG and low interaction cross section of EUV radiation with matter. Recently, attosecond pulses have been produced in Vacuum UV (VUV,  $10\text{-}30 \text{ eV}$ ) [53] and in the Soft X-Ray (SXR,  $300\text{-}3000 \text{ eV}$ ) [54], opening exciting paths for the real time observation of a multitude

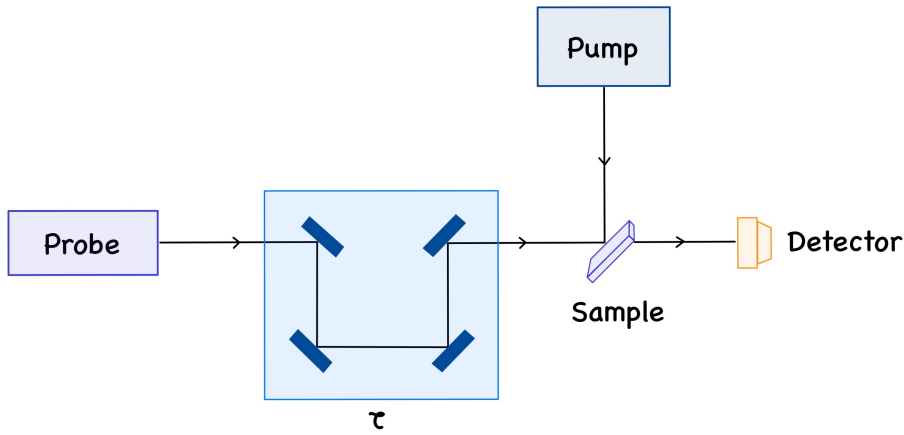


Figure 2.1. Pump-probe spectroscopy schematic setup. A variable delay  $\tau$  can be introduced between the two pulses to investigate all the analyte's dynamics.

of fundamental physical phenomena. Furthermore, SXR in the water window region will permit in-vivo observation of biological cycles. Few-femtosecond NIR and Visible pulses are instead ordinarily produced with hollow-core fiber compression [55] and filamentation [56].

Besides the aforementioned regions of the spectrum, there is another particular range of frequencies which can photoexcite neutral molecules and trigger processes of capital importance in chemistry and biology. This is the UV region from 150 to 300 eV, which in this work will be referred as Deep UV region (DUV). A remarkable example: DUV absorption leads to electronic excitation of nucleotides and then of DNA and RNA. Excess energy finds highly efficient pathways to relax through non-radiative decay: if it were not, radiation would probably damage the most important molecules for any living organism [57]. Some authors state that since life on Earth started under intense UV irradiation, this exceptional photostability of nucleotides is what makes them the building blocks of DNA and makes possible life as we know [58].

To study this phenomenon, a promising scheme is exactly a pump-probe experiment with, for example, a DUV pump and an XUV probe. Unluckily, ultrashort DUV generation is still extremely challenging. An important result is due to Galli et al. [1] which in 2019 reported a few femtosecond pulses in the range from 210 to 340 nm with a scheme that seem very promising for ultrafast measurements but still need to be optimized to reach an adequate photon flux. In this work is proposed a new photonic device aiming at increasing the performances of this setup, which will then be analysed in this chapter.

In Sect. 2.2 is presented the physical phenomena generating DUV radiation, highlighting the rationale behind the choose of one of this, namely the generation of the third harmonic. Both a classical and a quantum-mechanical interpretation of this process are also given. In Sect. 2.3 is described the setup used in [1] with a particular focus on the bulk differential pumping system that in this thesis is planned to be overcome.

## 2.2 Third Harmonic Generation in Gases

Nowadays, there are several ways to produce deep UV radiation pulses with duration of tens of femtosecond and even sub 10  $fs$ . For example, through optical parametric amplification of pulses confined in gas-filled capillary [59], waveguides nonlinear broadening in hollow fiber and subsequent compression [60], chirped pulse four wave mixing [61], direct frequency up-conversion in crystal [62] or dispersive wave emission in gas filled hollow-core crystal fibers [63].

Among all these techniques, the ones using gases as generating media produce the shortest pulses, since in solid the dispersion induced during propagation set a lower limit for the pulse duration. To reach the femtosecond goal, Third Harmonic Generation (THG) in gases is spotted as the most promising technique. In 2010, Reiter et al. reported the generation of pulses with a duration of about 2.8  $fs$  pulse and a wavelength distribution between 230 and 290  $nm$  via direct frequency upconversion of a sub-4  $fs$  NIR pulse focused in Krypton [64]. This record was broken in 2019 by Galli et al., who reached 1.9 femtosecond pulses in a spectrum between 210 and 340  $nm$  [1].

THG is a nonlinear optical phenomenon where light of angular frequency  $\omega$  is converted into light with a three-time higher frequency [65]. There are two ways to obtain such a frequency tripling.

One consists in a multi-stage scheme starting with Second Harmonic Generation (SHG) followed by Sum Frequency Generation (SFG), an optical phenomenon exploited to sum the driving radiation with  $2\omega$  second harmonic (fig. 2.2). Actually, this is the most common method to obtain UV radiation, because of relatively high efficiency conversion of this two steps provided by birefringent phase matching [66]. Indeed, both SHG and SFG are second order nonlinear processes, based on the susceptibility  $\chi^{(2)}$  of optical media, which is higher than the third order susceptibility  $\chi^{(3)}$ . But if the interest is in getting very short up-converted pulses, one must take into account that traversing two crystals will strongly limit the pulse duration, for the reason stated before. Then THG in gases must be considered because, even if based on a third order non-linearity, it can be performed in quasi dispersion-free noble gases.

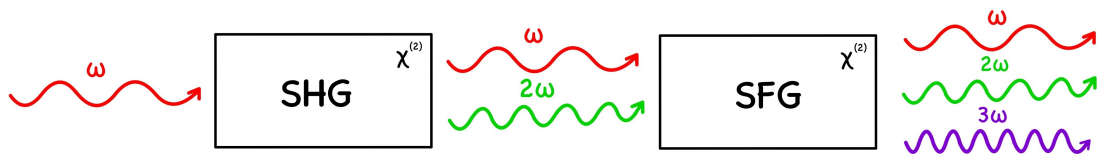


Figure 2.2. Schematic representation of THG via Second Harmonic Generation followed by Sum Frequency Generation.

THG in gases by a focused laser beam was firstly reported by New and Ward in 1967 [67] and a detailed mathematical description of this generation event was given by the same authors two years later [68]. Their goal was not as much generation of ultra-short pulses as the derivation of atomic and molecular coefficients from experimental data to compare with theoretical quantum-mechanical predictions, which are more amenable for gases than for solid, retracing what was previously done for SHG. They developed a

semi-classical model presenting the atomic system quantum mechanically and treating the radiation field classically. Different authors broaden their model, but to take into account other aspects such THG from the vacuum field or statistical properties of the generated light, a full quantum-mechanical perspective must be adopted, as firstly suggested by Nayak [69].

To have a more clear understanding of THG, two different formulation of the problem are here proposed: the first is completely classical, aiming at the writing of a wave equation for  $\chi^{(3)}$  materials [65], the second consider a possible Hamiltonian for the system made up of the quantized electromagnetic field and the two-level atom.



Figure 2.3. Schematic representation of Third Harmonic Generation via  $\chi^{(3)}$  materials.

### 2.2.1 Classical Formulation

In a complete classical picture, one can look at the generated third harmonic as a new frequency developed by the polarization  $\mathbf{P}$  of the material that was not present in the original electric field.  $\mathbf{P}$  must be understood as the electric dipole moment per unit volume, then something related to the averaged charge density of the medium. Under the assumption of no free charge and no free current, macroscopic Maxwell equations holds:

$$\nabla \cdot \mathbf{D} = 0 \quad (2.1)$$

$$\nabla \cdot \mathbf{B} = 0 \quad (2.2)$$

$$\nabla \times \mathbf{E} = -\frac{1}{c} \frac{\partial \mathbf{B}}{\partial t} \quad (2.3)$$

$$\nabla \times \mathbf{H} = \frac{1}{c} \frac{\partial \mathbf{D}}{\partial t} \quad (2.4)$$

being  $\mathbf{E}$  the electric field,  $\mathbf{H}$  the magnetic field,  $\mathbf{D}$  the electric flux density and  $\mathbf{B}$  the magnetic flux density, which can be taken as equal to  $\mathbf{H}$  in a typical optical material, which is nonmagnetic.  $\mathbf{D}$  is defined as  $\mathbf{D} = \mathbf{E} + 4\pi\mathbf{P}$ . Taking the curl of the Faraday law (2.3), using (2.4) and remembering the vectorial identity for the vector field  $\mathbf{E}$ :

$$\nabla \times \nabla \times \mathbf{E} = \nabla(\nabla \cdot \mathbf{E}) - \nabla^2 \mathbf{E} \quad (2.5)$$

it is obtained:

$$\nabla^2 \mathbf{E} - \frac{1}{c^2} \frac{\partial \mathbf{E}}{\partial t} = \frac{4\pi}{c^2} \frac{\partial^2 \mathbf{P}}{\partial t^2}. \quad (2.6)$$

Note that  $\nabla \cdot \mathbf{E}$  is not null as it is in linear optics, but still its contribution is negligible. The key point to solve this equation is to find a way to express the polarization field

as a function of the electric field. Without doing any assumption on the material,  $\mathbf{P}$  can be written as a series:

$$\mathbf{P}(t) = \chi^{(1)}\mathbf{E}(t) + \chi^{(2)}\mathbf{E}^2(t) + \chi^{(3)}\mathbf{E}^3(t) + \dots \quad (2.7)$$

The first term on the right is the only one considered in linear optics, thus  $\mathbf{P}$  and  $\mathbf{D}$  can be written as the sum of two terms:

$$\begin{aligned} \mathbf{P} &= \mathbf{P}^L + \mathbf{P}^{NL}, \\ \mathbf{D} &= \mathbf{D}^L + 4\pi\mathbf{P}^{NL}, \end{aligned}$$

with

$$\mathbf{D}^L = \mathbf{E} + 4\pi\mathbf{P}^L.$$

Then

$$\nabla^2\mathbf{E} - \frac{1}{c^2}\frac{\partial\mathbf{D}^L}{\partial t} = \frac{4\pi}{c^2}\frac{\partial^2\mathbf{P}^{NL}}{\partial t^2} \quad (2.8)$$

which is the most general wave equation in nonlinear optics. If considering THG,  $\mathbf{P}^{NL}$  will be proportional to  $\mathbf{E}^3$  through  $\chi^{(3)}$ , which will be a four rank tensor. Its 81 elements (which are not all independent if the assumption of isotropic material can be made, as it is usually the case for optical materials) are defined by the properties of the material in which the process is host. If the material is dispersive,  $\chi^{(3)}$  will depend on the electric field frequency. Choosing a model to represent the optical material, one can solve the nonlinear wave equation and find the generated third harmonic field.

### 2.2.2 Quantum Formulation

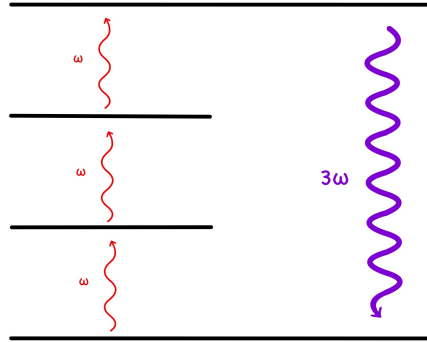


Figure 2.4. Energy levels involved in Third Harmonic Generation.

The Hamiltonian for THG – and similarly for the generation of  $n$  harmonics – can be written by analogy to the one for second harmonic generation and degenerate parametric down conversion, which is one of the most analysed Hamiltonian among nonlinear optical processes:

$$\hat{H}_{SHG} = \hbar\omega\hat{a}_1^\dagger\hat{a}_1 + 2\hbar\omega\hat{a}_2^\dagger\hat{a}_2 + i\hbar\chi(\hat{a}_1^2\hat{a}_2^\dagger - \hat{a}_1^{\dagger 2}\hat{a}_2) + (\hat{H}_{LOSS}) \quad (2.9)$$

Here, two photons in the fundamental mode  $a_1$  can annihilate to produce a photon in the second harmonic mode  $a_2$ .  $\hat{a}^\dagger$  e  $\hat{a}$  are the creation and annihilation operators

which product, in the second quantization language, is the number operator and it is multiplied by the photon energy in each mode.

In addition to SHG, this Hamiltonian includes the possibility that two photons of the field at the double frequency can be converted in one photon of the fundamental field, a process known as degenerate parametric down conversion. The coupling constant of the interaction obviously depend on the nonlinear susceptibility. The term  $\hat{H}_{LOSS}$  can be introduced to take into account losses which will give rise to cavity dumping constants.

The natural extension for THG is:

$$\hat{H}_{THG} = \hbar\omega\hat{a}_1^\dagger\hat{a}_1 + 3\hbar\omega\hat{a}_3^\dagger\hat{a}_3 + i\hbar\chi(\hat{a}_1^3\hat{a}_3^\dagger - \hat{a}_1^\dagger\hat{a}_3) + (\hat{H}_{LOSS}) \quad (2.10)$$

For which analogous comments hold. This Hamiltonian can be studied in several ways [70] and some interesting feature of the phenomenon can be retrieved. For example, numerical investigations led to the distribution function of the photon number and phase generated in THG [71] or considering photon statistics it was predicted that THG can be a source of sub-poissonian light [72].

## 2.3 Experimental Setup for Generation of Deep Ultraviolet Sub-2-fs Pulses

In fig. 2.5, it is schematically shown the experimental setup used for generation and characterization of the 1.9 *fs* pulses used in [1].

The driving laser delivers 5-*fs* NIR (770 *nm*) pulses which are partially send to interaction chamber for THG while the remaining are used to both temporally characterize the UV radiation and to perform pump-probe experiment. In future this setup will be developed and the NIR beam will be used to generate XUV attosecond pulses through HHG.

THG is induced in the glass cell shown in figure. The chip, fabricated with FLICE technique (cfr. Chapter 1), is 3 *mm* long and has a cross section of 1-*mm* diameter in the central part, which is progressively reduced to 400  $\mu m$  in the extremities (fig. 2.5 (b)). This design is optimized to confine the gas in the core of the chip. It is filled with argon by a 3 *mm* metallic tube directly glued on it and it is accommodated in a small chamber composed by three differentially pumped section, which will be analysed with some detail in the following.

The cell acts like a reservoir for the gas and is not waveguiding. A future improvement could be making the cell able to guide the beam. Doing so, the electromagnetic beam could maintain its cross section without beam spreading due to diffraction and this would increase the volume of interaction and the generation efficiency. In the current configuration, the beam is focused on a waist of  $50 \pm 5 \mu m$ , with a peak intensity in the range of 1 to  $5 \times 10^{14} Wcm^{-2}$ .

The residual NIR which is present after the UV generation is suppressed by 4 order of magnitude by three dichroic wedged beam separators, preserving the 85 % of the third harmonic beam.

All the apparatus is kept under vacuum condition to avoid dispersion of the UV pulses.

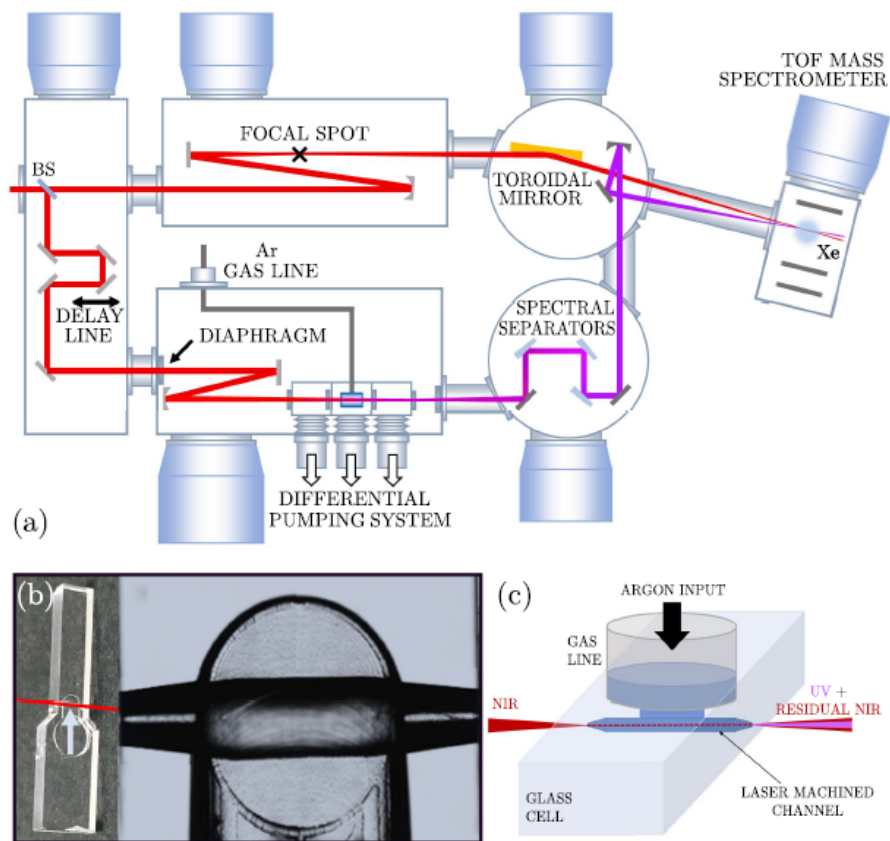


Figure 2.5. (a) Experimental setup for generation and characterization of deep ultraviolet pulses. Red line represents the NIR beam, purple one the DUV beam. (b) Picture and optical image of the glass cell used to confine THG gas. The red line represents the laser propagation direction, the arrow the gas flow. (c) Schematic representation of the gas cell [1].

### 2.3.1 Bulky Differential Pumping and Recirculation System

To ensure the maximum conversion of the fundamental frequency in the third harmonic, a high number density of argon molecules should be present in the THG chip. At the same time, it was stated that all the chamber – and the interaction chamber in particular – should be held in high vacuum condition. To find a trade-off between these two contrasting requirements, the glass cell is placed in the central of three sub-chambers, which are depicted in fig. 2.6.

The gas is injected with precision into the cell thanks to a manual valve (1). A first roots pump (2) collects most of the outflowing gas from the central sub-unit, which is connected through 0.8 mm diameter apertures to the later sub-chambers. Here the residual gas is evacuated by a second root pump (3), which is also used for backing the sealed pump maintaining the main chamber at  $10^{-4}$  mbar. With this system, it has achieved a residual gas pressure of  $10^{-3}$  mbar even when there are several bars of gas inside the THG cell. To further optimize the spatial confinement of the gas, small diameter apertures are installed also between the interaction chamber and the adjacent chambers which acts as supplementary differential pumping elements.

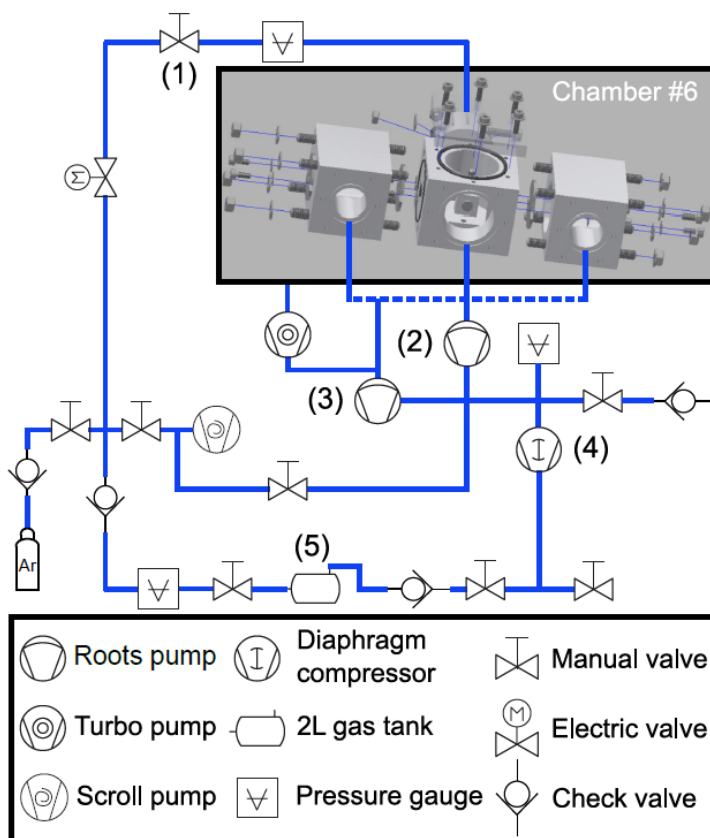


Figure 2.6. Differential pumping setup and recirculation system.

Such a system would have entailed an incredible high argon consumption if an appropriate recirculation system were not considered. The exhausts lines are then connected to a diaphragm pump (4) which compresses the gas into a 2-litre tank

(5) to a pressure up to 7 *bar*. Several valves and pressure gauges are placed up and downstream to guarantee the right flow direction. The compressed gas is then sent back to the THG chip, ready to operate again. This recirculation system has proved itself highly efficient, preserving the 96 % of the initial argon pressure after 3 hours of operation and ensuring a consumption of 0.027 *L/h*, while the bare apparatus consumes the unsustainable amount of 40 *L/h* of argon.



# Chapter 3

## High-Order Harmonic Generation

### 3.1 Introduction

Over the course of this work, much was said about the interaction between a tightly focused ultrashort laser pulse and matter, presenting the possibility of perform microfabrications and generate deep UV. Nevertheless, one of the most interesting phenomena one can address in this framework was not explored so far.

High-order Harmonic Generation (HHG) is a highly nonlinear effect which generates coherent radiation in the form of high-order harmonics of the driving laser frequency with a duration of attosecond ( $10^{-18}$  s) timescale. It allows the production of extreme ultraviolet (EUV) and soft X-ray (SXR) radiation in the form of a train of attosecond pulses, both spatially and temporally coherent, which can be used as a probe to investigate a number of phenomena in atomic, molecular and solid-state physic. Thanks to HHG a new branch of physics, which is usually called attosecond science, or attophysics, was established [51, 73].

A typical spectrum of high-order harmonics is schematically shown in fig 3.1. It consists of three regions: firstly, a fall-off of two or three order of magnitude extending for some harmonics; then a plateau in which the intensity remains more o less constant covers several hundreds or even thousands of harmonic orders; lastly, a sharp cut-off abruptly interrupts the spectrum [74]. Remarkably, only odd harmonics of the fundamental frequency are generated in this process.

Indeed, even these general features remain true, the HHG spectra highly depends on the generating medium (which is usually in a gaseous state but could be also a liquid or a solid) and on the operating conditions. Typically, laser peak intensities between  $10^{13}$  and  $10^{15}$   $W/cm^2$  are needed, bringing the interaction in a strongly non-perturbative regime.

The first observations of HHG dates to the late eighties, when McPherson et al. generated up to the 17<sup>th</sup> harmonic (14.6 nm) of a 248 nm KrF driving laser [75], and Ferray and co-workers until the 33<sup>rd</sup> harmonic (32.2 nm) of a Nd:YAG laser at 1064 nm [76]. In the following years it was possible to reach higher and higher frequency, in the effort of extending the plateau region, mainly thanks to the availability of sub-ps

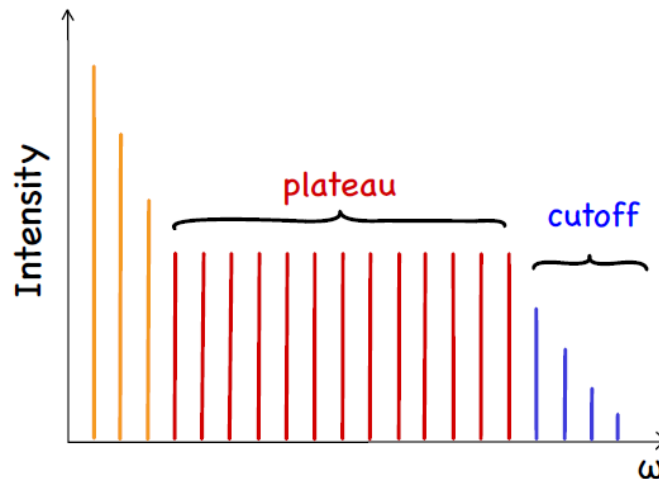


Figure 3.1. Schematic representation of a HHG spectrum. Each bar represent one harmonic. Characteristic plateau and cut off region are highlighted.

and then *fs* laser pulses.

In the last decades, many efforts have been addressed to develop an appropriate theoretical description of such a fascinating phenomenon. In fact, HHG cannot be simply understood as the absorption of  $n$ -photon like in second or third harmonic generation. This interpretation is indeed coherent with the initial decrease of the spectrum, since the probability of absorbing  $n$  photon decrease exponentially with  $n$ , but does not explain the plateau and the abrupt cut-off.

One of the most appreciated theoretical pictures is the so-called three-step model [77, 78], which is simple to be understood and clarifies HHG key aspects with semi-classical arguments. It will be presented in Sect. 3.2. A highly successful and semi-analytical quantum theory was proposed by Lewenstein [79] and is here reposed in Sect. 3.3. This model is still semi-classical since the driving and the emitted electromagnetic field are not quantized. A full quantum model requires quantum electrodynamics (QED), or better strong-field quantum electrodynamics (SFQED), to properly consider the quantum-optical nature of the interaction [80].

In Sect. 3.4 are introduced the main experimental techniques that have been used to boost HHG process, producing brighter harmonics with more efficiency, extending the plateau region to higher and higher frequencies. A special attention will be devoted to the benefits of constrain the generated gas inside a hollow waveguide.

## 3.2 Three-Step Model

To have a first glimpse of the physics underlying HHG, it is possible to assume the harmonics as generated by a single atom. This is in general not true, since HHG is the response to the laser stimulation of the medium as a whole, but microscopically it is in any case meaningful to focus on the single-atom response [81]. Referring to fig. 3.2, an outer-shell electron of the atom feels the coulomb potential modified by the laser electric field and can undergo tunnel ionization, with a high probability only when the

driving field is close to the peak during an optical cycle. Therefore, the electron can move in the continuum: initially it is accelerated away from the nucleus, then, when the electric field changes its signs, it decelerates and then accelerates again in the opposite direction, until it eventually recollides with the nucleus. During this process, the electron may have gained a significant amount of kinetic energy, which can be released together with the ionization potential in the form of high energy photons with sub-cycle durations at the time of recombination.

So this are the three steps: ionization, motion in the driving field, recombination.

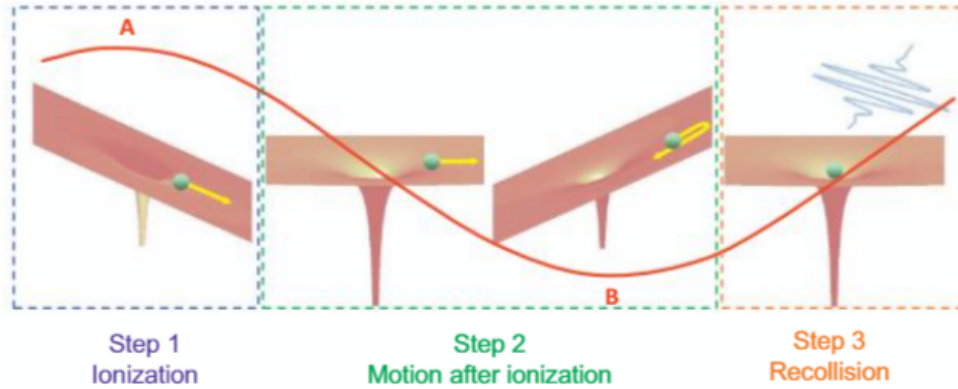


Figure 3.2. Schematic drawings of the three-step semiclassical model: a) tunnel ionization b) motion after ionization in electric field c) recollision and harmonic emission [74].

### 3.2.1 Ionization

In Chapter 1, it was introduced Keldysh theory referring to ionization of fused silica. The same theory holds for noble gases, which are usually employed to generate high-order harmonics, having an ionization potential (reported in table 3.1) much higher than the energy of the driving laser (usually, less than 2 eV).

	$I_p$ (eV)
<b>He</b>	24.587
<b>Ne</b>	21.564
<b>Ar</b>	15.759
<b>Kr</b>	13.999
<b>Xe</b>	12.129

Table 3.1. Noble gases ionization potentials [74].

The ionization then happens via tunnel ionization, being the Keldysh parameter  $\gamma \ll 1$ . In this contest,  $\gamma$  is usually rewritten as [82]:

$$\gamma = \sqrt{\frac{I_P}{2U_P}} \quad (3.1)$$

being  $I_p$  the ionization potential and  $U_p$  the ponderomotive force, defined as:

$$U_P = \frac{(eE_0)^2}{4m\omega_0^2} \quad (3.2)$$

which is the mean kinetic energy acquired by an electron oscillating in the laser field. Here,  $e$  and  $m$  are the charge and the mass of the electron whereas  $E_0$  e  $\omega_0$  are the energy and the frequency of the driver. This expression can be used to qualitatively understood the difference between the two regimes. In fact, (3.1) can be re-expressed as:

$$\gamma = \omega_0 \frac{\sqrt{2I_P}}{E_0} \approx \omega_0 \tau \approx \frac{\tau}{T_0} \quad (3.3)$$

where  $\tau$  is the time needed to overcome the potential barrier, estimable as the ratio between the thickness and a mean velocity of the electron. Of course, this concept is quite a stretch in a pure quantum process, nonetheless one can think at the distorted potential as oscillating at the laser frequency. So, if  $\gamma \gg 1$ , then  $\tau \gg T_0$ , meaning the electron does not have enough time to escape the potential well which is changing too fast, remaining trapped inside as there is no external field, at least as long as multiphoton ionization occurs. Conversely, a small  $\gamma$  means a  $\tau$  short enough to allow the particle tunnelling and only in this case the electron can start the movement in the electric field mentioned above.

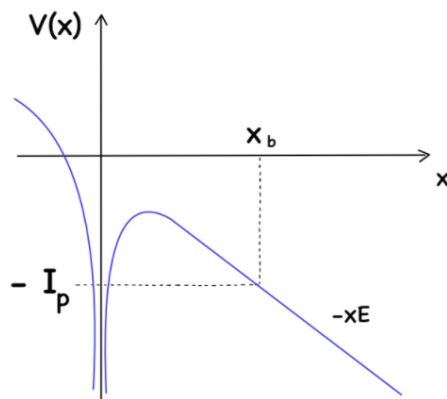


Figure 3.3. Distorted coulombian potential. At a fixed time, the electron can tunnel the barrier, which thickness is  $x_b$ .

Once realized tunnel ionization is the necessary starting point for HHG, one should look for an adequate procedure to determine the ionization rate. The first complete work in this sense is contained in the 1965 paper by Perelomov, Popov and Terent'ev [83], which takes into account both multiphoton and tunnel ionization. The more used model is the one proposed by Ammosov, Delone and Krainov [84] (known as ADK), which is simpler because it only considers tunnel ionization, and indeed coincide with the older one when  $\gamma \ll 1$ . More recently, Tong et al. extend this model to diatomic molecules [85].

ADK model still consider the atom-response, and in particular only one electron of the atom, while the others enter in the theory just in term of a screening potential, and then are taken into account the effective principal and orbital quantum numbers, defined as  $n^* = Z\sqrt{\frac{I_{pH}}{I_p}}$  (being  $I_{pH}$  the ionization potential of hydrogen) and  $l^* = n^* - 1$ . They assumed ionization occurred in a fraction of period of the laser field around a peak, so that  $E(t)$  can be regarded as quasi-static. The rate of ionization can be written as [74]:

$$\omega_{ADK} = |C_{n^*l^*}|^2 G_{lm} I_P \left(\frac{2F_0}{E}\right)^{2n^* - |m| - 1} \exp\left(\frac{-2F_0}{3E}\right) \quad (3.4)$$

Where  $C_{n^*l^*}$  and  $G_{lm}$  are coefficients depending on the subscripts. Without entering in too details, equation (3.4) discloses an exponential dependence on the driving electric field (being  $F_0 = (2I_p)^{3/2}$ ) and, most importantly, on a factor elevated to  $2n^* - |m| - 1$ , meaning that an electron with  $m = 0$  in the outer shell will undergo tunnel ionization most likely than one with a different magnetic quantum number.

### 3.2.2 Motion in the Electric Field

After the electron is tunneled into the continuum, it is free to move under the laser field  $\mathbf{E}(t) = \mathbf{E}_0 \cos(\omega_0 t) \mathbf{u}_x$ , according to Newton's Second Law:

$$\frac{d^2x}{dt^2} = \frac{eE_0}{n} \cos(\omega_0 t). \quad (3.5)$$

Integrating and assuming that electron starts its motion with  $v(t_0) = x(t_0) = 0$  are obtained expression for velocity and position along  $x$ :

$$v(t) = \frac{eE_0}{m\omega_0} [\sin(\omega_0 t) \cos(\omega_0 t_0)], \quad (3.6)$$

$$x(t) = -\frac{eE_0}{m\omega_0^2} [\cos(\omega_0 t) - \cos(\omega_0 t_0)] + \frac{eE_0}{m\omega_0} \sin(\omega_0 t)(t - t_0). \quad (3.7)$$

This completely classical derivation ends in a family of trajectories the electron can follow depending on the initial phase  $\phi = \omega_0 t_0$ , where  $t_0$  is the ionization time. The electron trajectories are shown in fig. 3.4 as a function of the phase for different times  $t_0$ . Every time a trajectory intercepts the  $x = 0$  axis there is a collision. The same information is represented in the  $v - x$  plane: one can see that some trajectory leads the electron back to the parent ion, while others push it far away. If the electron recollides with the ion, it can have a null or a different from zero velocity. Interestingly, if the electron is emitted exactly at the peak of the electric field returns with zero velocity, thus null kinetic energy (black trajectory in 3.4 left side, d trajectory right side).

It can be shown recombination happens for  $0 < \phi < 80$  and  $180 < \phi < 260$ , i.e. just after the positive and the negative peak of the electric field so an impulse is generated every half optical cycle. This is the reason why only odd harmonic normally appears in a HHG spectrum: if one considers the simple interference between two pulses

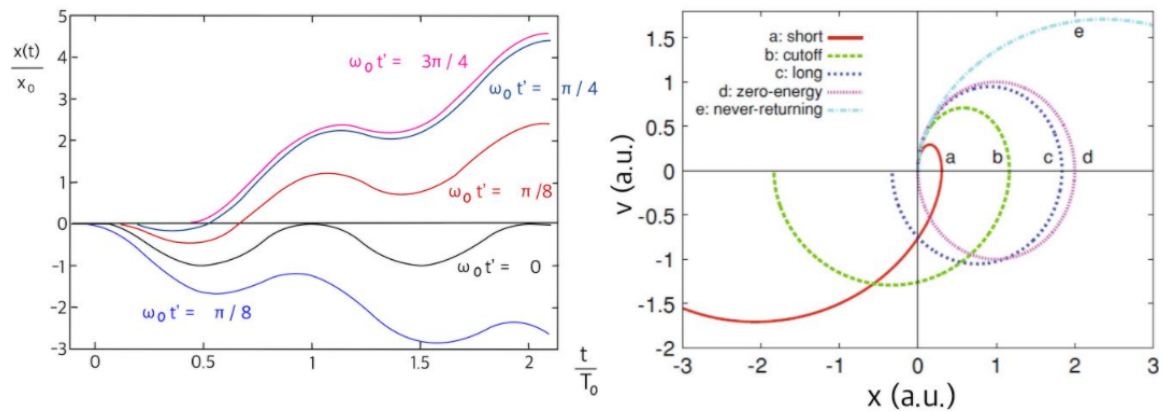


Figure 3.4. Trajectories for different initial phases, as a function of time (on the left) [74] and in the state space (on the right) [81].

generated within the period  $T$ ,  $\mathbf{E}'(t) = \mathbf{E}_1(t) - \mathbf{E}_1(t - \frac{T}{2})$ , one find a field amplitude modulated by a sinusoid of frequency  $\omega' = \omega_0(2n + 1)$ .

To calculate the final kinetic energy  $E_k = \frac{1}{2}mv(t_r)^2$ , which will be then associated to the energy of the emitted harmonic, one can solve (3.7) for  $x = 0$  and compute the returning time. Unfortunately, there is no exact solution for this problem, but it can be easily handled numerically. The highest kinetic energy is phenomenologically found to be  $3.17U_p$ , corresponding to  $\phi = 17^\circ$  (cut-off trajectory b in fig. 3.4).

Another significant result of this analysis is that there are two kind of trajectories leading to the same collision kinetic energy which are usually addressed as ‘short’ and ‘long’, as is evident considering figure 3.5. This is unwanted: long trajectory are characterized by  $\frac{dE_k}{dt} > 0$ , which means a positive variation of the harmonic frequency with time (known as frequency chirp), while short by a negative one. This kind of temporal distortions must be compensated to have a cleaner final pulse, but it is impossible to implement a compensation technique if the pulses have both positive and negative chirp [74]. More in general, it was recently understood that these different possible paths are a source of chromatic aberrations [86].

### 3.2.3 Recombination

When the electron recombines with its parent ion, there is the emission of a photon with an energy equal to the sum of the ionization potential and the final kinetic energy:

$$\hbar\omega = I_p + E_k \quad (3.8)$$

As underlined before, there is a maximum for the possible  $E_k$  and then, being  $I_p$  fixed, also for the photon energy, predicting the order of the cut-off of fig. 3.1:

$$N = \frac{I_p + 3.17U_p}{\hbar\omega_0} \quad (3.9)$$

Since  $U_p \propto \frac{E_0^2}{\omega_0^2} = E_0^2 \lambda_0^2$ , with  $\lambda_0$  the laser wavelength, it is possible to understand that the cut-off scales both with the ionization potential, then He is often choose as

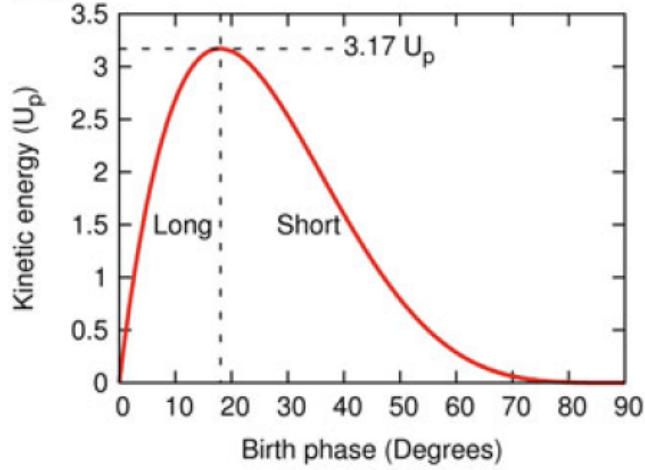


Figure 3.5. Kinetic energy is a non monotonic function of the initial phase, implying two different type of trajectories, which are called 'long' and 'short'. A mirrored graph could be considered for  $180 < \phi < 260$  [81].

the generating gas despite its low susceptibility, and with a dependence on the laser wavelength, as shown in fig. 3.6. Even if the formula suggest an indefinite increase of the photon energy with the laser intensity, there is a saturation level,  $I_{\text{sat}}$ , for which (3.9) no longer holds, corresponding to the complete depletion of the ground-state population, which need to stay in the atom to interact with the returning electron.

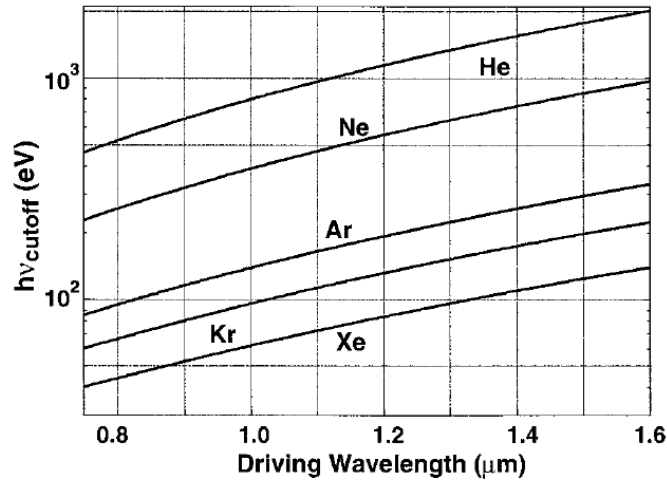


Figure 3.6. Cutoff energies as a function of the laser wavelength for different noble gases[87].

Equation (3.9) is confirmed by experimental data and validates the three-step model, which at a first sight might seem oversimplified but is able to predict the cutoff, to explain why only odd harmonics are produced and to give a hint of possible explanation of certain spatial and temporal characteristics of the harmonic pulses. Moreover, it suggest that the harmonic generation can be controlled by shaping appropriately electron trajectories through a tailored electromagnetic field.

Actually, the importance of this model goes beyond HHG, which indeed is not the only nonlinear process which could take place in these strong-field conditions: others are hot above-threshold ionization and correlated two-photon ejection [77]. They can be understood as the elastic and inelastic scattering of the returning electron with the parent ion, in the latter case ionizing the atom again and putting another electron in motion.

### 3.3 Quantum Models

#### 3.3.1 Quantum Treatment of Electrons' Dynamics

An important class of models try to introduce quantum perspective in the analysis of HHG considering the time dependent Schrodinger equation assuming the generated field as irradiated by electric dipoles:

$$\mathbf{P} = N \langle e\mathbf{r}(\mathbf{t}) \rangle = Ne \langle \psi(\mathbf{r}, t) | \mathbf{r} | \psi(\mathbf{r}, t) \rangle \quad (3.10)$$

which will be then included in a wave equation like (2.6) to compute the electric field. The problem is then reduced to find a  $\psi(t)$  which solve

$$i \frac{\partial |\psi(t)\rangle}{\partial t} = \hat{H} |\psi(t)\rangle \quad (3.11)$$

where, in the interaction picture,  $\hat{H}$  is the sum of the laser-free Hamiltonian (in atomic units)

$$\hat{H}_0 = -\frac{1}{2} \nabla^2 + V(r), \quad (3.12)$$

and the perturbation Hamiltonian in the dipole approximation

$$\hat{H}' = -\mathbf{r}\mathbf{E}(t). \quad (3.13)$$

Physically, this assumption is justified by the fact that the atom is usually much smaller than the driving laser wavelength, thus is possible to neglect the spatial dependence of the vector potential. As in three step model, it is considered that only one electron responds to the applied field (Single Active Electron approximation) and then we model the nuclear potential as  $V(\mathbf{r}) = \frac{Z}{r}$ .

Finally, it is assumed that the electrons are promoted directly from the ground states in the continuum (Strong Field Approximation) and there they do not feel anymore the coulombian field.

Then,  $|0\rangle$  (the fundamental state) and the continuous states  $\{k\}$  (fig. 3.7) form a complete basis set for the atomic system, which total wave function is

$$|\psi(t)\rangle = e^{iI_p t} [a(t) |0\rangle + \int d^3\mathbf{k} b(\mathbf{k}, t) |k\rangle] \quad (3.14)$$

where  $b$  are coefficients weighing the  $\{k\}$  states.

Inserting (3.14) in (3.10), we obtain an equation which can be solved with numerical non-trivial approximation to eventually obtain the dipole moment of the atom. One

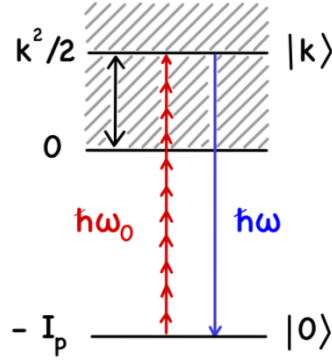


Figure 3.7. Quantum levels involved in the harmonic generation under the strong field approximation. Only the ground state  $|0\rangle$  and a level  $|k\rangle$  from the continuum, which energy is  $\frac{k^2}{2}$ , are considered, while any other possible resonance is neglected.

of the results obtained by Lewenstein [79], which was the first to propose this kind of approach, is a correction of the cut-off law

$$E_{cut} = I_p F \left( \frac{I_p}{U_p} \right) + 3.17 U_p \quad (3.15)$$

being  $F \left( \frac{I_p}{U_p} \right)$  equal to 1.3 for  $I_p \ll U_p$  and tending to 1 as  $I_p$  grows. This analysis allows to obtain some expressions for the generation efficiency and was extensively used to enhance the output of HHG.

### 3.3.2 Quantum-Optical Formulation

A most complete quantum treatment must include the quantization of the electromagnetic field, entering the realm of quantum optics. In principle, such a model can reveal new aspects of HHG: for example, the calculation of photon statistic shows that in each harmonic light can be in squeezed or bunched states [80]. To the present day, no experiment has been performed to study these peculiarities.

Still, this model starts from the Schrodinger equation. This time  $|\psi(t)\rangle$  is not only the electronic wave function, but also contains the laser field which can be expressed by a multimode coherent state

$$|\psi_{laser}\rangle = \prod_{\mathbf{k}_l j} |\alpha_{\mathbf{k}_l j}\rangle e^{-i\omega_k t}, \quad (3.16)$$

where  $\mathbf{k}_l$  is the laser wavevector and  $j$  the polarization. The Hamiltonian is then

$$\hat{H} = \frac{1}{2m} (\mathbf{p} - q\mathbf{A}_c(t))^2 + U + \hat{H}_F \quad (3.17)$$

Where  $\hat{H}_F$  is the Hamiltonian of the free electromagnetic field and the vector potential  $\mathbf{A}$  contains both the laser and the emitted field.

This theory will be not further developed here, but opens the door to a unified treatment of any frequency conversion nonlinear optical process.

### 3.4 HHG Improvement Strategies

Thus far, the microscopic physics of HHG has been exploited to clarify the origin of this kind of radiation and to justify the peculiarities of the spectrum. However, the interest in this phenomenon is not just theoretical, but very practical indeed: HHG could be used as an ultrafast, coherent source of EUV and SXR pulses for countless applications. But the transition from the microscopic world to the macroscopic application is never so smooth, and the generation of intense and bright attosecond pulses via HHG is still challenging.

One could think that since every atom emits harmonics over a broad range of energies (up to  $keV$ ) then also the HHG spectrum should show high energy photons. This is not automatically true, because it is needed that the photon generated by many atoms coherently add to provide the output beam, as shown in fig. 3.8. This is a well-known issue in nonlinear optics that is usually overcome by equalizing the phase velocity of the pump light with the generate beams by using birefringence [88], satisfying the so-called phase-matching condition which is commonly exploited in frequency conversion experiments. Unfortunately, in HHG several macroscopic mechanisms make hard to reach phase matching and different expedients have been proposed during the years to improve the coherence of the output beam. Another critical point to be addresses is the experimental apparatus used for generation and in particular the solutions to confine the gas. In this sense, hollow waveguides system proved themselves as a worthwhile choice.

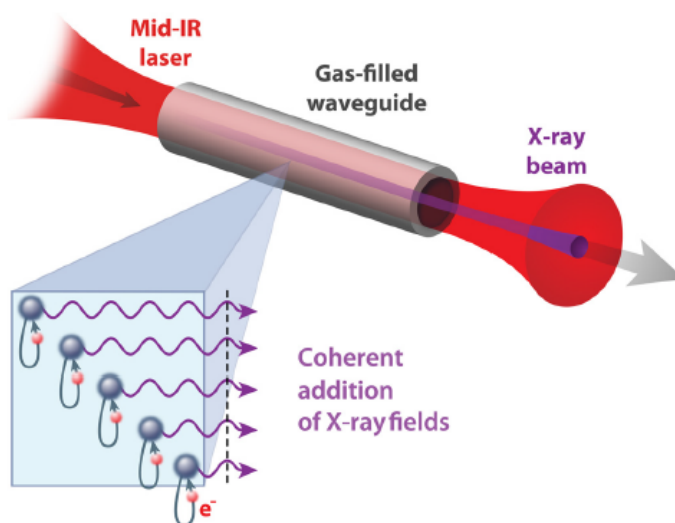


Figure 3.8. Representation of an extreme nonlinear upconversion of a femtosecond laser in a gas-filled hollow channel. To be successful, phase matched addition of harmonic produced by each single atom is required [89].

#### 3.4.1 Phase Matching

Until the photon energies of the driving laser are kept low, more or less  $< 130 eV$ , HHG can be easily phase matched over centimetre lengths by balancing the neutral atom

dispersion with the dispersion of the free-electron plasma [89]. This is possible up to some critical ionization level that depends on the gas species and laser wavelength [90], for which the matter becomes strongly ionized and dispersive inducing relative phase slip between the laser and the harmonic field. To quantitatively address the phase matching problem, two important quantities can be defined. One is the absorption length:

$$L_{abs} = \frac{1}{\sigma\rho} \quad (3.18)$$

where  $\sigma$  is the ionization cross section and  $\rho$  the atomic density, the other is the coherence length

$$L_{coh} = \frac{\pi}{\Delta k} \quad (3.19)$$

which is the length over which the harmonics field build up constructively, being  $\Delta k$  the wave vector mismatch [91].  $\Delta k$  can be calculated as a sum of contributions due to neutral gas dispersion, plasma dispersion and, if it is the case, waveguide dispersion. To have a good matching should be  $L_{coh} > L_{abs}$ : an optimal conversion efficiency in a long uniform medium is obtained for  $L_{coh} > 5L_{abs}$  [92]. Even when  $L_{coh}$  can be considered infinite, HHG emission saturates as the medium length is few  $L_{abs}$ , as depicted in fig. 3.9. To reach this condition, the wave front of the laser field should be slow varying, as it is the case in a hollow waveguide.

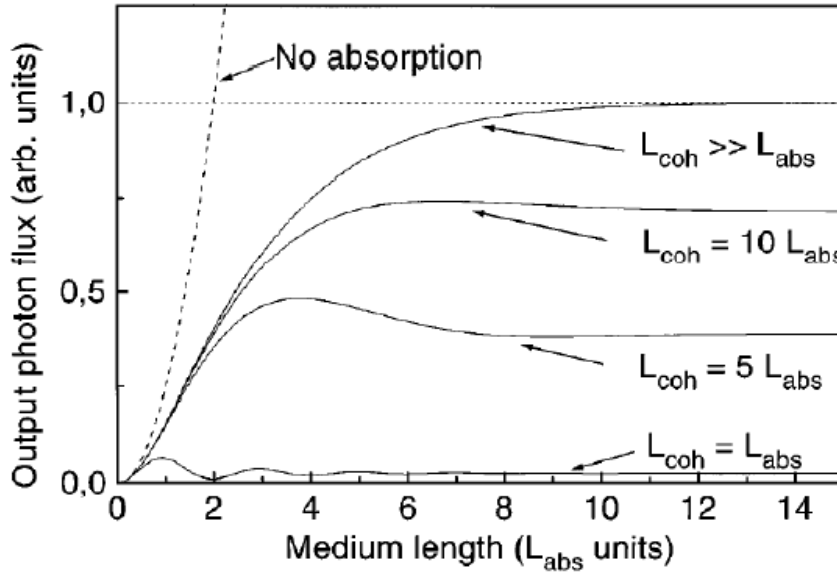


Figure 3.9. On axis photon flux as a function of the medium length [92].

To obtain higher-order harmonics can be employed quasi-phase-matching techniques, consisting in the compensation of the phase mismatch readjusting every  $L_{coh}$  the relative phase or cancelling the out-of-phase emission. The idea is that in high nonlinear optics even a little phase change can have dramatic consequences on the output. Practically this is generally achieved by modulating the atomic density, or the fundamental laser beam along the laser axis, for example varying the gas pressure [91],

but other schemes have been proposed, such as the use of two counter-propagating driving beams [93].

### 3.4.2 Gas-Filled Hollow Waveguide

First studies on HHG were performed on gas-jet systems, with laser beams tightly focused on a stream of noble gas atoms. Such a configuration had a very low efficiency (about  $10^{-7}$ , meaning one harmonic photon generated every ten million photons of the driver [94]) depending on the properties of the laser field and strongly influenced by the dispersion in a nonlinear material but also by the focusing of the laser [95], the latter being a purely geometrical effect which leads to destructive phase cancellations [96]. Great improvement in the harmonic generation efficiency (up to, in the best conditions,  $10^{-4}$ ) has been achieved by gas-filled hollow waveguide systems.

The key reason why hollow guides represent a good alternative is that they can provide a sharp transverse intensity profile of the fundamental beam and thus a very controlled geometry of the interaction region. Obviously, also waveguides have losses, depending on the wavelength and related to geometrical factors and, as will be extensively shown in chapter 6, to the internal surface quality.

Wave propagation along a hollow channel can be regarded as multiple reflection at the inner walls, occurring at a grazing incidence. Since the losses affect mostly high-order modes, only the fundamental propagates adequately through the guide, as shown in fig 3.10. Thus, it is possible to choose cylindrical channels with internal radius  $a$  much larger than the free-space wavelength [97].

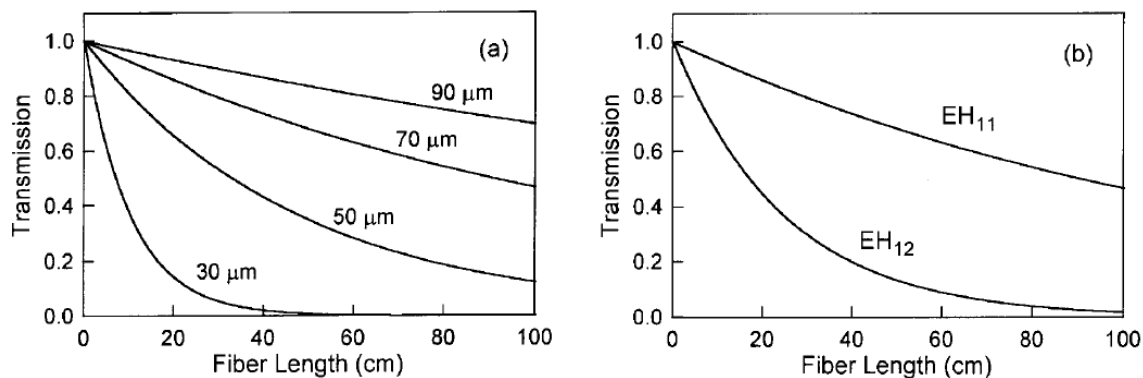


Figure 3.10. (a) Transmission of the fundamental mode  $\text{EH}_{11}$  at 780 nm as a function of hollow fiber length for various radii of the guide and (b) against the next high-order mode  $\text{EH}_{12}$  for a 70  $\mu\text{m}$  diameter fiber [96]. Higher length of the channel helps in the discrimination of the fundamental mode.  $\text{EH}_{11}$  hybrid mode is the lowest order mode for fused silica hollow waveguides.

A complete analysis of the field configurations and propagation constants of the normal modes in a hollow circular waveguide was performed by Marcatili and Schmeltzer [97]. It is based on the following assumption:

- Radius  $a$  much larger than the free space wavelength  $\lambda$ :

$$ka = \frac{2\pi a}{\lambda} \gg |\nu| u_{nm}. \quad (3.20)$$

- Infinite wall thickness.
- Magnetic permeability equal to that of free space  $\mu_0$ .
- Only low-losses modes considered, which are those whose propagation constant  $\gamma$  are nearly equal to that of free space:

$$\left| \frac{\gamma}{k} - 1 \right| \ll 1. \quad (3.21)$$

Here,  $k$  is the free space propagation constant,  $u_{nm}$  is the  $m$ th root of the equation  $J_{n-1}(u_{nm}) = 0$  for the Bessel function of order  $n - 1$  and  $\nu = \sqrt{\frac{\epsilon}{\epsilon_0}}$  is the complex refractive index of the external medium. The integers  $n$  and  $m$  are thus two labels identifying the propagating mode. All the modes form a complete set over a cylindrical system of coordinates  $(\theta, r, z)$ . In [97] are shown the mathematical expressions for each mode and their field lines (the first modes are shown in fig. 6.4), by which they can be qualitatively divided in three groups:

- Transverse circular electric modes  $TE_{0m}$ : the field lines are concentric circle in the cross section centred on the axis of the guide. The field component are  $E_\theta$ ,  $H_R$ ,  $H_z$ .
- Transverse circular magnetic modes  $TM_{0m}$ : the field lines are directed radially. The field component are  $H_\theta$ ,  $E_R$ ,  $E_z$ .
- Hybrid mode  $EH_{nm}$  ( $|n| \geq 1$ ): both components are present. All the field components are present, but the axial ones are relatively small and are usually neglected.

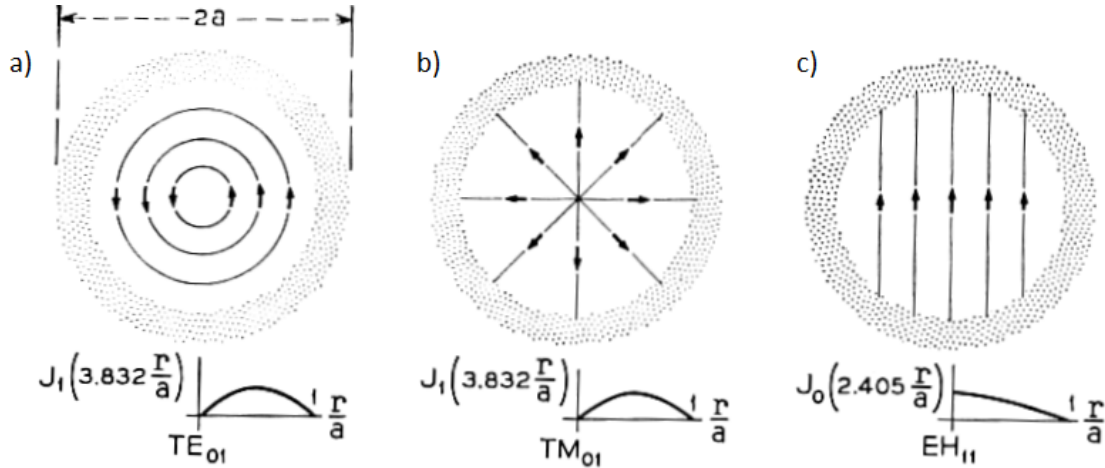


Figure 3.11. Examples of (a) a transverse circular electric, (b) a transverse circular magnetic and (c) an hybrid modes [97].  $TE_{01}$  is the fundamental mode for waveguide in which the external medium has a refractive index 2.02 times greater than the internal medium, in other cases is  $EH_{11}$ .

$|n|$  and  $m$  are parameters which respectively represent the number of periods in the  $\theta$  direction and the number of maxima and minima in the radial direction. TE and TM modes have  $n = 0$  as the result of the assumption  $a \gg \lambda$ .



# Chapter 4

## Materials and Methods

The major experimental equipment employed in this work is illustrated in this chapter. Each section is devoted to a specific stride of the activity, namely FLICE, hollow waveguide characterization and HHG.

### 4.1 FLICE Fabrication Setup

#### Laser Source

Laser light for femtosecond laser micromachining is provided by Satsuma HP2 (Amplitude Systemes S.A), an air-cooled commercial femtosecond laser system. It includes a diode-pumped ultrafast fiber amplifier and an electro-optic pulse picker which allows to deliver pulses at a repetition rate from 1 *MHz* to 40 *MHz*. The pulse duration can be tuned from 230 *fs* to over 10 *ps*. Its central wavelength is  $1030 \pm 5$  *nm*, and its specification reports a beam quality  $M^2 < 1.2$  and a beam circularity  $> 87$  %.

At 1 *MHz*, the beam power is of the order of 10 *W* and can be tuned by an internal attenuator. The laser is vertical polarized with respect to the optical table. To operate properly, it needs some control on the environmental condition, that is a room temperature of  $22 \pm 1$  °C and humidity around 40 %.

All the laser parameters are monitored by an external software.

#### Beam Steering

Laser beam undergoes several manipulations which aims to the extraction of the second harmonic at 515 *nm* with the proper power to promote non-linear absorption. The optical path is shown in fig. 4.1.

Two mirrors deflect the beam towards two lenses, L1 and L2, which form a telescope needed to shape the beam cross section before it enters the following stage, consisting in a half-wave plate and a polarizer put in cascade. The first is mounted on a gear-driven rotary stage and is used to change the polarization and in turn, thanks to the polarizer, the attenuation of the beam. It eventually arrives at the sample with a power included between 300 and 400 *mW* which can be tuned controlling remotely the half-wave plate rotation with A3200 software.

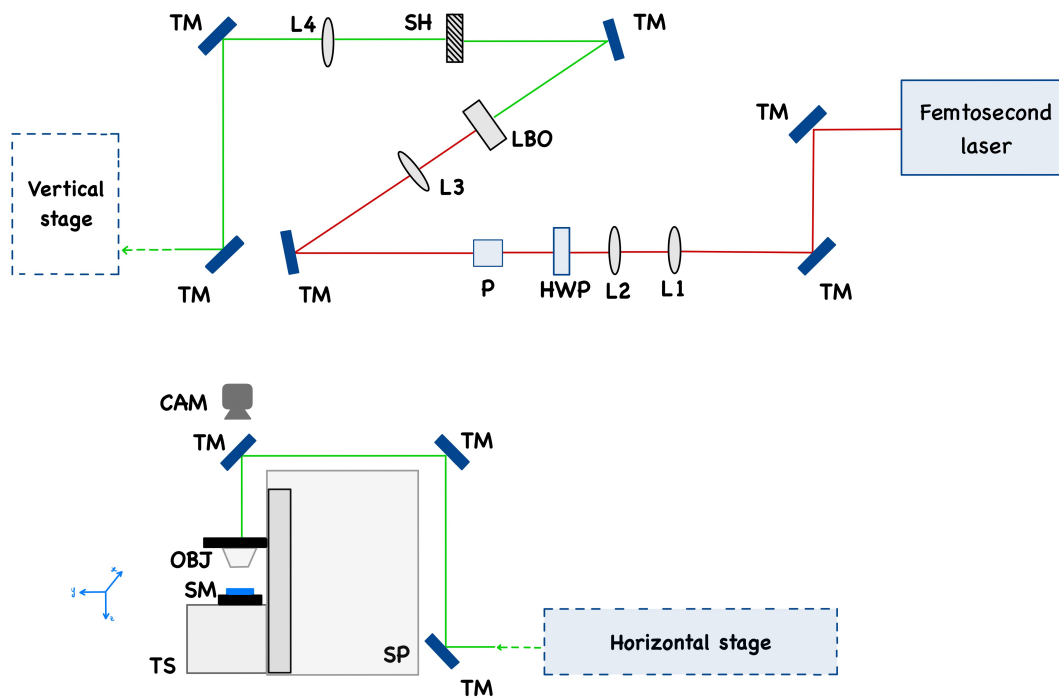


Figure 4.1. Schematic experimental apparatus for femtosecond laser writing, a) top and b) side view. The red line represent the IR line, at  $1030\text{ nm}$ : TM - turning mirror; L1 -  $75\text{ mm}$  focal length lens; L2 -  $150\text{ mm}$  focal length lens; L3 -  $400\text{ mm}$  focal length lens; HWP -  $\lambda=2$  waveplate; P - polarizer; LBO - Lithium Triborate crystal. For the green line, at  $515\text{ nm}$ : TM - turning mirror; L4 -  $800\text{ mm}$  focal length lens; SH - mechanical shutter; CAM - imaging camera; OBJ - focusing objective; SM - glass sample; TS - translation stages; SP - mechanical support.

Before every fabrication a calibration of the rotary stage is needed since the delivered power can slightly change because of environmental factors. To do it, power is measured thanks to a power meter near the position of the objective, with an uncertainty of few  $mW$ , and each desired power is associated to a particular position of the half-wave plate which enters as an input in the controlling software.

Next, a mirror sends the beam to the second harmonic generation stage (SHG). These first three mirrors operate in the wavelength region of 1000-1060  $nm$ , the following in the 500-530  $nm$  range.

Lens L3 adapt the beam cross section to the dimensions of a Lithium Triborate ( $LiB_3O_5$ ) or LBO crystal, which generates the second harmonic. After this stage polarization is parallel with respect to the optical plane as a consequence of phase matching, which requires the outgoing photon polarized perpendicular to the incoming two. To optimize SHG, LBO is kept in an oven maintaining an appropriate temperature, being it a birefringent crystal whose index of refraction is temperature depending.

Lens L4 forms a telescope with lens L3 to collimate and enlarge the beam to the dimension of the whole aperture of the focusing objective, a 63X Zeiss dry objective (LD-plan Neofluor) with 0.65 numerical aperture. It is equipped with a correction collar to compensate spherical aberration at a depth that is changed manually once during the fabrication. Finally, a mechanical Uniblitz shutter stops the propagation of the beam to allow discrete modification of the material. It is controlled by the same A3200 software which adjusts the half wave plate and move the translational stage.

## Translational Stage

To obtain a precise three-dimensional structure a fundamental role is played by the mechanisms which move the sample with respect to the objective, in this case a 1D and a 2D Aerotech stages (ANT130-035-L-ZS-PLUS and ANT95-50-XY-CMS-ULTRA). Referring to the reference system in fig. 4.1 (b), the first stage guarantees the motion of the objective along z axis, whereas the second moves the sample in the xy plane. Due the foretold polarization of the laser beam, x direction is the preferential writing direction, along which the generated nanogratings are aligned (cfr. Chapter 1). The maximum declared stroke in both x and y direction is of 50 mm, but in practice it was possible to fabricate over a distance of 49 mm. This represents a constraint in the design of the Differential Pumping Chip (cfr. Chapter 5).

The levelling of the sample in the plane is done manually by looking at the back-reflected spot size while spanning over the whole sample and tilting it with precision control knobs. A CMOS camera is devoted to this purpose.

The desired movement of the stages is dictated by a sequence of G-CODE instructions. They are written both directly in G-CODE language and through a customized MATLAB program, which can generate a code for a point-by-point translation of the stages, taking as input the desired geometry. Unfortunately, it is not possible to use the MATLAB tool to fabricate big structures because it generates too heavy programs the A3200 software is not able to run.

## Wet Chemical Etching

The second step of FLICE technique is the chemical etching, performed submerging the fused silica samples in an aqueous solution of hydrofluoric acid, which is diluted at 10 % starting from a 20 % molar solution. The solution with the sample is contained in plastic beakers, placed inside an ultrasonic bath at about 35 °C to enhance the effect of the acid. These steps must be performed under a fireproof fume hood since the dangerousness of HF and reaction products. Personal protective equipment, such as gloves and lab coats, is also necessary.

At the end of the etching process, which in this work could last some hours, the sample is washed with deionized water, again in ultrasonic bath, to remove residual chemicals and any possible scrap of glass trapped inside the channels. After drying with nitrogen, the sample can be handled with tweezers. The result of the procedure is then evaluated with an optical microscope or a scanning electron microscope.

## Thermal Annealing

Some of the samples used in this work underwent thermal treatment. For this process is used a L5/13 Nabertherm oven able to reach a maximum temperature of 1300 °C. Annealing cycles are imposed through a P330 controller and optimized by the user as a sequence of plateau and ramps. The sample is placed inside the furnace without any holder to avoid the risk of cracks in the outer surfaces, which however appears slightly ruined after the treatment. Since any impurities can be the starting point of a fracture, before the treatment the sample is left for some hours in chromic acid, a strong oxidant able to remove any insoluble organic residual. For the same reason, the oven should be cleaned before use.

## 4.2 Hollow Waveguide Characterization

The hollow waveguides used for HHG in this work were previously characterized in order to estimate the coupling losses and to acquire the intensity profile of the fundamental mode, to compare with theoretical prediction. For this purpose, a coupling set-up was mounted as shown in fig. 4.2.

A Toptica laser with a central frequency of 780 *nm* (near the one used for HHG) provides the light beam to be coupled with the wavelength. As in FLM, the beam power (which is of few *mW*) is adjusted with a rotating half-wave plate followed by a polarizer. A biconvex lens (L1) with a focal length of 20 *cm* reduces the cross section of the beam to 0.6453 times the radius of the waveguide, to enhance the energy coupling with the  $EH_{11}$  guided mode. To respect this exact focal length, the lens is mounted on a translational stage and slightly moved parallel to the beam. The coupling is performed manually by moving the sample, which is hold by a manipulation stage with a micrometric resolution that allows the translation horizontally and vertically with respect to the laser beam and the tilting in the same directions, thanks to the experience of the operator which can recognize the guided mode simply putting a cardboard after the sample. For coupling optimization and for the acquisition of the mode, the light is collected by a lens (L2) with  $NA = 0.55$  on a CCD Spiricon camera, which sends the image to an external software which can fit the intensity profile with

a Gaussian shape. However, the image data are exported, and a better fitting can be done with another program, as for example MATLAB.

Waveguide insertion losses are calculated by measuring the power before and after the sample and taking the ratio. For space reason, in this case the power meter was maintained in the same position after the sample and the measure was done with and without the waveguide.

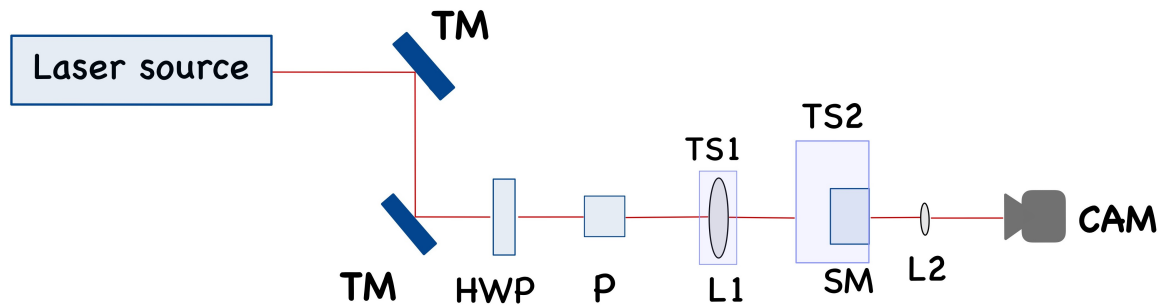


Figure 4.2. Schematic experimental apparatus for hollow waveguide characterization, with optical elements operating at 780 nm: TM - turning mirror; HWP - half-wave plate; P - polarizer; L1 - 20 cm focal length lens; TS1 - translation stage; SM - sample; TS2 - translation stage; L2 - aspheric 40x lens; CAM - collecting camera.

## 4.3 HHG Setup

In contrast with FLM, which do not require any particular adjustment of the surrounding conditions (besides temperature and humidity), HHG is performed in a high controlled experimental environment, mainly because extreme ultraviolet (EUV) and soft X radiation (SXR) are strongly absorbed by atmospheric gases. Then both the generation and the measurement of the harmonics requires vacuum chambers. When employed in the following described apparatus, the HHG chip can be used for several weeks without showing any quality degradation. From the schemes in fig. 4.3 and 4.5, we can recognize three main components of the experimental apparatus: the driving laser, the interaction chamber and the collecting stage.

### Laser Source

The beam, provided by a Ti:Sapphire laser with a preferential emission wavelength centered at 800 nm, is characterized by pulses 25 fs long, delivered with a repetition rate of 1 kHz, with an energy of 1 mJ each. The beam cross section is promptly reduced by a factor three by means of a two-lens telescope to be adapted to the transmission line which, as shown in fig. 4.3, starts with turning mirrors which direct the beam towards the first vacuum chamber. Some irises are devoted to a precise control of the power since it affects critically the harmonic generation process.

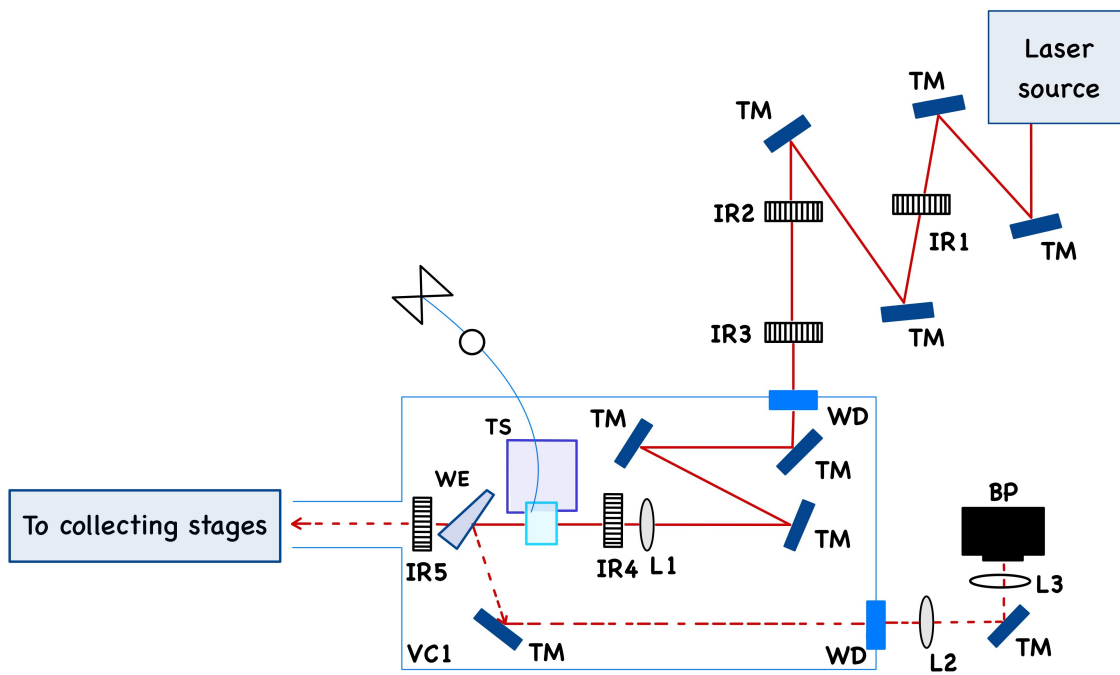


Figure 4.3. Schematic representation of the interaction chamber for high-order harmonic generation, with optical elements operating at  $800\text{ nm}$ : TM - turning mirror; IR1, IR2, IR3, IR4, IR5 - irises; WD fused silica window; L1 -  $200\text{ mm}$  focal length lens; SM - sample; TS - translation stages; WE - wedge; VC1 - first vacuum chamber; L2 - negative  $100\text{ mm}$  focal length lens; L3 -  $200\text{ mm}$  focal length lens; BP - beam profiler.

## Interaction Chamber

A scheme of the generation stage is proposed in fig. 4.3. The beam enters the vacuum chamber (characterized by a pressure around  $10^{-5} - 10^{-4}$  bar) through a fused silica window. After three turning mirrors, operating at  $800\text{ nm}$ , the beam is focused at the entrance of the hollow waveguide by a biconvex lens with a focal length of  $20\text{ cm}$ . The HHG chip is placed on the support shown in fig. 4.4. The beam enters on a tapered region, specifically designed to ease the coupling reducing the unwanted scattering, while exits through a straight profile. Lateral faces are shaped as well for reducing the distance between the chip and the objective during imaging experiments. The chip is clamped by a viton O-ring hosted in the top PMMA cover (see fig. 4.4 (b)). The transparent cover allows the operators to visually check the beam coupling.

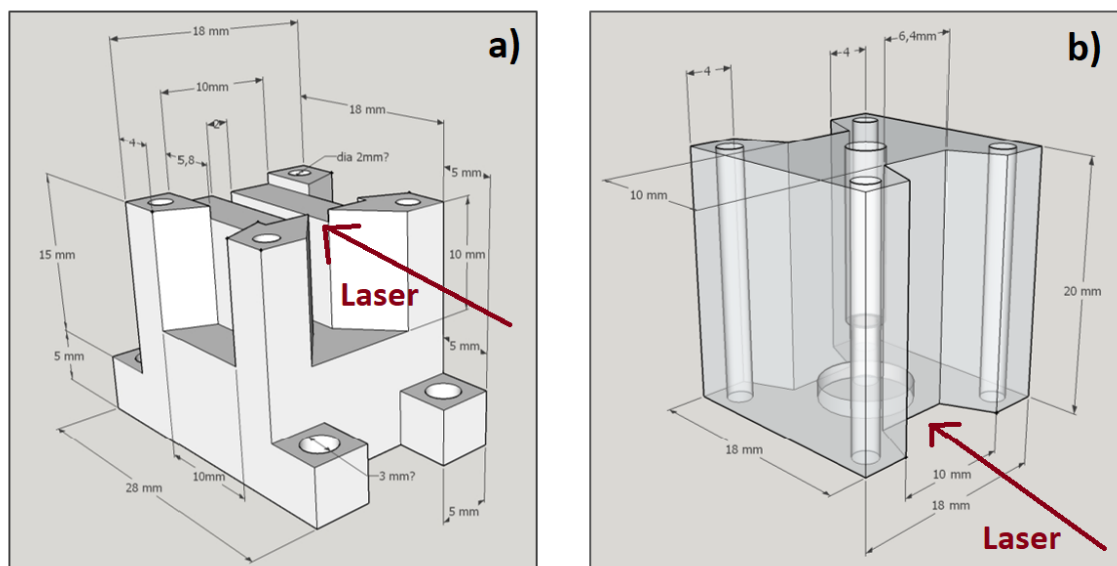


Figure 4.4. Three-dimensional drawings of a) aluminium base b) PMMA cover of the home-made support for the HHG chip.

The gas enters through a metallic tube and goes out sideways from the openings of the guide. Its pressure is carefully controlled thanks to a needle valve followed by a pressure gauge. The support is mounted on a high precision motorized alignment stage with two tilts and three axial micrometric knobs. A first coupling is done before the chamber is closed, then a finer positioning is done remotely after the chamber depressurization, since some distortion can be introduced while vacuum is made. The spatial quality of the beam is checked on a screen after the IR5 before the chamber is closed.

In order to inspect the coupling after depressurization, it is possible to insert via software a wedge which deviates the beam outside the chamber to be collected by a beam profiler. The operator can then look directly at the generated harmonics and optimize the coupling maximizing their intensity.

## Collecting stage

Collecting stage (fig. 4.5) consists by three chambers forming a spectrometer composed of grazing-incidence optics. In the first chamber a toroidal mirror is able to generate an intermediary focus employed in spectroscopy experiments. The following chamber contains a gold-coated toroidal mirror which purpose is to focus the HHG beam on a dispersion grating, located in the last chamber. The toroidal mirror, which position is accurately controlled remotely, can compensate the residual aberration through the adjustment of the sagittal focus and its tangential curvature.

The plus of this configuration maintaining always grazing incidences is that the detector collects a flat field signal, at almost normal incidence and at a fixed position. In the last chamber, the pressure is kept around  $10^{-7}$  bar to minimize possible noises. The grating is fixed to its position and ensure the detection of the harmonics from the order  $25^{th}$  to the  $161^{st}$ . The dispersed harmonics - which intensity is very weak - impinge a vacuum compatible detector, consisting of single stage microchannel plate and a phosphorous screen. The HHG photons ionize electrons from magnesium fluoride photocathode which are in turn multiplied along the microchannel plate. The gain is controlled by the bias voltage and must be properly tuned to avoid the saturation of the detector. The multiplied electrons hit the phosphorous screen and are converted again in an optical signal, which is collected by a focusing objective and finally acquired by an Apogee Ascent A2150 CCD camera.

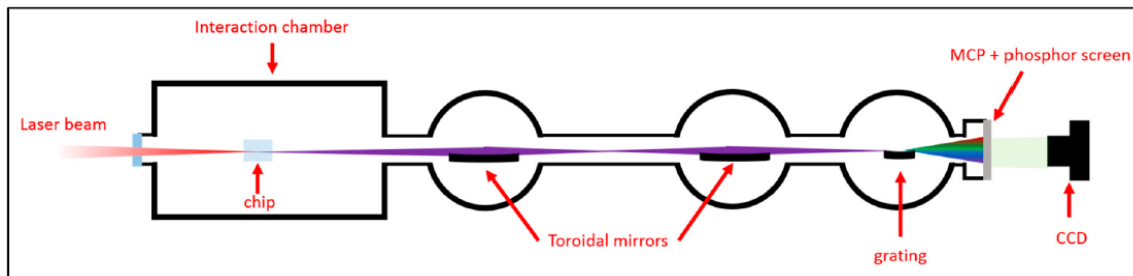


Figure 4.5. High-order harmonic generation and acquisition schematic setup [2].

# Chapter 5

## Differential Pumping Chip

### 5.1 Introduction

One of the main objectives of this thesis work was the design, fabrication and optimization of a new glass optical device able to replace the one used for the generation of sub-2-fs deep UV pulses presented in Chapter 2, integrating the bulky differential pumping described in sect. 2.3.1.

In several engineering and physical applications involving radiation, the need of separating vacuum chambers from the high pressure environment of the experimental apparatus is satisfied with windows made of thin metal, glass or polymer films. However, such an element unavoidably absorbs part of the radiation energy.

A windowless technique, known as differential pumping, is typically realized connecting with a thin orifice two chambers maintained at a very different pressures (typically, one of the two parts is connected to a vacuum pump). Often, there are more of this stages with different pumping speeds, and light is able to propagate through them thanks to the small apertures [98, 99]. This solution has been adopted both for separating vacuum chambers from the external environment and for isolating high pressure parts inside a vacuum chamber itself, as it is in the present case.

Due to the simplicity of the principle underlying this technique, it was considered possible to implement it inside the very same glass chip used for the generation of the DUV, exploiting all the capabilities of femtosecond laser micromachining. To the author knowledge, this is the first attempt to develop an integrated differential pumping system.

Besides all the advantages of integrated devices, as compactness, replicability and easy incorporation in different setups, it is believed that such a Differential Pumping Chip (DPC) will be able to increase the intensity of the generated third harmonic thanks to a better gas confinement. Moreover, it will be mounted on a high precision translation stage (while the present bulky system is fixed on its position), facilitating the alignment between the chip and the laser. This will assure the possibility for a forthcoming step of making the glass cell guiding to further increase the generation yield.

On the other side, the major difficulties in the realization of this device are related to

its dimensions. When switching from a 3 *mm*-length device as the one in fig. 2.5 to an almost 5 *cm* chip, the fabrication become a long and complex process which need to be carefully optimized in order to be successful.

Here are presented the main aspects related to design (Sect. 5.2) and fabrication (Sect. 5.3) of the DPC. In Appendix A is reported a detailed overview of the fluid dynamical simulation performed before the realization of the device, which outcome is also quickly shown in this chapter. It is believed that for the development of complex structured integrated devices, the numerical simulation of the gas flow will play an increasingly important role to have a preliminary feedback on the expected functioning.

In the present case, the simulations are consistent with the concept of differential pumping.

## 5.2 Design Criteria

A CAD drawing of the device is reported in fig. 5.1. It consists in a  $49 \times 15 \times 2$  *mm* fused silica slab glued on a glass substrate with the same area but a thickness of 1 *mm*. Two basic geometries can be distinguished: a central part, the *cell*, which is where the third harmonic is generated, and four *pumping chambers*, which are devoted to the differential pumping. All the chambers and the central cell are connected via a 800  $\mu\text{m}$ -diameter cylindrical *channel*, which runs through the chip for all its length.

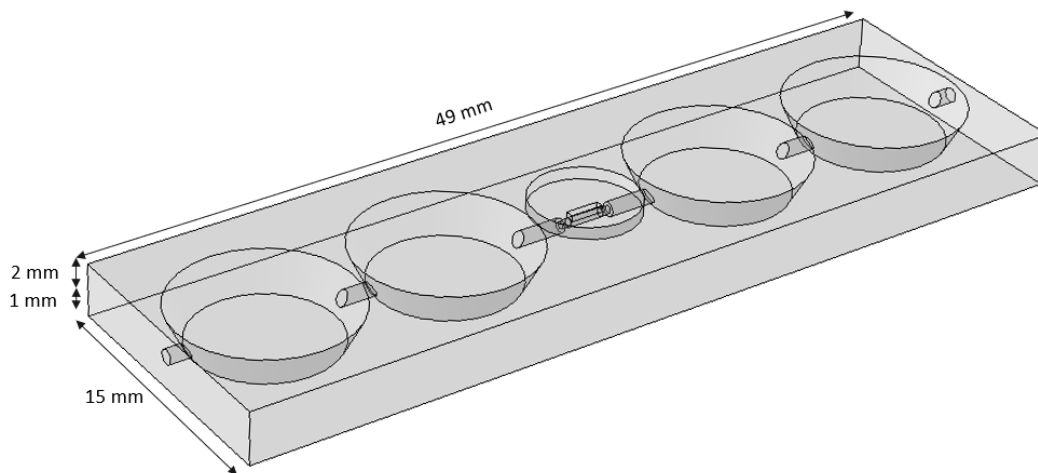


Figure 5.1. CAD drawing of the differential pumping chip. All the designs included in this work were realized with SolidWorks.

### Channel

To asses the dimensions of the channel, a first characterization of the laser beam was considered. It was focused by two different lenses with 50 *cm* and 80 *cm* focal length. The final focusing will be decided experimentally but 80 *cm* will be the upper limit, thus it defines the minimum size of connecting channels. Fig. 5.2 shows an

image of the laser beam on the focus. It is characterized by a  $\frac{1}{e^2}$  diameter of  $170 \mu m$  (averaged on  $x$  and  $y$ ) and a Rayleigh length ( $R_z$ ) of  $28.4 mm$ , with a diameter (at  $R_z$ ) of  $240 \mu m$ . In table 5.1 are also reported the laser parameters for a lens of  $50 mm$  focal length.

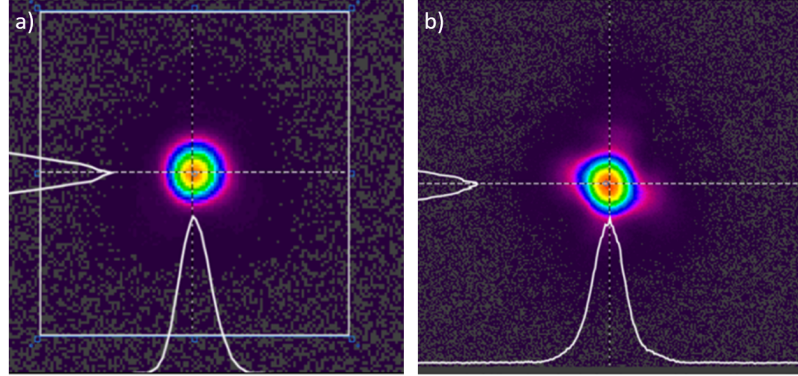


Figure 5.2. Beam cross sections for a) a focal length of  $50 cm$  and b) of  $80 cm$ . Measured parameter are reported in table 5.1.

Focal length ( $cm$ )	Spot size ( $\mu m$ )	$R_z$ ( $mm$ )	Diameter at $R_z$ ( $\mu m$ )	Retrieved collimated beam ( $mm$ )
50	86	7.3	122	5.9
80	170	28.4	240	4.8

Table 5.1. Measured parameters of the laser beam for two different focusing lenses.

The beam was also observed over a distance of  $\pm 30 mm$  from the focus, to take into account astigmatism effects which could enlarge and distort the beam cross section. The results are reported in fig. 5.3.

It is shown that the beam diameter never exceeded  $350 \mu m$ . However, it was decided to oversize the dimensions of the channel because this guarantees an easier alignment and a slightly better confinement of the gas in the cell without impacting too much on the irradiation-fabrication time.

The channel length is instead constrained by the maximum travel of the translational stage of the FLM setup (cfr. 4.1), otherwise it would have been preferred a longer device to provide more separation between the pumping stages (in the present design, the chambers are spaced by only  $0.5 mm$  in the top surface).

## Pumping Chambers

The pumping chambers are designed to be connected to two vacuum pumps with a flow of  $15 l/s$  each through small pipes with an internal diameter of  $8 mm$  and an external one of  $10 mm$ . The tapered shape ( $10 mm$  diameter on top reducing to  $8 mm$ ) is chosen to insert the pipes minimizing the irradiated area: the initial design foresaw a basis to accommodate them (similar to the one of the central part) but it

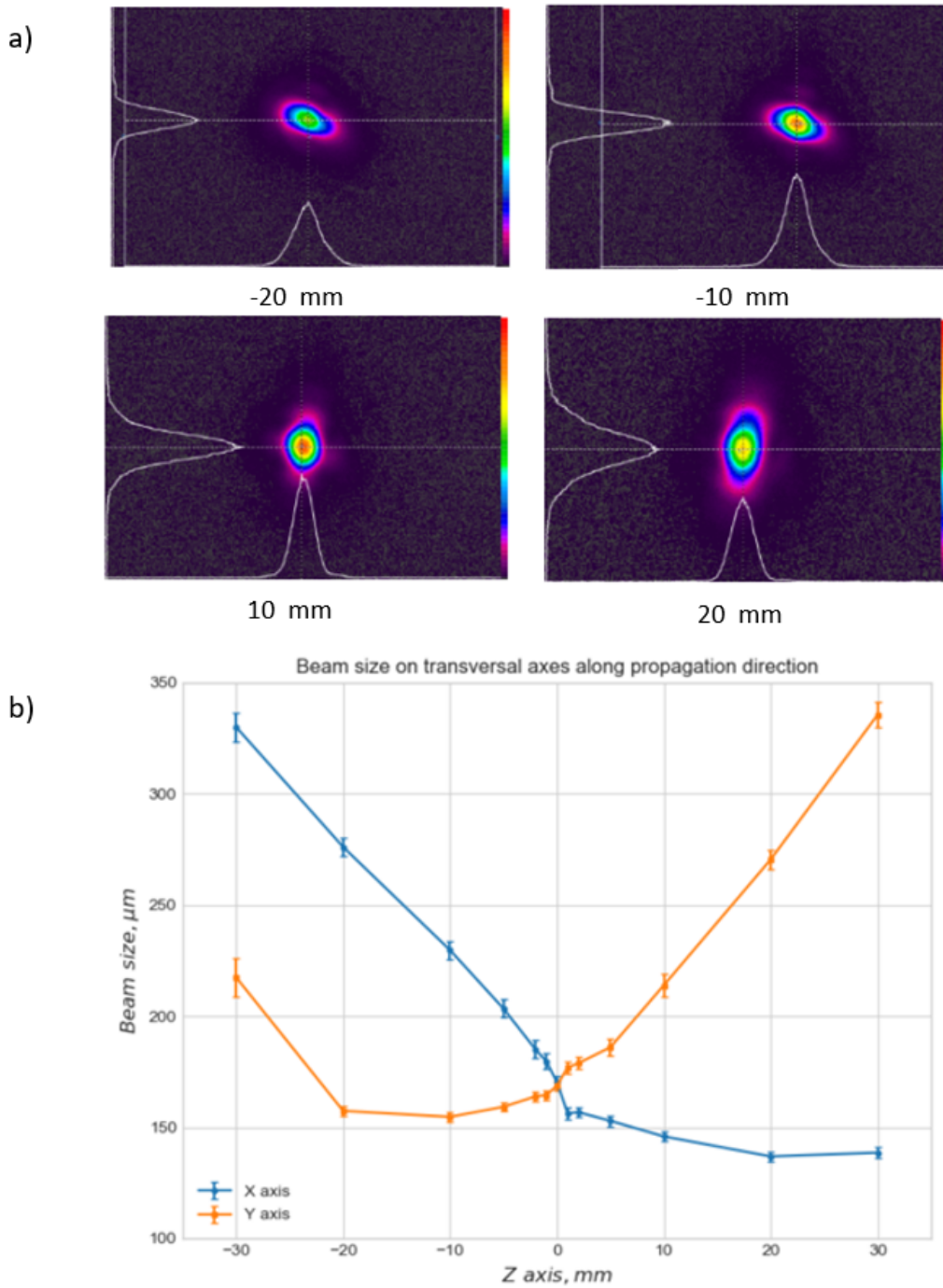


Figure 5.3. a) Beam spot at different position over the length of the DPC (the origin is set in the cell center). Effects of astigmatism are visible. b) Beam size on perpendicular axis along the propagation direction.

has been noted that removing it more than 10 hours of fabrication could be saved. For the same reason, the irradiation is done on a 2 mm thick sample and not directly on a 3 mm one: pass-through chamber can be fabricated quickly and the inner glass easily removed in the etching process.

## Cell

The most articulated structure of the device to be designed and produced is the central cell, shown in fig. 5.4. Its dimensions are analogous to the one previously used in [1], which proved itself really reliable operating for more than two years without showing any significant degradation. On top of it, a cylindrical reservoir is fabricated to house the inlet pipe and is connected to the cell with a box shaped channel. The cell is connected on both side to the bigger channel. The dimensions are reported in figure. The minimum diameter is of 400  $\mu\text{m}$ , much larger than the foreseen beam waist at that point.

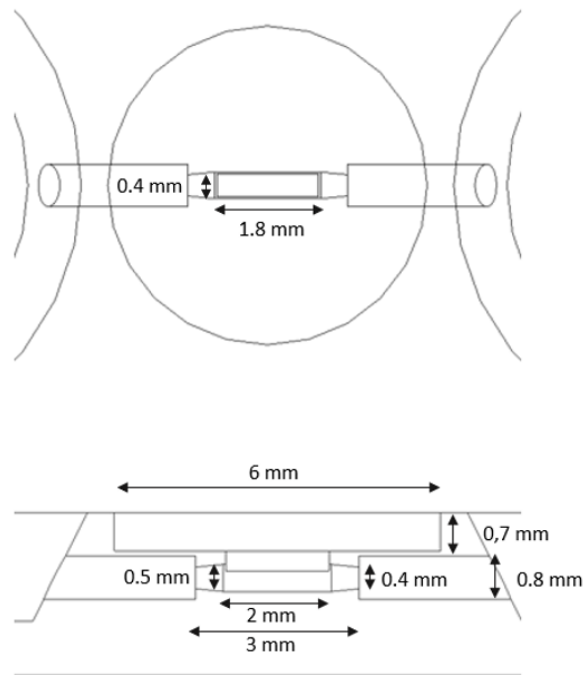


Figure 5.4. Top and front view of the glass cell for third harmonic generation.

### 5.2.1 Gas Flow Simulations

To predict the behaviour of the gas flow inside the chip, some numerical simulation were done according to the flow rates shown in fig. 5.5. Three vacuum pumps were considered, one for the vacuum chamber hosting the device and two directly connected to the top of the pumping chambers (one for each two). These pumps have a vacuum flow rate of 15 l/s. The flow in the pipes must be corrected by the resistance from the friction of the molecules with the walls, which in free molecular flow regime (cfr. A.1)

can be calculated as

$$\frac{1}{C} = \frac{l}{12d^3} \quad (5.1)$$

where  $C$  is the conductance (the reciprocal of the flow resistance, measured in  $l/s$ ),  $l$  and  $d$  respectively the length and the diameter of the pipe (in  $cm$ ). Then, being  $S$  the nominal pump speed, the flux out-going from the chambers  $S'$  can be estimated as:

$$\frac{1}{S'} = \frac{1}{C} + \frac{1}{S} = 0.6 l/s \quad (5.2)$$

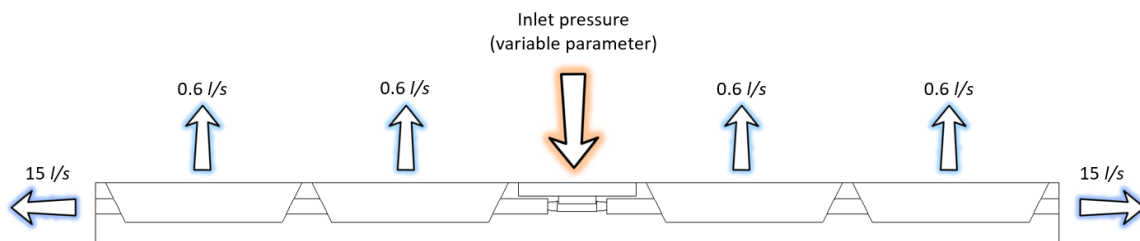


Figure 5.5. Gas flow through the DPC. Each pair of pumping chambers is connected to a vacuum pump which speed is  $15 l/s$ . This value is corrected to  $0.6 l/s$  to consider the piping conductance. The device is hosted in a vacuum chamber, so the gas flows out also from the two sides, realizing the differential pumping.

Of course, this is just an approximation of the real system, but it was deemed appropriate to include conductivity effects in these simulations.

In fig. 5.6 is shown the number density of the gas molecules for different inlet pressures as computed by the Free Molecular Flow module of COMSOL Multiphysics. The simulation shows a density of  $10^{26} particles/m^3$  which is reduced of four order of magnitude in less than  $25 mm$ . Such a gas density drop is enough to ensure a good gas pressure in the main chamber and a propagation with little absorption through the rest of the device.

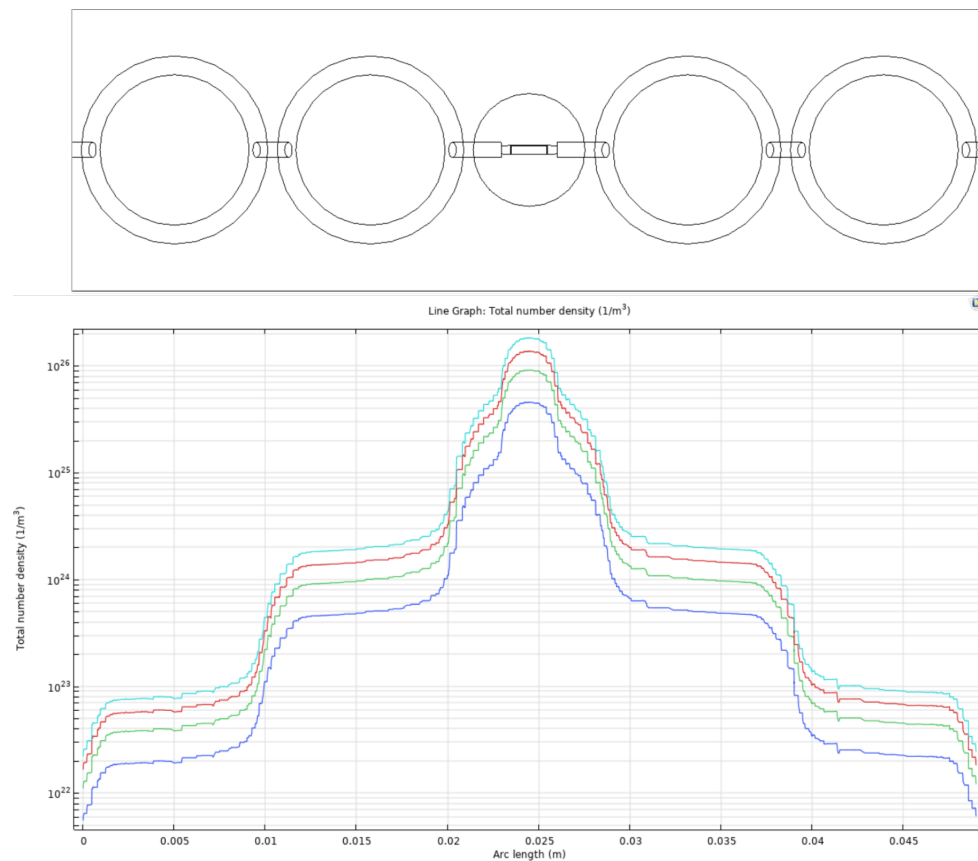


Figure 5.6. Top view and total number density (logarithmic scale) along the axis of the DPC for different inlet pressures: 2 atm (blue line), 4 atm (green line), 6 atm (red line), 8 atm (light-blue line). More simulations can be found in appendix A.

## 5.3 Fabrication

### 5.3.1 Etching Dynamic Analysis

Preliminarily to any micromachining on a new fused silica sample, it is necessary to investigate the etching dynamic by irradiating an array of lines both in  $x$  and  $y$  direction for different powers and relative velocities. The lines are then left in the etching solution for one hour, after which the length of the etched path is measured. The operation is repeated another time for the lines scanned in the  $x$  direction (fig. 5.7).

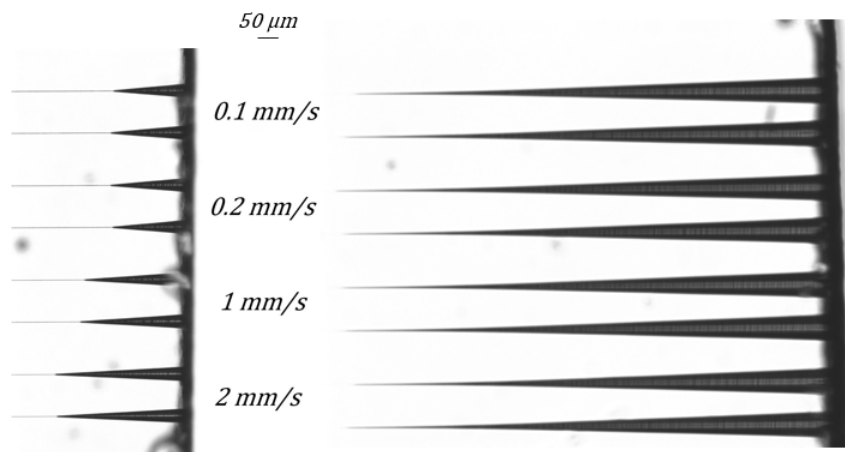


Figure 5.7. Optical images of the lines irradiates along  $y$  direction at  $380\text{ mW}$  for 1 h (on the left) and along  $x$  direction at  $350\text{ mW}$  for 2 hrs (on the right). The etching rate along  $y$  is much smaller than along  $x$ . It can be observed the characteristic conical shape of the etched region.

The results of this study are reported in tables 5.2, 5.3 and 5.4.

Writing velocities ( $mm/s$ )	Powers ( $mW$ )			
	300	350	380	400
<b>0.1</b>	1040	1030	1000	990
<b>0.2</b>	1040	1030	1000	1020
<b>1</b>	1040	1030	1040	1080
<b>2</b>	1040	1020	1040	1100
<b>4</b>	1030	1000	1020	1070
<b>10</b>	970	950	1000	1040
<b>20</b>	—	—	—	—

Table 5.2. Lengths (in  $\mu m$ ) of the etching paths over lines irradiated at different laser powers and writing speeds along the  $x$  direction (perpendicular to the laser polarization) after **1 h** in 20% HF solution. Lengths are given with an uncertainty of  $\pm 40\ \mu m$ .

The laser powers are the ones used in the fabrication and seven different velocities were tested. Several observation can be made: this setup is not able to fabricate

Writing velocities ( $mm/s$ )	Powers ( $mW$ )			
	300	350	380	400
<b>0.1</b>	1380	1340	1410	1340
<b>0.2</b>	1410	1360	1410	1420
<b>1</b>	1380	1360	1400	1440
<b>2</b>	1360	1350	1420	1450
<b>4</b>	1350	1270	1400	1430
<b>10</b>	1320	1270	1370	1400
<b>20</b>	—	—	—	—

Table 5.3. Lengths (in  $\mu m$ ) of the etching paths over lines irradiated at different laser powers and writing speeds along the  $x$  direction (perpendicular to the laser polarization) after **2 hrs** in 20% HF solution. Lengths are given with an uncertainty of  $\pm 40 \mu m$ .

at 20  $mm/s$ , since no modification is observed; for this kind of sample there is no remarkable difference between etching speeds if the writing velocities are limited to few millimeters per second (this is not always the case); there is a minor change in length with the increase of the irradiation power; the acid action take place predominantly in the first hours, accordingly to what was said in section 1.3.1 about the self-limiting effect; the etching along  $y$ , the direction of writing parallel to the laser polarization, is ten times less effective than in the preferential direction, again in agreement to what was said in the first chapter.

Writing velocities ( $mm/s$ )	Powers ( $mW$ )			
	300	350	380	400
<b>0.1</b>	140	210	220	210
<b>0.2</b>	140	190	210	190
<b>1</b>	200	220	265	220
<b>2</b>	250	330	350	370
<b>4</b>	260	300	300	290
<b>10</b>	290	250	210	200
<b>20</b>	—	—	—	—

Table 5.4. Lengths (in  $\mu m$ ) of the etching paths over lines irradiated at different laser powers and writing speeds along the  $y$  direction (parallel to the laser polarization) after **1 h** in 20% HF solution. Lengths are given with an uncertainty of  $\pm 20 \mu m$ .

At the end of this analysis, is possible to foresee that for the DPC the chemical etching will last several hours. The most impervious structure to be reached by the acid will be the cell, since it is buried without any direct access for the acid, which need to transverse the reservoir and the pumping chamber to enter.

For this reason, the main efforts where addressed to the fabrication of the cell.

### 5.3.2 Cell Fabrication: Solutions and Parameters

A scheme of the central part of the device is shown in fig. 5.8. It is realized on a  $20 \times 20 \times 2 \text{ mm}$  fused silica slab. To simulate the pumping chamber, the channel is cut on both sides with two walls.

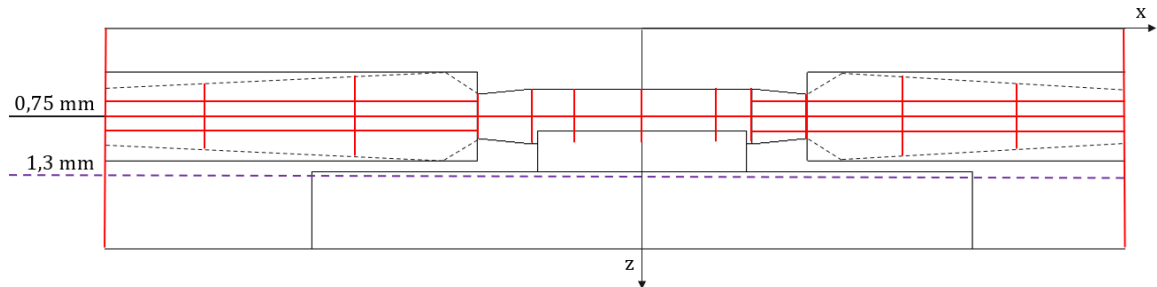


Figure 5.8. Schematic draw of the upside-down glass cell with all the solution adopted for the fabrication. Two zone can be distinguished, before and after the purple dotted line, which are characterized by different positions of the objective's correction collar. Black dotted line: effective irradiation path for the channel. Red lines: cutting planes to ease the glass removal.

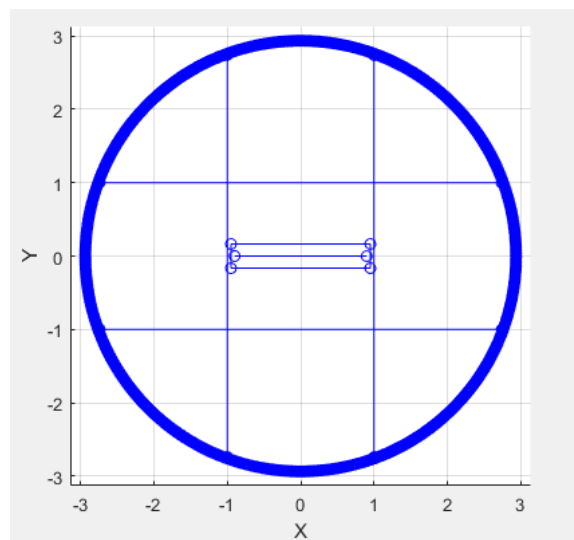


Figure 5.9. Top view of the irradiated path for the reservoir with the cutting planes and the cell-reservoir connection as it is generated by MATLAB.

The 3 mm cell hosting the generation phenomena is the structure which needs to be micromachined with more precision. For this reason the whole DPC is fabricated upside-down, to make the cell nearer to the top. In this way, less irradiation power can be used since the laser transverses a minor distance inside the material ( $0.75 \text{ mm}$ ): it was indeed observed that fabricating the cell with the same power from bottom to top, some modification did not occur making impossible the glass removal.

The irradiation is divided into two parts, interspersed with a position change of the objective's correction collar (from 1.6 to 0.9). This break is exploited also to verify

the laser power has not changed measuring it with a power meter and if necessary is corrected rotating the half-wave plate (see 4.1 for a more detailed description of the beam line).

The first to be irradiated is the reservoir, with a power of 400 *mW* and a helicoidal trajectory.

Secondly, it is made the cell (300 *mW*), then the reservoir basis (350 *mW*) and the connections cell-reservoir (380 *mW*) and cell-channels (300 *mW*). It is fundamental that the channel has a larger diameter than the cell, to strictly confine the gas is strictly confined in the innermost zone.

The black dotted line in fig. 5.8 represents the actual shape of the channel when irradiated (300 *mW*), which differs from the desired one for two reasons. First, since the acid enters much earlier from the wall/pumping chamber than from the cell, then the diameter must shrink as it moves away from the origin; second, the sharp edges near the cell must be removed, to facilitate the acid propagation and making possible the glass detachment.

The separation and the expulsion of the inner glass would be impossible without a number of cutting planes which shape and location were assessed fabricating several prototypes. Five crossed planes divide the volume of the reservoir (fig. 5.9), the central one crosses also the connecting channel and ends inside the cell, acting as a first duct to take the acid in depth. A straight line transverses all the sample along the axis of the channels and in addition two cylinders are irradiated concentric to them (red lines in fig. 5.8). Eleven circular planes are also scanned at the cross sections of the channels and the cell in order to break the glass in multiple pieces. All these planes are irradiated at 380 *mW*.

After the irradiation, the cell is immersed for 5:30 hours in an ultrasonic bath with the etchant solution. The resulting prototype is shown in fig. 5.10 and fig. 5.11.



Figure 5.10. Picture of the THG cell fabricated in a fused silica slab.

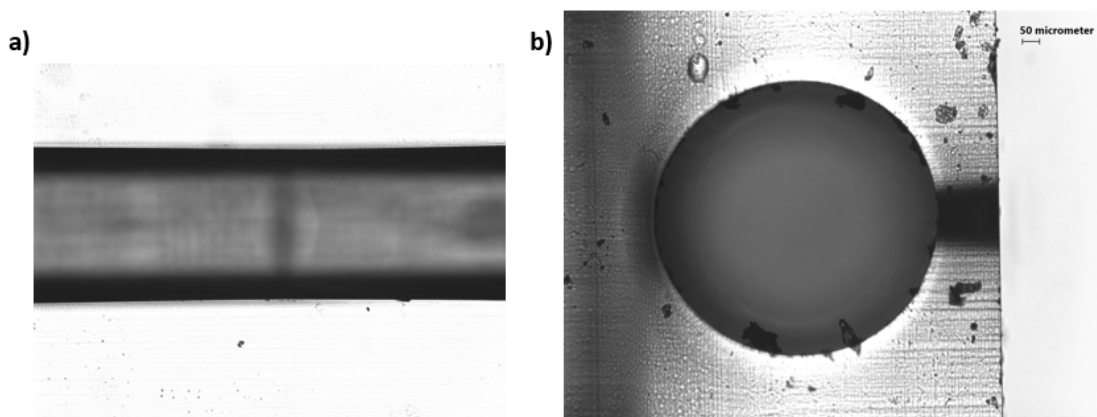


Figure 5.11. Optical microscope images of a) the inner cell and b) the side of the device. The light coming out from the channel show that the etching process was effective in the full removal of the inner glass.

### 5.3.3 DPC micromachining

Conversely to the central cell, the design of the fabrication procedure of the rest of the device is quite straightforward. The main issue to be overcome is the huge time consumption of the whole process, which must be limited as much as possible since the laser power is not stable over a large period of time. Working on the trajectories followed by the laser and maximizing when possible the writing speed, the one-day procedure reported in table 5.5 is set out.

Part	Description	Required time
A	reservoir	1.15 hrs
B	pumping chambers (from 1.3 and 2 mm)	1.15 hrs
C	pumping chambers (from 0 to 1.3 mm)	~7 hrs
D	cell and auxiliaries structures	~12 hrs

Table 5.5. Final procedure for the fabrication of the differential pumping chip.

The process is split in four parts, after each of which the alignment of the laser is checked and power is measured. The first two irradiate all the chip from  $z = 1.3$  to the bottom, the third the remainder of the pumping chambers and the last one, the cell, which is performed overnight.

In fig. 5.12 is showed the chip after the irradiation. The final step is the etching, which takes some additional hours. Once the structure is all empty, the sample can be glued on its support and the device is ready to be used.



Figure 5.12. Picture of a fused silica slab irradiated with the geometry of the differential pumping chip.



# Chapter 6

## High-Order Harmonic Generation in a Thermally Treated Glass Chip

### 6.1 Introduction

In this last chapter is reported the characterization of a microfluidic device used for the generation of high-order harmonics in helium [100] which for the first time underwent a thermal treatment.

The design of this HHG chip is shown in fig. 6.1. Its dimensions are of  $8 \times 10 \times 1 \text{ mm}$  and is composed by a rectangular inlet ( $2 \times 4.7 \times 0.1 \text{ mm}$ ) which is connected to the  $130 \text{ }\mu\text{m}$ -diameter waveguide through evenly-spaced  $100 \text{ }\mu\text{m}$ -long channels. This design serves to two major purposes: first, it ensures an efficient chemical etching, being HF collected by the rectangular chamber and then uniformly distributed along the guide; then, it guarantees an almost uniform gas density distribution inside the hollow waveguide when it is plugged to the gas line.

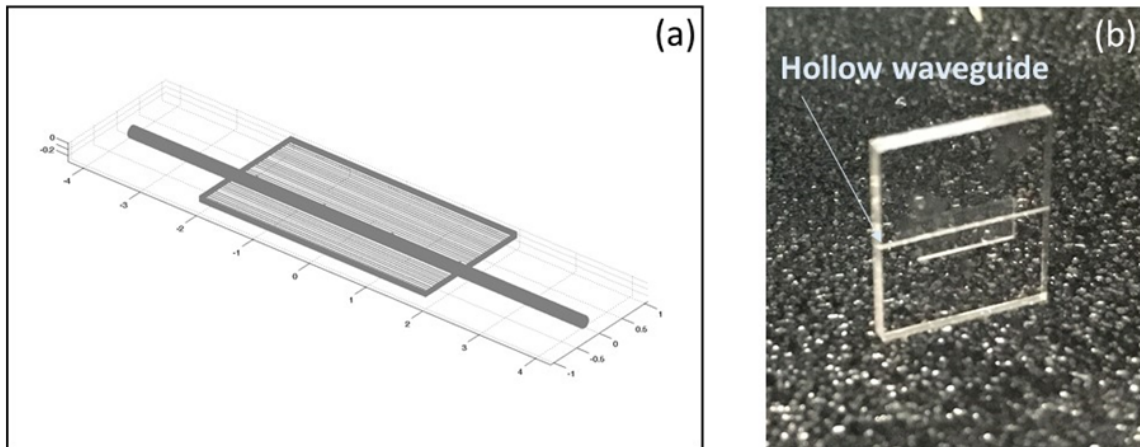


Figure 6.1. (a) Scheme of the irradiation pattern for the HHG chip and (b) a picture of the device fabricated with FLICE technique.

The device is then annealed following the recipe shown in fig. 6.2. Temperature is raised at a rate of  $300 \text{ }^\circ\text{C/h}$  till  $800 \text{ }^\circ\text{C}$ , where is kept constant for 10 hours to

evaporate contaminants inside the furnace. Then the chip is brought for 25 hours to 1215 °C, which is in the stress-relief temperature range for fused silica (see 1.3.3). Eventually it is cooled down following a ramp of 100 °C/h.

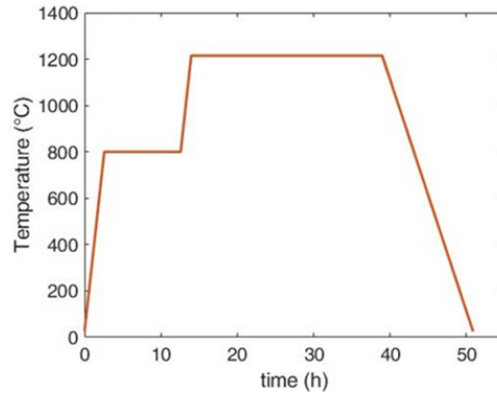


Figure 6.2. Thermal treatment for the annealing of the HHG chip.

A comparison between the inner surface before and after the annealing process is shown in the scanning electron microscope images in fig. 6.3. The periodic pattern visible in 6.3 (a) is due to the scanning step: the waveguide is not irradiated as straight cylinder, but has a variable diameter modulated to be minimum in correspondence of the etching channels and maximum in between. Each 5  $\mu\text{m}$  the GCODE recomputes this diameter giving rise to these ripples.

However, as evident from 6.3 (b), the thermal treatment is very effective in smoothing the internal surface, with a final rugosity which can be estimated from previous works of few nanometers [47, 48].

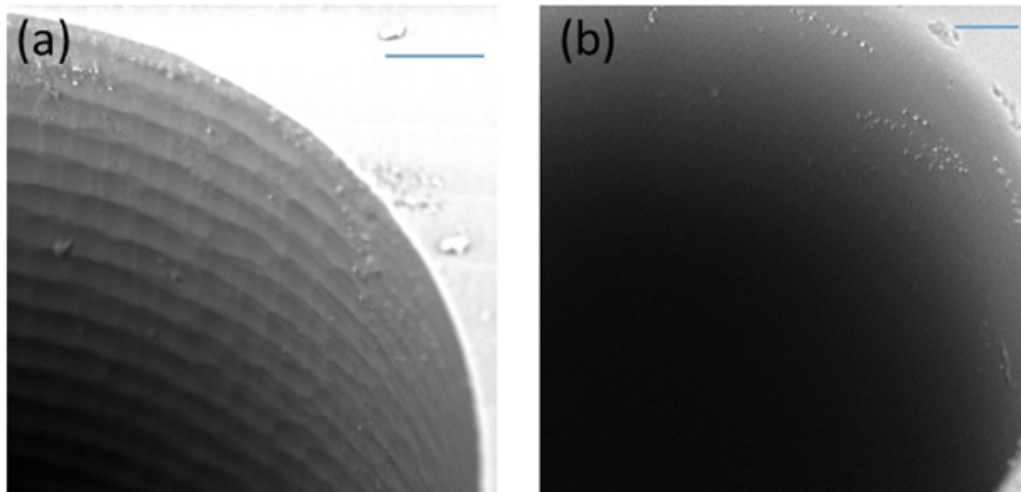


Figure 6.3. SEM images of the HHG chip (a) before and (b) after thermal annealing. Scale bars correspond to 10  $\mu\text{m}$ .

In this chapter, is presented the optical characterization of the hollow waveguide before and after the annealing (Sect. 6.2) and the HHG spectra obtained with the annealed device (Sect. 6.3). A remarkable increase in the generation yield with respect to the not-annealed one is observed.

## 6.2 Device Characterization

The HHG chip was coupled with a laser beam (the setup described in sect. 4.2) to acquire optical properties and obtain near field images, which are shown in fig. 6.4.

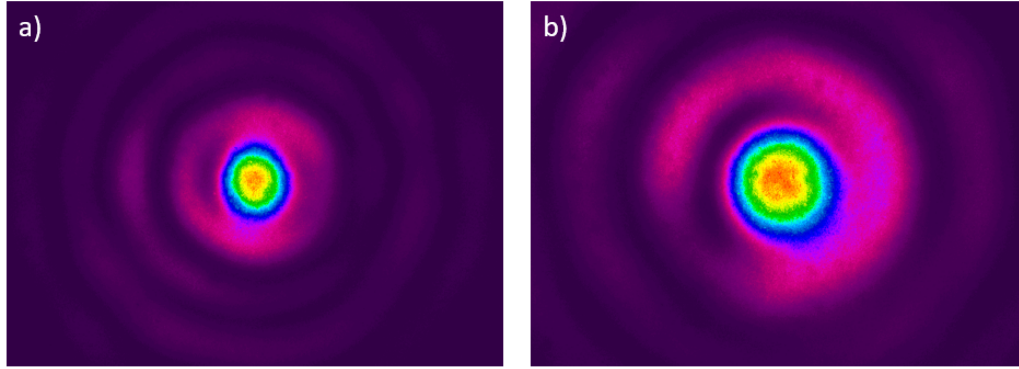


Figure 6.4. Zero order Bessel modes of the waveguide (a) before and (b) after thermal annealing.

As anticipated in Chapter 3, the mode with lowest attenuation which should be supported by a fused silica hollow waveguide is the hybrid  $EH_{11}$ , defined by the radial intensity profile [97]

$$I(r) = I_0 J_0^2 \left( 2.405 \frac{r}{a} \right) \quad (6.1)$$

with  $I_0$  the peak intensity and  $J_0$  the zero order Bessel function of the first kind. To verify that this is the actual case, the above images are imported in MATLAB where a row of points in correspondence to the maximum intensity is extracted and fitted with the aid of the curve fitting tool, which implements a nonlinear least square method.

As fitting function is chosen  $J_0(p(x-x_0)+y_0)^2$ , with  $p$ ,  $x_0$ ,  $y_0$  serving as free coefficients.

Since it is common practice to approximate the squared Bessel function with a more familiar and practical Gaussian profile, the fitting is done in both ways and results are compared. In particular, both the Bessel and the Gaussian curves are employed to assess the mode waist. This is possible thanks to a preliminary calibration of the camera pixels achieved with the near field picture of a grid.

While for the Gaussian the beam size is almost universally taken at  $\frac{1}{e^2}$  of the peak, there is no such an agreement on the definition of the diameter of  $J_0$ 's central lobe, but a common choice is to take as reference the first two zeros [101].

In fig. 6.5 is shown that the retrieved values are identical within the experimental error, so can be considered a rightful choice to ignore the secondary peaks and approximate the central lobe with a Gaussian.

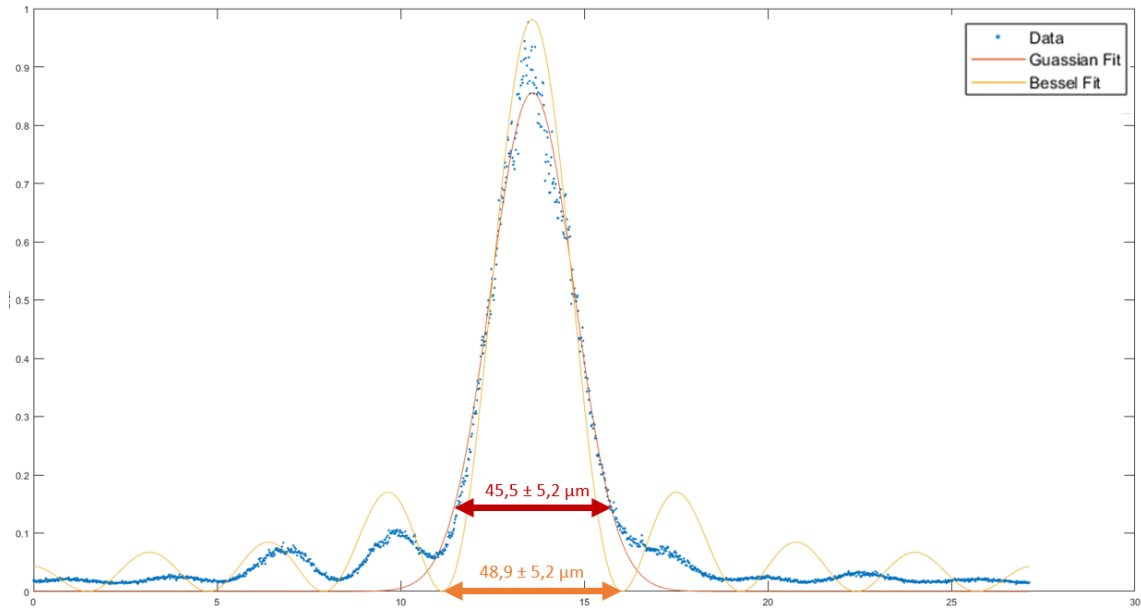


Figure 6.5. Zero order Bessel fitting (in orange) and Gaussian fitting (in red) of the mode transverse profile (in blue) before the annealing of the waveguide. The Bessel fitting function is  $J_0(1.375(x - 10.52) + 0.002)^2$  with an  $R^2$  of 0.95, while the Gaussian is  $0.9\exp(-(\frac{x-10.52}{1.12})^2)$  with  $R^2$  of 0.97. The mode dimension are also shown for both approximations.

Then, the same procedure is repeated once the thermal treatment is completed

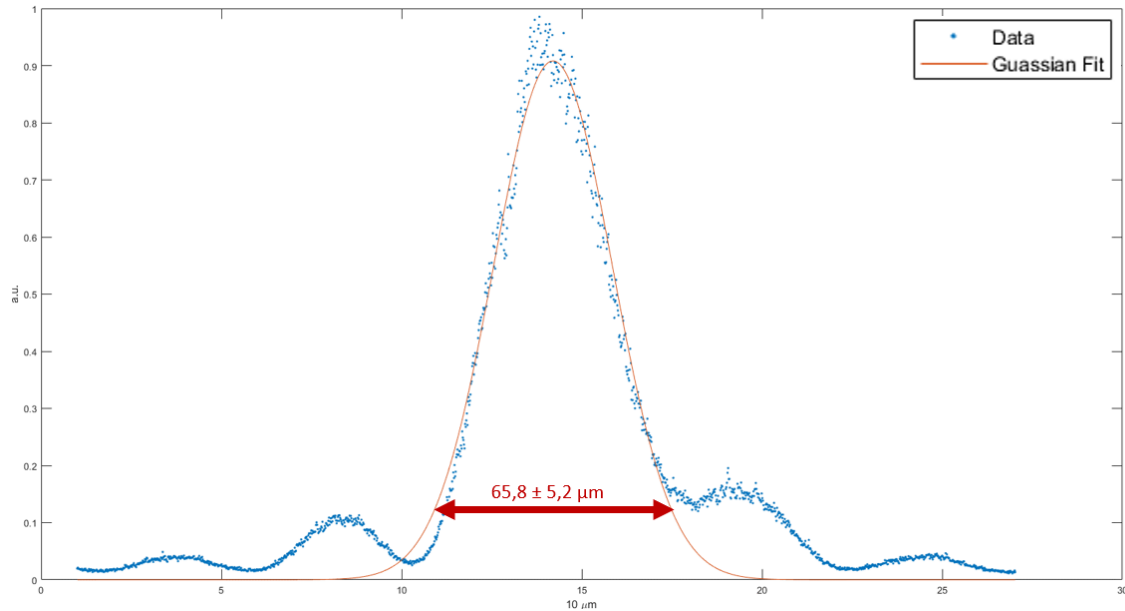


Figure 6.6. Gaussian fitting (in red) of the mode transverse profile (in blue) after the annealing of the waveguide.

Surprisingly, the mode is slightly bigger after the annealing. Since no difference is observed at the optical microscope, the reason might be in the different quality of the inner surface, which somehow affects the propagating mode.

In the end, the insertion losses are calculated as

$$I_L(dB) = 10 \log_{10} \frac{P_{in}}{P_{out}} \quad (6.2)$$

where  $P_{in}$  and  $P_{out}$  are the measured powers before and after the waveguide.  $I_L$  is then a global parameter which includes coupling, propagation, Fresnel and absorption losses.

It turns out  $I_L = 1.193$  dB for the not annealed waveguide and  $I_L = 0.766$  dB after the annealing, which in conclusion seems to slightly improve the guiding properties of the device.

## 6.3 HHG in an Annealed Gas-Filled Hollow Waveguide

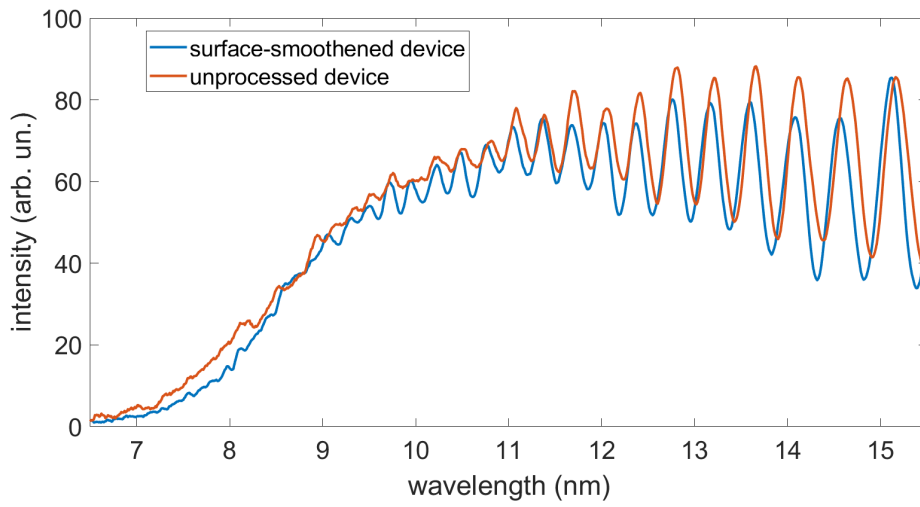
In fig. 6.7 are shown the HHG spectra obtained with the same device before (orange line) and after (blue line) the baking process. The waveguide is filled with helium at different backing pressures.

In these graphics it is possible to retrieve all the characteristics extensively explained in Chapter 3, in particular the fringe pattern of odd harmonics which in this case is shown as a function of the wavelength, extending over 7 nm, when the driving laser has a central frequency of 800 nm (see 4.3 for more details).

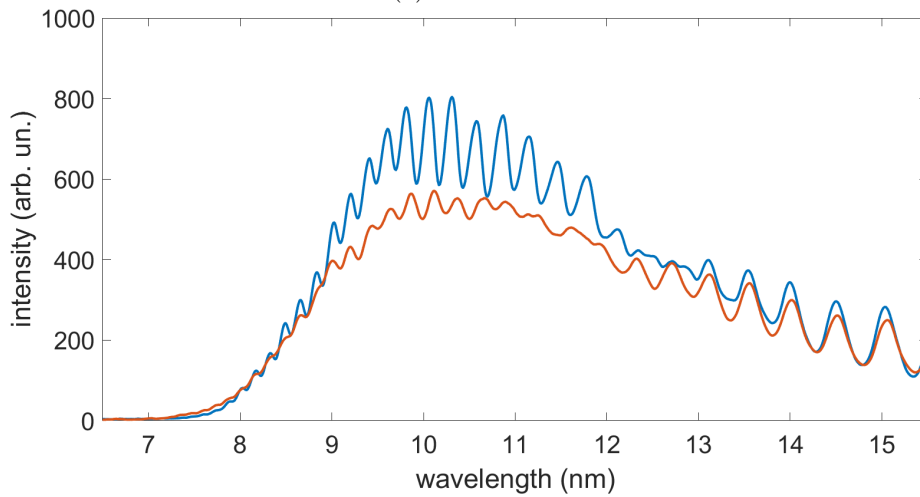
At low pressures (100 mbar) there are no visible differences both in the shape of the spectrum and in the EUV generation yield, with a spectral cut-off at around 9 nm. Increasing the pressure, the annealed chip starts to provide an higher yield of harmonics. In particular, at 400 mbar, this enhancement is localized around the 10 nm wavelength, while the spectra remain similar in other ranges of frequencies. Raising further the pressure, the difference become more apparent: at 1 bar, the yield at 10 nm is almost doubled, peaks are clearly visible also around the cutoff and in general there is a boost in the efficiency of the process.

There is also a reshaping of the spectrum as a function of the gas pressure due to absorption and decoherence effects that are typical in an extended generating medium. Unfortunately, this setup can not provide higher pressures, which the chip could instead accommodate.

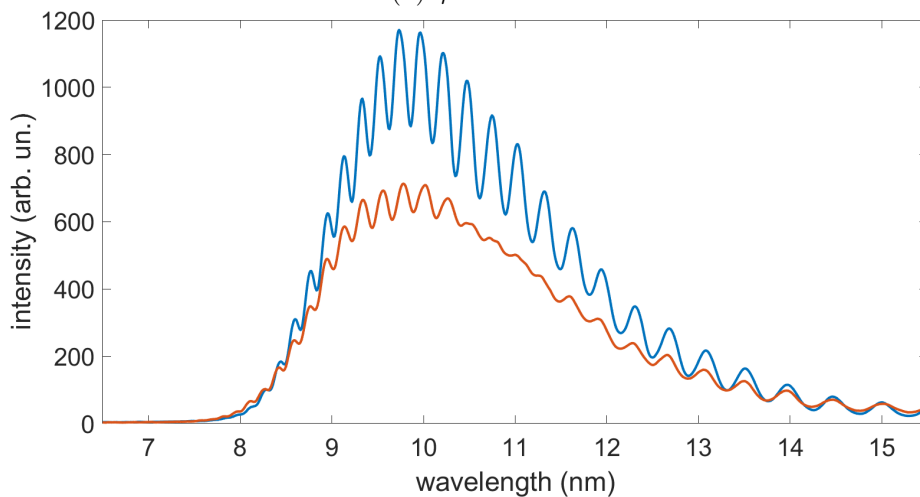
In any case, how structural properties as surface smoothness affect the generation yield is still something mostly unknown.



(a) 100 mbar



(b) 400 mbar



(c) 1 bar

Figure 6.7. HHG spectra generated at different pressures: (a) 100 mbar, (b) 400 mbar, (c) 1 bar. Orange lines are obtained with a not annealed chip, whereas blue line with the treated chip.

# Conclusions

Femtosecond laser micromachining is nowadays a well-established technique for microfabrications. When performed on fused silica and followed by chemical etching, it becomes a powerful tool to build articulated buried hollow structures with a micrometric precision in all three dimensions.

Such structures could be of interest on a wide range of disciplines, and a remarkable example is their ability to host the interaction between an ultra-strong femtosecond laser beam and a gas, which ends in extreme UV radiation generation.

In this work, I exploited this technique for the development and the fabrication of a device which will be devoted to the generation of deep UV radiation, integrating a differential pumping system numerical simulations make promising for a precise spatial confinement of the gas.

I had also the opportunity to investigate how thermal treatments together with the fabrication parameters can influence the quality of the inner surfaces of this kind of devices, and how in turn the structural properties affect the radiation generation efficiency.

The further development of integrated devices, which will include the functionalities of many lab equipment, together with a proper engineering of all the factors influencing the generation yield, will be the basis for the future of Attosecond Physics.



# Appendix A

## Free Molecular Flow Simulations with COMSOL Multiphysics

### A.1 Molecular Gas Flow in Micro-Devices

The motion of rarefied gases in microsystems cannot be addressed with standard tools of computational fluid dynamics, because at extremely low pressures the very concept of fluid itself no longer holds.

A fluid is defined under the so-called *continuum hypothesis*, which considers an infinitesimal volume of matter as the fundamental element of the physical description. This volume contains a large number of molecules in constant motion undergoing collisions between each other and thus can be seen as a collection of discrete point-like elements moving as dictated by Newton's law. The basic equations of fluid dynamic (the continuity equation, Navier-Stokes equation and the energy conservation) are derived considering only the average effects of this microscopic motion, which is instead studied in a kinetic or statistical model when the number of molecules is not high enough to give significance to the mean operation [102].

There are then completely different regimes which can be addressed when studying a gas flow. To discriminate among them the adimensional Knudsen number  $Kn$  is introduced as the ratio between the mean free path  $\lambda$  and some characteristic length  $L$ . Since in this context the mean free path is the average distance a molecule can travel before a collision, a high  $Kn$  means that molecules seldom interact among them but more likely with the walls of the container. For a Boltzmann gas  $Kn$  can be obtained through:

$$Kn = \frac{\lambda}{L} = \frac{T}{\sqrt{2}\pi d^2 p L} \quad (\text{A.1})$$

being  $T$  the temperature in kelvin,  $d$  the particle hard-shell diameter and  $P$  the pressure. Then the four different regime can be distinguished (fig. A.1):

- $Kn < 0.01$ : Continuum flow
- $0.01 < Kn < 0.1$ : Slip flow
- $0.1 < Kn < 10$ : Transitional flow

- $Kn > 10$ : Free molecular flow

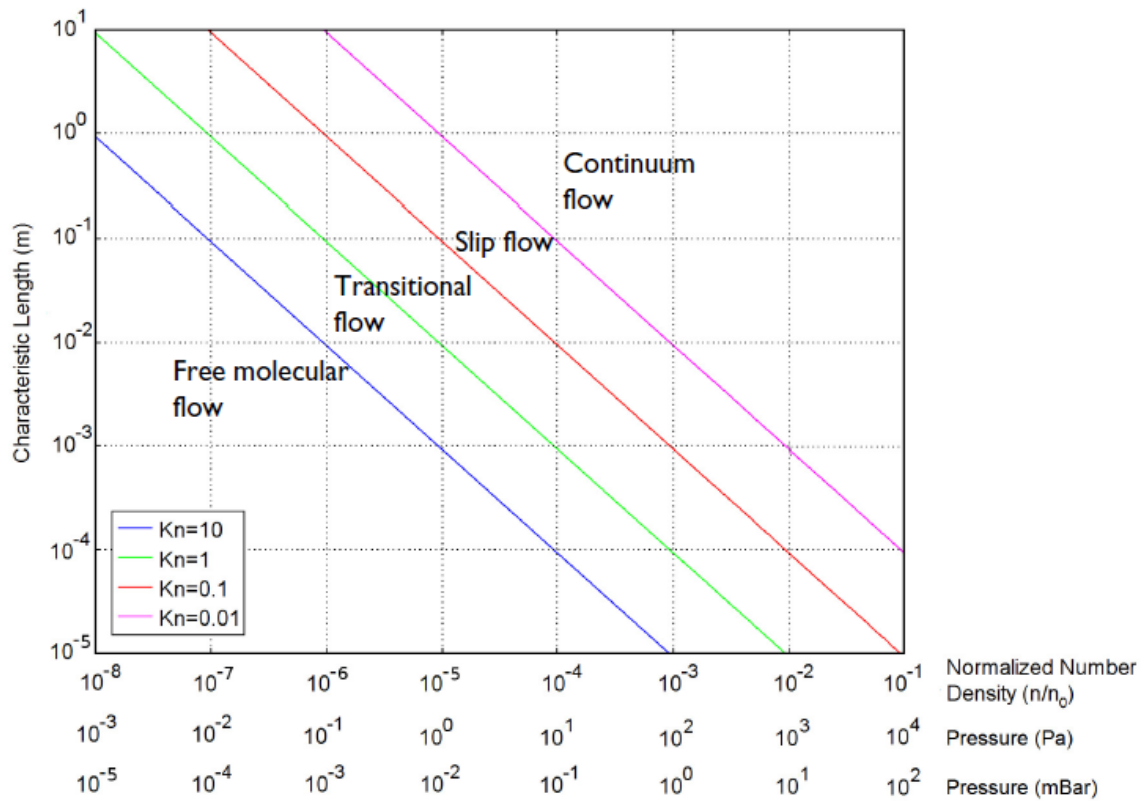


Figure A.1. Fluid flow regimes. Each zone is bounded by constant  $Kn$  lines. The number density on the horizontal is normalized to the number density of an ideal gas at a pressure of 1 *atm* and a temperature of 0 °C. Pressures in different units are also shown. Known the characteristic length and the pressure, one can retrieve the appropriate regime [103].

For both continuum and slip flow classical fluid dynamics equations hold, except (in the second case) for a thin region near to the surface of the containing geometry known as Knudsen layer, thus different boundary conditions are required. The numerical simulation of the flow can be performed with one of the traditional methods of CFD. In transitional regime the continuum hypothesis breaks down and high order correction to the constitutive equations are required, while the simulation needs a more statistical approach [104]. This is even more true for the free molecular flow, which is the regime considered in this work, as indicated by fig. A.1 for a few-centimeters channel in a high vacuum system ( $10^{-4}$  *mbar*).

Historically, academic research on molecular gas flows simulations has been focused on aerospace applications, such as the study of air streams around aircrafts flying at high altitudes, where the atmosphere is much rarefied, or the plume of exhaust gas which allows the movement of a rocket. In both cases, the flow occurs at high Reynolds ( $Re$ ) and Mach ( $Ma$ ) number, and this is often not the case of microfluidic devices, which will then require ad-hoc solutions.

In addition to non-continuum effects, when dealing with microflows should be considered the increased importance of surface effects compared to volumetric properties and possibly multiphysics effects.

The majority of numerical microfluidic simulation are based on Monte Carlo-like methods, which compute the trajectories of a large number of randomized particles through the system. Instead, to simulate the argon flow inside the differential pumping chip, it was chosen the Free Molecular Flow module of COMSOL multiphysics, which is based on a different approach, called *angular coefficient method* [103].

### A.1.1 Angular Coefficient Method

The principle of the angular coefficient method lies in summation of the flux  $\mathbf{G}$  arriving in the infinitesimal surface area  $dA$  from all the other elements  $dA'$  in its line of sight (see fig. A.2). The fluid dynamical variables in the vicinity of the surface are then derived through the equation of kinetic theory. A dedicated function is then able to reconstruct the number density in any point of the volume.

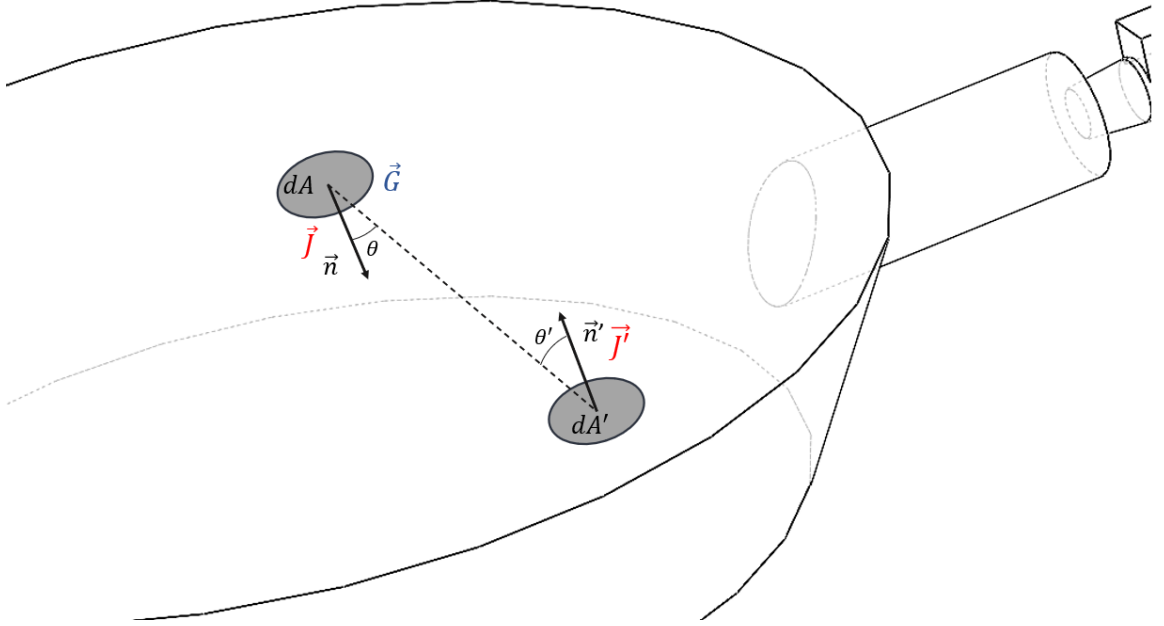


Figure A.2. Scheme for the derivation of the flow  $\mathbf{G}$  impinging in  $dA$ .  $\mathbf{J}$  and  $\mathbf{J}'$  are the fluxes leaving respectively from  $dA$  and  $dA'$ .

To calculate  $\mathbf{G}$  in  $dA$ , it is supposed that in another infinitesimal area  $dA'$  the molecules are diffusely reflected from the surface. It is then necessary to define an appropriate probability density function  $\rho'(\theta', v')$  for emission from  $dA'$ , to be integrated over the surface in the line of sight of  $dA$ . Such distribution has been derived in [105] based on Knudsen's cosine law, and it is found to significantly differ from the renewed Maxwell-Boltzmann distribution which holds in free space, as shown in fig. A.3. It

can be written as:

$$\rho_{2D}(v, \theta) = \sqrt{\frac{2}{\pi}} \left(\frac{m}{T}\right)^{3/2} v^2 \frac{\cos(\theta)}{2} \exp - \left(\frac{mc^2}{2T}\right) \quad (\text{A.2})$$

in two dimensions, and can be extended in three dimension as:

$$\rho_{3D}(v, \theta) = \left(\frac{m}{T}\right)^2 \frac{v^3 \cos(\theta)}{2 \pi} \exp - \left(\frac{mc^2}{2T}\right) \quad (\text{A.3})$$

where  $T$  is temperature in kelvin,  $v$  the velocity and  $m$  the molecular mass. COMSOL Multiphysics allows both two and three-dimensional simulation, but here the focus is on the latter. In this case, it is assumed an uniform probability distribution over the azimuthal angle  $\phi$ .

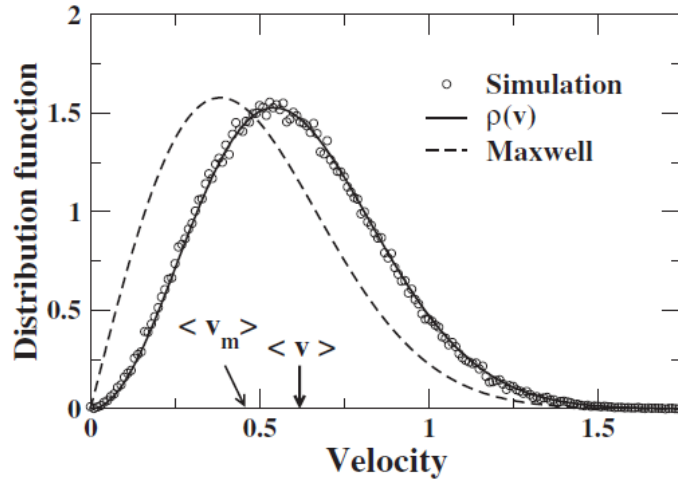


Figure A.3. Probability density functions of the velocity modulus. The dotted curve is Maxwell-Boltzmann distribution, while the full line is  $\rho(v)$  from equation (A.2). Circles are results of molecular dynamics simulations used to validate (A.2), which is derived from the fundamental laws of gas dynamics [105].

Now, the flux  $\mathbf{J}'$  would take a finite time to reach  $dA$ , but this is not taken into account in this model. Thus, this method can be only applied to steady state or quasi-static fluxes, meaning that there shouldn't be any pressure variations faster than the molecular motion. In practice, this is the main limitation for the range of validity of this model. Nonetheless, referring to fig A.2, the 3D flux of molecules leaving  $dA'$  with speeds between  $v$  and  $v + dv$  with angles between  $\theta$  and  $\theta + d\theta$  and  $\phi$  and  $\phi + d\phi$  is

$$\mathbf{J}' dA' \rho_{3D}(v', \theta') \sin |\theta'| d\theta' d\phi' dv' \quad (\text{A.4})$$

and is spread over an area

$$\frac{r^2 \sin(|\theta'|) d\theta' d\phi'}{\cos\theta}. \quad (\text{A.5})$$

Thus, the arriving particle flux is:

$$dG_{3D} = \frac{\mathbf{J} dA' \cos\theta \rho_{3D}(v', \theta') dv'}{r^2}. \quad (\text{A.6})$$

Integrating and remembering that by definition of probability distribution the integral over  $dv'$  is 1,

$$G_{3D} = \int_A \frac{\mathbf{J} \cos\theta \cos\theta'}{\pi r^2} dA = \int_A \frac{\mathbf{J}'(\mathbf{n} \cdot \mathbf{r})(\mathbf{n}' \cdot \mathbf{r})}{\pi r^4} dA \quad (\text{A.7})$$

is obtained, where  $\rho_{3D}(\theta')$  is substituted from (A.3).

The pressure acting on the surface  $dA$  can be derived from the momentum rate of change of molecules impinging normally that elemental surface. COMSOL multiphysics then computes

$$P_{3D} = \int_{A'} \frac{\mathbf{J}'(\mathbf{n} \cdot \mathbf{r})^2 (\mathbf{n}' \cdot \mathbf{r})}{\pi r^5} m \langle v'_{3D} \rangle dA' \quad (\text{A.8})$$

where

$$\langle v'_{3D} \rangle = \sqrt{\frac{9\pi T}{8m}} \quad (\text{A.9})$$

is the mean velocity as can be retrieved from (A.3). The surface  $dA$  can also emit or absorb molecules at a rate  $\mathbf{J}$ . This can be taken into account by setting an appropriate boundary condition: if  $\mathbf{J} = \mathbf{G}$ , there is a wall; if  $\mathbf{J} < \mathbf{G}$ , there is an out-gassing surface; if  $\mathbf{J} > \mathbf{G}$  the gas is pumped in the volume through that surface. The software allows to choose between a set of different boundary conditions (*wall, reservoir, vacuum pump, evaporation...*), for each of which a suitable correction to (A.8) is considered.

The number density  $n$  incoming at  $dA$  is calculated by similar arguments resulting in

$$n_{3D} = \int_{A'} \frac{\mathbf{J}'(\mathbf{n}' \cdot \mathbf{r})}{\pi r^3} \left\langle \frac{1}{v'_{3D}} \right\rangle dA' \quad (\text{A.10})$$

where the mean of inverse speed is

$$\left\langle \frac{1}{v'_{3D}} \right\rangle = \sqrt{\frac{\pi m}{8T}}. \quad (\text{A.11})$$

Again, the total number density will depend on local boundary conditions. Notably,  $n_{3D}$  depends only on the emitted flux, the orientation of  $dA'$  and the molecular velocity at the emitting surface. This can be exploited to compute the flux at any point within the flow domain thanks to the Number Density Reconstruction tool.

## A.2 Differential Pumping Chip Simulations

To predict the behaviour of the gas flow inside the DPC, COMSOL Multiphysics Free Molecular Flow module is chosen.

Even if the software provides a tool to define the geometry, the gas volume was imported from an external CAD file. This choice allows a better accuracy in the design of the domain and facilitates the building of the mesh.

COMSOL Multiphysics contains a broad library of materials between which Argon is selected.

The boundary conditions are shown in fig. A.4. Most of the surfaces, depicted in grey, are *walls*, meaning they diffuse back all the incoming molecular flux. All the walls were kept at the default temperature of 293.15 K. The surface in green has a *reservoir* boundary condition: the molecular flux is computed as effusing from a large adjacent chamber kept at a constant pressure whose extent is much larger of the mean free path. Of course, this is an idealization of the reservoir considered in the design (see Chapter 5) but it was considered a reasonable assumption for a stationary study. Finally, the blue surfaces represent *vacuum pumps*, where a specified pump speed (reported in fig. 5.5) acts to remove molecules from the incident molecular flux.

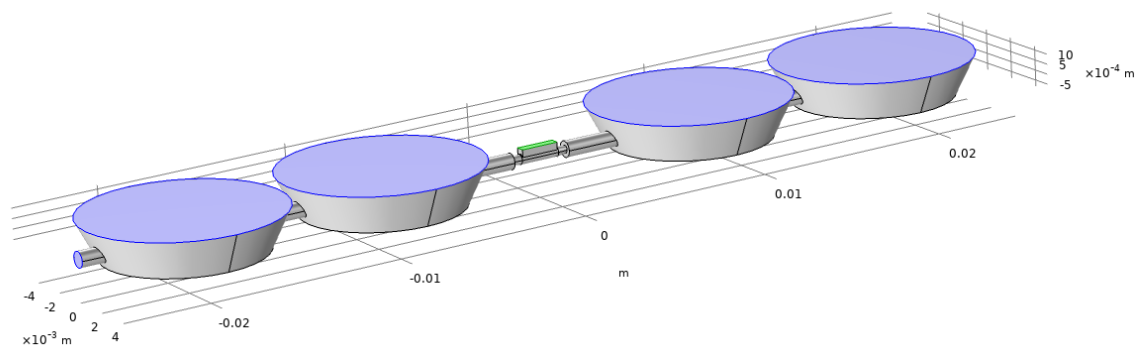


Figure A.4. Volume of gas and boundary conditions applied. Grey: walls; green: reservoir; blue: vacuum pumps.

The Number Density Reconstruction function is enabled, to compute the number density not only at the surfaces but also within the volume.

A detail of the mesh is shown in fig. A.5. COMSOL Multiphysics offers a physics-controlled mesh, which can be made finer or coarser by the user. A finer mesh is selected.

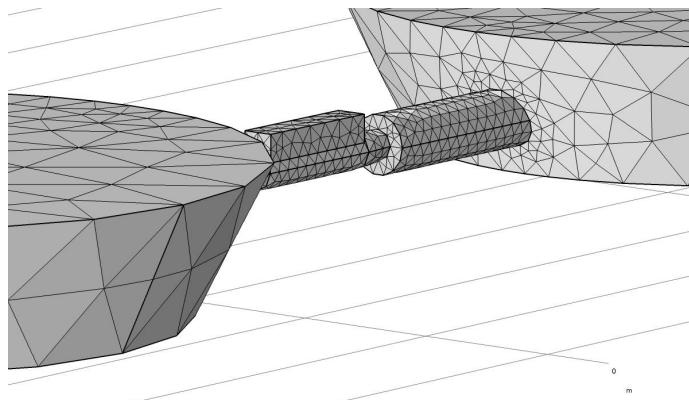


Figure A.5. A detail of the triangle mesh used for these simulations. Only the exterior boundaries are meshed with constant elements. In general, constant elements with a fine mesh provide better accuracy than using coarser higher-order elements.

A first simulation is done with an inlet pressure of  $2 \text{ atm}$ . Other initial values (number density, pressure, incident molecular flux) are all set to zero. The result partially invalidates the assumption of free molecular flow, since the pressure is too high, especially in the central region, to consider this as the proper regime. However, since the device functioning is based on the interaction between the gas and the walls, results obtained neglecting collisions can represent a good starting point.

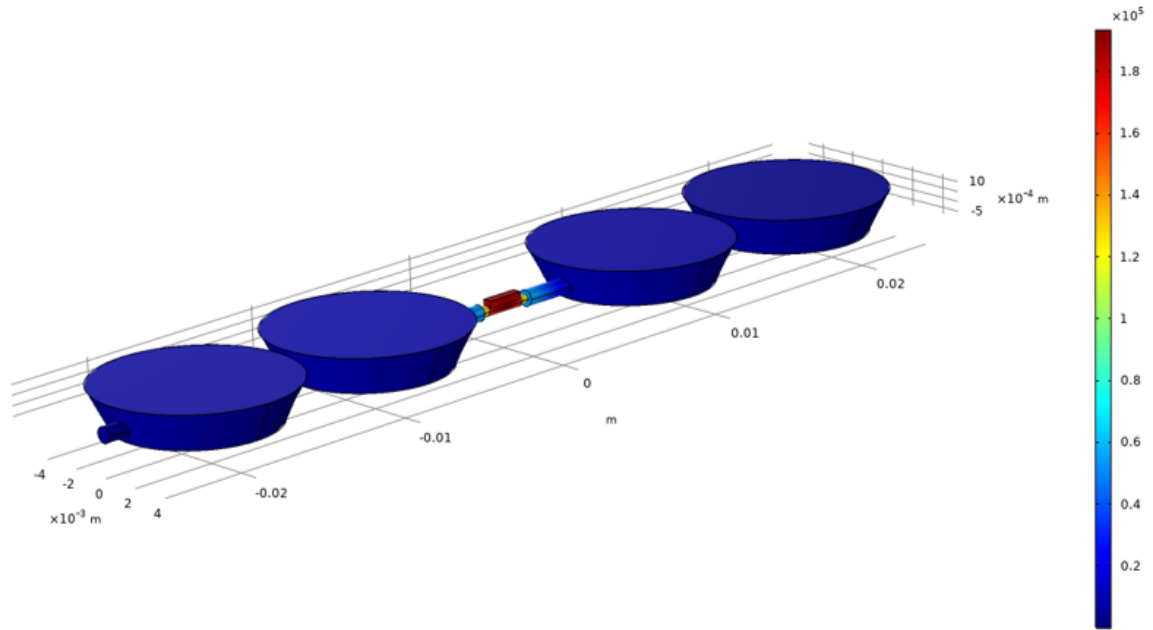


Figure A.6. Pressure at the walls of the device for an inlet pressure of  $2 \text{ atm}$ . The graduated scale is in  $\text{Pa}$ .

Two parametric stationary studies were then performed, computing the number density on the chip axis for different values of the inlet pressure and of the channel diameter.

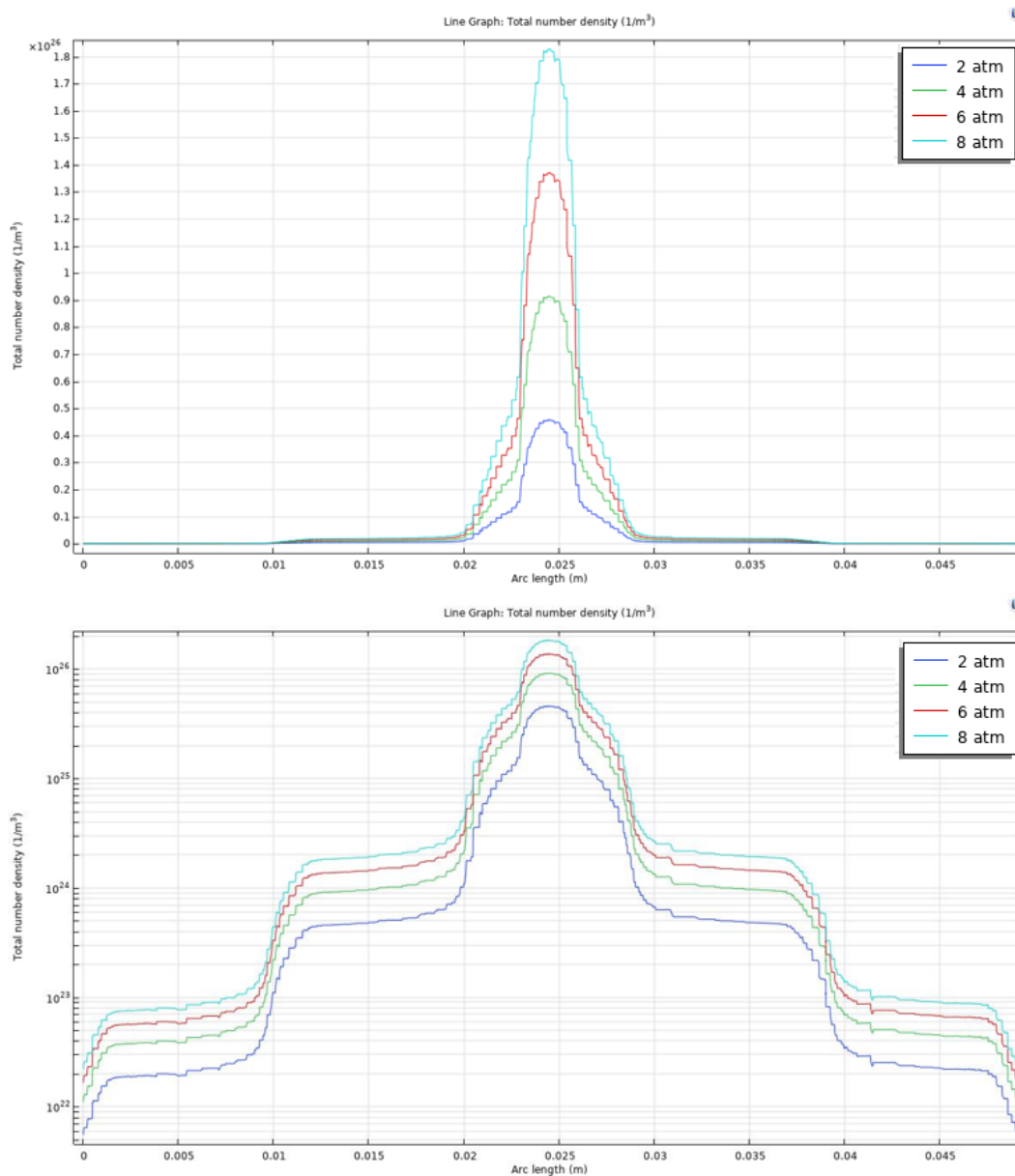


Figure A.7. Total number density ( $\frac{1}{m^3}$ ) along the axis of the DPC for different inlet pressure. On top, linear scale; on bottom, log scale. Blue line: 2 atm; green line: 4 atm; red line: 6 atm; light-blue line: 8 atm.

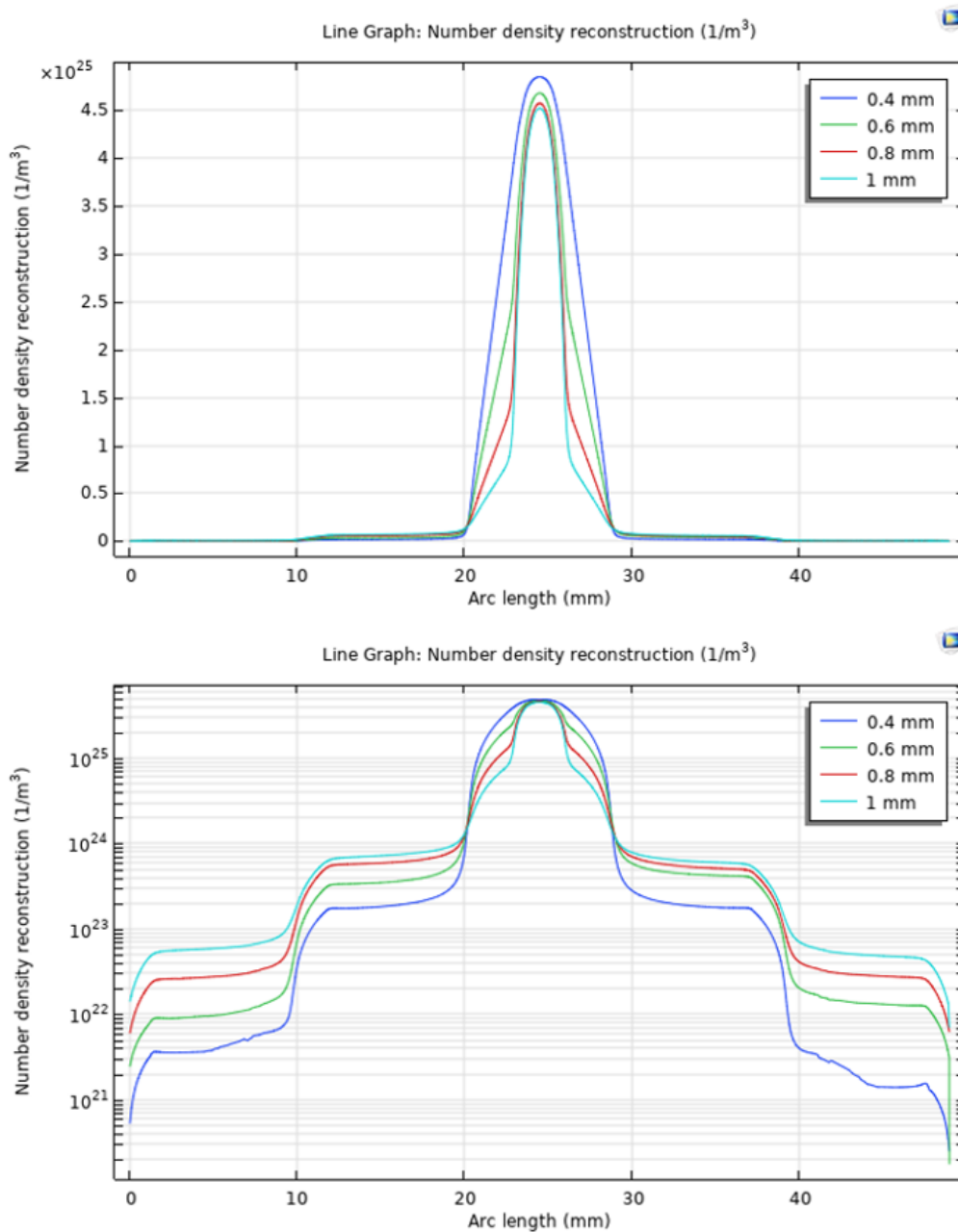


Figure A.8. Total number density ( $\frac{1}{m^3}$ ) along the axis of the DPC for different channel diameters. The inlet pressure is fixed to 2 atm. On top, linear scale; on bottom, log scale. Blue line: 0.4 mm; green line: 0.6 mm; red line: 0.8 mm; light-blue line: 1 mm. For a diameter of 0.4 mm, there is less density in the pumping chambers but the gas is not predominantly confined in the innermost 3 mm. This is in fact the condition in which channel and cell have the same diameter. 0.8 mm is considered a good trade of between the gas confinement and the fabrication requirements.

These graphs seem to confirm the expected behaviour of the gas flow. In the 3 *mm* cell the total number density reaches the maximum value of  $10^{26}$  *particles/m<sup>3</sup>*, and is then reduced by almost two order of magnitude in each subsequent pumping chamber. It is then possible to foresee that less absorption will occur after the generation and in turn there will be an increase in the yield of deep UV radiation.

No remarkable difference is expected in the functioning with the increase of the inlet pressure, which will range up to some *bars*. It is also possible to select freely the channel diameter, as long as it is bigger than 0.4 *mm*. In the end, the dimensions introduced in Chapter 5 are confirmed: the device is 49 *cm* long, the channel has a diameter of 0.8 *mm*, the one of the pumping chambers ranges from 10 to 8 *mm* and the innermost cell, dedicated to the deep UV generation, extends for 3 *mm* with a diameter of 0.4 *mm*.

### A.2.1 Conclusions

The simulation here reported confirms the goodness of the DPC design, predicting a high number density of argon in the generating cell and a gradual decrease in the lateral chambers.

It has been already outlined how numerical investigation of the gas flow will be an important tool for future development of integrated optofluidic devices, which will be more and more articulated in the attempt to include as many functions as possible in a few centimeter glass chip

The approach here proposed has some significant advantages: it is based on a deterministic, accurate, fast algorithm presented on a user-friendly interface. It could be the best choice to preliminary analyze the behaviour of glass devices produced by FLICE technique, in a perspective of fast prototyping and testing of different concepts.

There are however some major limitations in this kind of modelling. First, only quasi-static flows can be consider. Then, the effects of the presence of the laser beam propagation is totally neglected. One must expect that particularly in the generation region the behaviour of the gas is somehow influenced by the plasma generation and nonlinear absorption. This is indeed an interesting problem from a theoretical point of view that will be studied later. Right now the main aim of these simulations is to guarantee a high gas density in the structure before the laser arrives.

Moreover, although free molecular flow can be a reasonable approximation in the lateral chambers, it is not completely correct in the central cell, where argon is injected with a pressure of few bars. To proper simulate the flow, one should look at different regimes in different regions. Unfortunately, this is something that COMSOL Multiphysics can not do, so other software should be considered to implement suitable dynamic equations and take into account collisions' effects.

# Acronyms

**FLM** Femtosecond Laser Micromachining

**FLICE** Femtosecond Laser micromachining followed by Chemical Etching

**EUV** Extreme Ultraviolet

**HHG** High-order Harmonic Generation

**NIR** Near Infrared

**SXR** Soft X-Ray

**DUV** Deep Ultraviolet

**THG** Third-Harmonic Generation

**SHG** Second-Harmonic Generation

**DPC** Differential Pumping Chip



# Bibliography

- [1] Mara Galli et al. “Generation of deep ultraviolet sub-2-fs pulses”. In: *Optics Letters* 44 (6 2019). ISSN: 0146-9592. DOI: 10.1364/ol.44.001308.
- [2] Anna G. Ciriolo et al. “Femtosecond laser-micromachining of glass micro-chip for high order harmonic generation in gases”. In: *Micromachines* 11 (2 2020). ISSN: 2072666X. DOI: 10.3390/mi11020165.
- [3] K. M. Davis et al. “Writing waveguides in glass with a femtosecond laser”. In: *Optics Letters* 21 (21 1996). ISSN: 0146-9592. DOI: 10.1364/ol.21.001729.
- [4] Roberto Osellame, Giulio Cerullo, and Roberta Ramponi. “Femtosecond Laser Micromachining: Photonic and Microfluidic Devices in Transparent Materials”. In: *Topics in Applied Physics* 123 (2012). ISSN: 03034216. DOI: 10.1007/978-3-642-23366-1.
- [5] Andrius Marcinkevičius et al. “Femtosecond laser-assisted three-dimensional microfabrication in silica”. In: *Optics Letters* 26 (5 2001). ISSN: 0146-9592. DOI: 10.1364/ol.26.000277.
- [6] Demetri Psaltis, Stephen R. Quake, and Changhuei Yang. “Developing optofluidic technology through the fusion of microfluidics and optics”. In: *Nature* 442 (7101 2006). ISSN: 14764687. DOI: 10.1038/nature05060.
- [7] C. Monat, P. Domachuk, and B. J. Eggleton. “Integrated optofluidics: A new river of light”. In: 1 (2 2007). ISSN: 17494885. DOI: 10.1038/nphoton.2006.96.
- [8] D. Ehrt et al. “Femtosecond-laser-writing in various glasses”. In: vol. 345-346. 2004. DOI: 10.1016/j.jnoncrysol.2004.08.039.
- [9] Yuri Sikorski et al. “Fabrication and characterization of microstructures with optical quality surfaces in fused silica glass using femtosecond laser pulses and chemical etching”. In: *Appl. Opt.* 45.28 (Oct. 2006), pp. 7519–7523. DOI: 10.1364/AO.45.007519. URL: <http://ao.osa.org/abstract.cfm?URI=ao-45-28-7519>.
- [10] T. Gorelik et al. “Transmission electron microscopy studies of femtosecond laser induced modifications in quartz”. In: *Applied Physics A: Materials Science and Processing* 76 (3 2003). ISSN: 09478396. DOI: 10.1007/s00339-002-1813-x.
- [11] K. L.N. Deepak et al. “Luminescent microstructures in bulk and thin films of PMMA, PDMS, PVA, and PS fabricated using femtosecond direct writing technique”. In: *Chemical Physics Letters* 503 (1-3 2011). ISSN: 00092614. DOI: 10.1016/j.cplett.2010.12.069.

- [12] J. W. Chan et al. “Modification of the fused silica glass network associated with waveguide fabrication using femtosecond laser pulses”. In: *Applied Physics A: Materials Science and Processing* 76 (3 2003). ISSN: 09478396. DOI: 10.1007/s00339-002-1822-9.
- [13] C. B. Schaffer, A. Brodeur, and E. Mazur. “Laser-induced breakdown and damage in bulk transparent materials induced by tightly focused femtosecond laser pulses”. In: *Measurement Science and Technology* 12 (11 2001). ISSN: 09570233. DOI: 10.1088/0957-0233/12/11/305.
- [14] Rafael R. Gattass and Eric Mazur. “Femtosecond laser micromachining in transparent materials”. In: *Nature Photonics* 2 (4 2008). ISSN: 17494885. DOI: 10.1038/nphoton.2008.47.
- [15] R. Osellame et al. “Femtosecond laser microstructuring: an enabling tool for optofluidic lab-on-chips”. In: *Laser & Photonics Reviews* 5.3 (2011), pp. 442–463. DOI: <https://doi.org/10.1002/lpor.201000031>.
- [16] LV Keldysh. “Ionization in the field of a strong electromagnetic wave”. In: *Sov. Phys. JETP* 20 (5 1965).
- [17] Scott C. Jones et al. “Recent Progress On Laser-Induced Modifications And Intrinsic Bulk Damage Of Wide-Gap Optical Materials”. In: *Optical Engineering* 28 (10 1989). ISSN: 0091-3286. DOI: 10.1117/12.7977089.
- [18] B. Stuart et al. “Nanosecond-to-femtosecond laser-induced breakdown in dielectrics”. In: *Physical Review B - Condensed Matter and Materials Physics* 53 (4 1996). ISSN: 1550235X. DOI: 10.1103/PhysRevB.53.1749.
- [19] K. K. Thornber. “Applications of scaling to problems in high-field electronic transport”. In: *Journal of Applied Physics* 52 (1 1981). ISSN: 00218979. DOI: 10.1063/1.328490.
- [20] G. Pucella and S. E. Segre. *Fisica dei Plasmi*. Zanichelli, 2009. ISBN: 9788808063830.
- [21] K. Miura et al. “Photowritten optical waveguides in various glasses with ultrashort pulse laser”. In: *Applied Physics Letters* 71 (23 1997). ISSN: 00036951. DOI: 10.1063/1.120327.
- [22] L. Sudrie et al. “Study of damage in fused silica induced by ultra-short IR laser pulses”. In: *Optics Communications* 191 (3-6 2001). ISSN: 00304018. DOI: 10.1016/S0030-4018(01)01152-X.
- [23] Yasuhiko Shimotsuma et al. “Self-organized nanogratings in glass irradiated by ultrashort light pulses”. In: *Physical Review Letters* 91 (24 2003). ISSN: 10797114. DOI: 10.1103/PhysRevLett.91.247405.
- [24] C. Hnatovsky et al. “Pulse duration dependence of femtosecond-laser-fabricated nanogratings in fused silica”. In: *Applied Physics Letters* 87 (1 2005). ISSN: 00036951. DOI: 10.1063/1.1991991.
- [25] S. Juodkazis et al. “Laser-induced microexplosion confined in the bulk of a sapphire crystal: Evidence of multimegabar pressures”. In: *Physical Review Letters* 96 (16 2006). ISSN: 00319007. DOI: 10.1103/PhysRevLett.96.166101.

- 
- [26] Koji Sugioka, Yasutaka Hanada, and Katsumi Midorikawa. “Three-dimensional femtosecond laser micromachining of photosensitive glass for biomicrochips”. In: *Laser and Photonics Reviews* 4 (3 2010). ISSN: 18638880. DOI: 10.1002/lpor.200810074.
- [27] E. N. Glezer et al. “Three-dimensional optical storage inside transparent materials”. In: *Optics Letters* 21 (24 1996). ISSN: 0146-9592. DOI: 10.1364/ol.21.002023.
- [28] S. Juodkazis et al. “Application of femtosecond laser pulses for microfabrication of transparent media”. In: vol. 197-198. 2002. DOI: 10.1016/S0169-4332(02)00397-5.
- [29] Rod Taylor, Cyril Hnatovsky, and Eli Simova. “Applications of femtosecond laser induced self-organized planar nanocracks inside fused silica glass”. In: *Laser and Photonics Reviews* 2 (1-2 2008). ISSN: 18638880. DOI: 10.1002/lpor.200710031.
- [30] J Mills et al. “Embedded anisotropic micro-reflectors by femtosecond-laser nanomachining”. In: *Applied Physics Letters* 81 (Jan. 2002).
- [31] P. P. Rajeev et al. “Memory in nonlinear ionization of transparent solids”. In: *Physical Review Letters* 97 (25 2006). ISSN: 10797114. DOI: 10.1103/PhysRevLett.97.253001.
- [32] Andrea Macchi. *A Superintense Laser-Plasma Interaction Theory Primer*. Springer, 2013.
- [33] V. R. Bhardwaj et al. “Optically produced arrays of planar nanostructures inside fused silica”. In: *Physical Review Letters* 96 (5 2006). ISSN: 10797114. DOI: 10.1103/PhysRevLett.96.057404.
- [34] P. P. Rajeev et al. “Transient nanoplasmonics inside dielectrics”. In: *Journal of Physics B: Atomic, Molecular and Optical Physics* 40 (11 2007). ISSN: 09534075. DOI: 10.1088/0953-4075/40/11/S03.
- [35] L. Shah et al. “Waveguide writing in fused silica with a femtosecond fiber laser at 522 nm and 1 MHz repetition rate”. In: *Optics Express* 13 (6 2005). ISSN: 1094-4087. DOI: 10.1364/opex.13.001999.
- [36] Krishna Chaitanya Vishnubhatla et al. “Shape control of microchannels fabricated in fused silica by femtosecond laser irradiation and chemical etching”. In: *Optics Express* 17 (10 2009). ISSN: 1094-4087. DOI: 10.1364/oe.17.008685.
- [37] O. Svelto and D.C. Hanna. *Principles of Lasers*. Springer, 2009. ISBN: 1441913017.
- [38] M. Ams et al. “Slit beam shaping method for femtosecond laser direct-write fabrication of symmetric waveguides in bulk glasses”. In: *Optics Express* 13 (15 2005). ISSN: 1094-4087. DOI: 10.1364/opex.13.005676.
- [39] Y. Nasu, M. Kohtoku, and Y. Hibino. “Low-loss waveguides written with a femtosecond laser for flexible interconnection in a planar light-wave circuit”. In: *Optics Letters* 30 (7 2005). ISSN: 0146-9592. DOI: 10.1364/ol.30.000723.
- [40] Roberto Osellame et al. “Femtosecond writing of active optical waveguides with astigmatically shaped beams”. In: *Journal of the Optical Society of America B* 20 (7 2003). ISSN: 0740-3224. DOI: 10.1364/josab.20.001559.

- [41] R. R. Thomson et al. “Shaping ultrafast laser inscribed optical waveguides using a deformable mirror”. In: *Optics Express* 16 (17 2008). ISSN: 1094-4087. DOI: 10.1364/oe.16.012786.
- [42] Shane M. Eaton et al. “Heat accumulation effects in femtosecond laser-written waveguides with variable repetition rate”. In: *Optics Express* 13 (12 2005). ISSN: 1094-4087. DOI: 10.1364/opex.13.004708.
- [43] Satoshi Kiyama et al. “Examination of Etching Agent and Etching Mechanism on Femtosecond Laser Microfabrication of Channels Inside Vitreous Silica Substrates”. In: *The Journal of Physical Chemistry C* 113.27 (2009), pp. 11560–11566.
- [44] G.A.C.M. Spierings. “Wet chemical etching of silicate glasses in hydrofluoric acid based solutions”. In: *Journal of Materials Science* 28 (23 1993). ISSN: 00222461. DOI: 10.1007/BF01352182.
- [45] N. Fukata et al. “In situ spectroscopic measurement of defect formation in SiO<sub>2</sub> induced by femtosecond laser irradiation”. In: *Physica B: Condensed Matter* 340-342 (2003). ISSN: 09214526. DOI: 10.1016/j.physb.2003.09.114.
- [46] K. Miura et al. “Examination of Etching Agent and Etching Mechanism on Femtosecond Laser Microfabrication of Channels Inside Vitreous Silica Substrates”. In: *Proc. SPIE* (2006).
- [47] F. He; J. Lin; Y. Cheng. “Fabrication of hollow optical waveguides in fused silica by three-dimensional femtosecond laser micromachining”. In: *Applied Physics B: Lasers and Optics* 105 (2 Nov. 2011). DOI: 10.1007/s00340-011-4520-5.
- [48] Federico Sala et al. “Effects of Thermal Annealing on Femtosecond Laser Micromachined Glass Surfaces”. In: *Micromachines* 12 (Feb. 2021), p. 180. DOI: 10.3390/mi12020180.
- [49] Nan Shen et al. “Thermal annealing of laser damage precursors on fused silica surfaces”. In: *Optical Engineering* 51 (12 2012). ISSN: 0091-3286. DOI: 10.1117/1.oe.51.12.121817.
- [50] Lukas Gallmann, Claudio Cirelli, and Ursula Keller. “Attosecond science: Recent highlights and future trends”. In: *Annual Review of Physical Chemistry* 63 (2012). ISSN: 0066426X. DOI: 10.1146/annurev-physchem-032511-143702.
- [51] Ferenc Krausz and Misha Ivanov. “Attosecond physics”. In: *Reviews of Modern Physics* 81 (1 2009). ISSN: 15390756. DOI: 10.1103/RevModPhys.81.163.
- [52] G. Sansone et al. “Isolated single-cycle attosecond pulses”. In: *Science* 314 (5798 2006). ISSN: 00368075. DOI: 10.1126/science.1132838.
- [53] D. Fabris et al. “Synchronized pulses generated at 20...eV and 90...eV for attosecond pump-probe experiments”. In: *Nature Photonics* 9 (6 2015). ISSN: 17494893. DOI: 10.1038/nphoton.2015.77.
- [54] Seth L. Cousin et al. “Attosecond streaking in the water window: A new regime of attosecond pulse characterization”. In: *Physical Review X* 7 (4 2017). ISSN: 21603308. DOI: 10.1103/PhysRevX.7.041030.

- 
- [55] M. Nisoli, S. De Silvestri, and O. Svelto. “Generation of high energy 10 fs pulses by a new pulse compression technique”. In: *Applied Physics Letters* 68 (20 1996). ISSN: 00036951. DOI: 10.1063/1.116609.
- [56] C. P. Hauri et al. “Generation of intense, carrier-envelope phase-locked few-cycle laser pulses through filamentation”. In: *Applied Physics B: Lasers and Optics* 79 (6 2004). ISSN: 09462171. DOI: 10.1007/s00340-004-1650-z.
- [57] Chris T. Middleton et al. *DNA excited-state dynamics: From single bases to the double helix*. 2009. DOI: 10.1146/annurev.physchem.59.032607.093719.
- [58] Thomas Gustavsson, Roberto Improta, and Dimitra Markovitsi. *DNA/RNA: Building blocks of life under UV irradiation*. 2010. DOI: 10.1021/jz1004973.
- [59] Charles G. Durfee et al. “Intense 8-fs pulse generation in the deep ultraviolet”. In: *Optics Letters* 24 (10 1999). ISSN: 0146-9592. DOI: 10.1364/ol.24.000697.
- [60] Tamas Nagy and Peter Simon. “Generation of 200-J, sub-25-fs deep-UV pulses using a noble-gas-filled hollow fiber”. In: *Optics Letters* 34 (15 2009). ISSN: 0146-9592. DOI: 10.1364/ol.34.002300.
- [61] Yuichiro Kida et al. “Sub-10 fs deep-ultraviolet pulses generated by chirped-pulse four-wave mixing”. In: *Optics Letters* 35 (11 2010). ISSN: 0146-9592. DOI: 10.1364/ol.35.001807.
- [62] P. Baum, S. Lochbrunner, and E. Riedle. “Generation of tunable 7-fs ultraviolet pulses: Achromatic phase matching and chirp management”. In: vol. 79. 2004. DOI: 10.1007/s00340-004-1668-2.
- [63] Felix Köttig et al. “Generation of microjoule pulses in the deep ultraviolet at megahertz repetition rates”. In: *Optica* 4 (10 2017). ISSN: 2334-2536. DOI: 10.1364/optica.4.001272.
- [64] “Generation of sub-3 fs pulses in the deep ultraviolet”. In: *Optics Letters* 35 (13 2010). ISSN: 0146-9592. DOI: 10.1364/ol.35.002248.
- [65] B.Y. Soon and J.W. Haus. “chi (3) - Third-Harmonic Generation”. In: *Encyclopedia of Modern Optics*. 2004.
- [66] J. Ringling et al. “Tunable femtosecond pulses in the near vacuum ultraviolet generated by frequency conversion of amplified Ti:sapphire laser pulses”. In: *Optics Letters* 18 (23 1993). ISSN: 0146-9592. DOI: 10.1364/ol.18.002035.
- [67] G. H.C. New and J. F. Ward. “Optical third-harmonic generation in gases”. In: *Physical Review Letters* 19 (10 1967). ISSN: 00319007. DOI: 10.1103/PhysRevLett.19.556.
- [68] J. F. Ward and G. H.C. New. “Optical third harmonic generation in gases by a focused laser beam”. In: *Physical Review* 185 (1 1969). ISSN: 0031899X. DOI: 10.1103/PhysRev.185.57.
- [69] N. Nayak. “Quantum Theory of Third-Harmonic Generation in a Gaseous System-part 1”. In: *IEEE Journal of Quantum Electronics* 16 (8 1980). ISSN: 15581713. DOI: 10.1109/JQE.1980.1070581.

- [70] Gabriel Álvarez and Ramón F. Álvarez-Estrada. “Third harmonic generation as a third-order quasi-exactly solvable system”. In: *Journal of Physics A: Mathematical and General* 34 (47 2001). ISSN: 03054470. DOI: 10.1088/0305-4470/34/47/310.
- [71] S. T. Gevorkyan. “Quantum superposition states in third-harmonic generation”. In: *Physical Review A - Atomic, Molecular, and Optical Physics* 58 (6 1998). ISSN: 10941622. DOI: 10.1103/PhysRevA.58.4862.
- [72] Jiří Bajer and Adam Miranowicz. “Sub-Poissonian photon statistics of higher harmonics: quantum predictions via classical trajectories”. In: *Journal of Optics B: Quantum and Semiclassical Optics* 2 (3 2000). ISSN: 14644266. DOI: 10.1088/1464-4266/2/3/102.
- [73] Philippe Antoine, Anne L’Huillier, and Maciej Lewenstein. “Attosecond pulse trains using high-order harmonics”. In: *Physical Review Letters* 77 (7 1996). ISSN: 10797114. DOI: 10.1103/PhysRevLett.77.1234.
- [74] Margherita Zavelani-Rossi and Federico Vismarra. *High Intensity Lasers for nuclear and physical applications*. 2020. DOI: 10.15651/9788893851886.
- [75] A. McPherson et al. “Studies of multiphoton production of vacuum-ultraviolet radiation in the rare gases”. In: *Journal of the Optical Society of America B* 4 (4 1987). ISSN: 0740-3224. DOI: 10.1364/josab.4.000595.
- [76] M. Ferray et al. “Multiple-harmonic conversion of 1064 nm radiation in rare gases”. In: *Journal of Physics B: Atomic, Molecular and Optical Physics* 21 (3 1988). ISSN: 09534075. DOI: 10.1088/0953-4075/21/3/001.
- [77] P. B. Corkum. “Plasma perspective on strong field multiphoton ionization”. In: *Physical Review Letters* 71 (13 1993). ISSN: 00319007. DOI: 10.1103/PhysRevLett.71.1994.
- [78] Jeffrey L. Krause, Kenneth J. Schafer, and Kenneth C. Kulander. “High-order harmonic generation from atoms and ions in the high intensity regime”. In: *Physical Review Letters* 68 (24 1992). ISSN: 00319007. DOI: 10.1103/PhysRevLett.68.3535.
- [79] M. Lewenstein et al. “Theory of high-harmonic generation by low-frequency laser fields”. In: *Physical Review A* 49 (3 1994). ISSN: 10502947. DOI: 10.1103/PhysRevA.49.2117.
- [80] Alexey Gorlach et al. “The quantum-optical nature of high harmonic generation”. In: *Nature Communications* 11 (1 2020). ISSN: 20411723. DOI: 10.1038/s41467-020-18218-w.
- [81] Cheng Jin. *Theory of nonlinear propagation of high harmonics generated in a gaseous medium*. 2012.
- [82] M. V. Fedorov. “L. V. Keldysh’s “Ionization in the Field of a Strong Electromagnetic Wave” and modern physics of atomic interaction with a strong laser field”. In: *Journal of Experimental and Theoretical Physics* 122 (3 2016). ISSN: 10637761. DOI: 10.1134/S1063776116030043.

- 
- [83] A. Perelomov, V. Popov, and M. Terent'ev. "Ionization of Atoms in an Alternating Electric Field". In: *Soviet Journal of Experimental and Theoretical Physics* 23 (1966). ISSN: 1063-7761.
- [84] M. V. Ammosov, N. B. Delone, and V. P. Krainov. "Tunnel ionization of complex atoms and of atomic ions in an alternating electromagnetic field". In: *Soviet Physics - JETP* 64 (6 1986).
- [85] X. M. Tong, Z. X. Zhao, and C. D. Lin. "Theory of molecular tunneling ionization". In: *Physical Review A - Atomic, Molecular, and Optical Physics* 66 (3 2002). ISSN: 10941622. DOI: 10.1103/PhysRevA.66.033402.
- [86] Hampus Wikmark et al. "Spatiotemporal coupling of attosecond pulses". In: *Proceedings of the National Academy of Sciences of the United States of America* 116 (11 2019). ISSN: 10916490. DOI: 10.1073/pnas.1817626116.
- [87] Bing Shan and Zenghu Chang. "Dramatic extension of the high-order harmonic cutoff by using a long-wavelength driving field". In: *Physical Review A - Atomic, Molecular, and Optical Physics* 65 (1 2002). ISSN: 10941622. DOI: 10.1103/PhysRevA.65.011804.
- [88] Andy Rundquist et al. "Phase-matched generation of coherent soft x-rays". In: *Science* 280 (5368 1998). ISSN: 00368075. DOI: 10.1126/science.280.5368.1412.
- [89] Tenio Popmintchev et al. "Phase matching of high harmonic generation in the soft and hard X-ray regions of the spectrum". In: *Proceedings of the National Academy of Sciences of the United States of America* 106 (26 2009). ISSN: 00278424. DOI: 10.1073/pnas.0903748106.
- [90] Tenio Popmintchev et al. "Bright coherent ultrahigh harmonics in the kev x-ray regime from mid-infrared femtosecond lasers". In: *Science* 336 (6086 2012). ISSN: 10959203. DOI: 10.1126/science.1218497.
- [91] T. Augustine, B. Carré, and P. Salières. "Quasi-phase-matching of high-order harmonics using a modulated atomic density". In: *Physical Review A - Atomic, Molecular, and Optical Physics* 76 (1 2007). ISSN: 10502947. DOI: 10.1103/PhysRevA.76.011802.
- [92] E. Constant et al. "Optimizing high harmonic generation in absorbing gases: Model and experiment". In: *Physical Review Letters* 82 (8 1999). ISSN: 10797114. DOI: 10.1103/PhysRevLett.82.1668.
- [93] Justin Peatross, Sergei Voronov, and I. Prokopovich. "Selective zoning of high harmonic emission using counter-propagating light". In: *Optics Express* 1 (5 1997). ISSN: 1094-4087. DOI: 10.1364/oe.1.000114.
- [94] Hyun Ook Seo et al. "Improving the efficiency of high harmonic generation (HHG) by Ne-admixing into a pure Ar gas medium". In: *Applied Physics B: Lasers and Optics* 122 (4 2016). ISSN: 09462171. DOI: 10.1007/s00340-016-6347-6.
- [95] Ph. Balcou and Anne L'Huillier. "Phase-matching effects in strong-field harmonic generation". In: *Physical Review A* 47 (2 1993). ISSN: 10502947. DOI: 10.1103/PhysRevA.47.1447.

- [96] M. Nisoli et al. “A novel-high energy pulse compression system: Generation of multigigawatt sub-5-fs pulses”. In: *Applied Physics B: Lasers and Optics* 65 (2 1997). ISSN: 09462171. DOI: 10.1007/s003400050263.
- [97] E. A.J. Marcatili and R. A. Schmelzter. “Hollow Metallic and Dielectric Waveguides for Long Distance Optical Transmission and Lasers”. In: *Bell System Technical Journal* 43 (4 1964). ISSN: 15387305. DOI: 10.1002/j.1538-7305.1964.tb04108.x.
- [98] C. Bridgman. “Design aspects of a differential vacuum pumping system”. In: *Journal of Vacuum Science Technology A Vacuum Surfaces and Films* 7 (3 May 1989). DOI: 10.1116/1.575913.
- [99] W.K. Warburton; P. Pianetta. “A novel differential pump for synchrotron beamlines tests, models and applications”. In: *Nuclear Instruments and Methods in Physics Research Section A: Accelerators, Spectrometers, Detectors and Associated Equipment* 291 (1-2 1990). DOI: 10.1016/0168-9002(90)90086-1.
- [100] A. G. Ciriolo et al. “High-order harmonic generation in a microfluidic glass device”. In: *JPhys Photonics* 2 (2 2020). ISSN: 25157647. DOI: 10.1088/2515-7647/ab7d81.
- [101] G. S. Sokolovskii et al. *Bessel beams from semiconductor light sources*. 2014. DOI: 10.1016/j.pquantelec.2014.07.001.
- [102] Pijush Kundu, Ira Cohen, and David Dowling. *Fluid Mechanics*. 2012. DOI: 10.1016/C2009-0-63410-3.
- [103] URL: <https://doc.comsol.com/5.4/doc/com.comsol.help.molec/MolecularFlowModuleUsersGuide.pdf> (visited on 03/13/2021).
- [104] George Karniadakis, Ali Beskok, and Narayan Aluru. *Microflows and Nanoflows: Fundamentals and Simulation (Interdisciplinary Applied Mathematics)*. 2005.
- [105] Franck Celestini and Fabrice Mortessagne. “Cosine law at the atomic scale: Toward realistic simulations of Knudsen diffusion”. In: *Physical Review E - Statistical, Nonlinear, and Soft Matter Physics* 77 (2 2008). ISSN: 15393755. DOI: 10.1103/PhysRevE.77.021202.